

REPORT DOCUMENTATION PAGE

Form Approved
OMB No. 0704-0188

The public reporting burden for this collection of information is estimated to average 1 hour per response, including the time for reviewing instructions, searching existing data sources, gathering and maintaining the data needed, and completing and reviewing the collection of information. Send comments regarding this burden estimate or any other aspect of this collection of information, including suggestions for reducing the burden, to Department of Defense, Washington Headquarters Services, Directorate for Information Operations and Reports (0704-0188), 1215 Jefferson Davis Highway, Suite 1204, Arlington, VA 22202-4302. Respondents should be aware that notwithstanding any other provision of law, no person shall be subject to any penalty for failing to comply with a collection of information if it does not display a currently valid OMB control number.

PLEASE DO NOT RETURN YOUR FORM TO THE ABOVE ADDRESS.

1. REPORT DATE (DD-MM-YYYY) 02/15/2013			2. REPORT TYPE Interim Research Performance Report		3. DATES COVERED (From - To) 11/1/2012 - 01/31/2013	
4. TITLE AND SUBTITLE Interim Research Performance Report Quarterly Report No. 6					5a. CONTRACT NUMBER	
					5b. GRANT NUMBER N00014-11-1-0752	
					5c. PROGRAM ELEMENT NUMBER	
6. AUTHOR(S) Nathan E. Murray, Charles E. Tinney (U. of Texas at Austin), Brian S. Thurow (Auburn Univ.), Praveen Panickar (CRAFT Tech.)					5d. PROJECT NUMBER	
					5e. TASK NUMBER	
					5f. WORK UNIT NUMBER	
7. PERFORMING ORGANIZATION NAME(S) AND ADDRESS(ES) The University of Mississippi Jamie Whitten National Center for Physical Acoustics University, MS 38677					8. PERFORMING ORGANIZATION REPORT NUMBER	
9. SPONSORING/MONITORING AGENCY NAME(S) AND ADDRESS(ES) Joseph Doychak Office of Naval Research 875 North Randolph Street Arlington, VA 22203-1995					10. SPONSOR/MONITOR'S ACRONYM(S) ONR	
					11. SPONSOR/MONITOR'S REPORT NUMBER(S)	
12. DISTRIBUTION/AVAILABILITY STATEMENT Approved for Public Release; Distribution is Unlimited						
13. SUPPLEMENTARY NOTES						
14. ABSTRACT The research team made steady progress in many areas during the reporting period. Review and research into the characterization of the noise source continues and is guiding data analysis efforts. CFD solutions were completed and used to generate time-resolved flow data for further analysis to study relevant aeroacoustic sources. Significant progress was made on the development and application of the computational phased array beamforming analysis. Analysis of standard stereo-PIV data acquired in October, 2012, was completed and reduced to generate a database for further study and comparison with other diagnostic efforts.						
15. SUBJECT TERMS Jet Noise Reduction, High Dynamic Range PIV, Computational Phased Array Beamforming, Aeroacoustics						
16. SECURITY CLASSIFICATION OF:			17. LIMITATION OF ABSTRACT	18. NUMBER OF PAGES 90	19a. NAME OF RESPONSIBLE PERSON Nathan E. Murray	
a. REPORT	b. ABSTRACT	c. THIS PAGE			19b. TELEPHONE NUMBER (Include area code) 662-915-3190	

TOWARD ACTIVE CONTROL OF NOISE
FROM HOT SUPERSONIC JETS

Quarterly Progress Report No. 6

1 NOVEMBER 2012 – 31 JANUARY 2013

Nathan E. Murray (PI)
National Center for Physical Acoustics
The University of Mississippi
University, MS 38677
(662) 915-3190
nmurray@olemiss.edu

Charles E. Tinney (Co-PI) – The University of Texas at Austin
Brian S. Thurow (Co-PI) – Auburn University
Praveen Panickar – Combustion Research and Flow Technology, Inc.

Contract: N00014-11-1-0752

Attn: Joseph Doychak & Brenda Henderson
Office of Naval Research
Arlington, VA 22203-1995
joseph_doychak@onr.mil | brenda.s.henderson@navy.mil

Executive Summary

The research team made steady progress in many areas during the reporting period. Review and research into the characterization of the noise source continues and is guiding data analysis efforts. CFD solutions were completed and used to generate time-resolved flow data for further analysis to study relevant aeroacoustic sources. Significant progress was made on the development and application of the computational phased array beam-forming analysis. Analysis of standard stereo-PIV data acquired in October, 2012, was completed and reduced to generate a database for further study and comparison with other diagnostic efforts.

20130221070

15 February 2013

Contents

1	Project Objectives and Status	2
1.1	Review of Program Objectives	2
1.2	Project Status	3
2	Activity for Current Reporting Period	3
2.1	Significance of the Jet Conditions	3
2.1.1	Near-Field Acoustic Characterization	5
2.2	Exploring Aeroacoustic Source Terms	8
2.2.1	Time-Resolved CFD Data Set for Aeroacoustic Source Analysis . . .	9
2.2.2	Computation of Acoustically Relevant Source Terms	10
2.2.3	Possible Entropic Effects	10
2.3	Updates on Computational Phased Array Work	13
2.4	Stereo PIV Analysis of Jet Characteristics	14
2.4.1	Preliminary Results	16
2.5	Progress on HDR-PIV Diagnostic Efforts	17
2.5.1	DEVOLS Processing for HDR-PIV	17
2.5.2	Current Status of Experimental Efforts	17
3	Technical/Cost Status & Problem Areas	18
3.1	Status Summary	18
3.2	High-Frame-Rate Camera for HDR-PIV	18
3.3	Other Potential Imaging Diagnostic Options	19
4	Publications, Meetings, and/or Travel	19
4.1	Running List of Publications Produced	19
5	Planned Activities for Next Reporting Period	20
6	Cited References	20

Appendices

A	FORTTRAN Code for Computing Derivatives from CFD Data . .	A-1
B	Baars & Tinney APS-DFD-D24:8	B-1
C	Panickar <i>et al.</i> AIAA-2013-0613	C-1
D	Presentation Slides from Panickar <i>et al.</i> AIAA-2013-0613. . . .	D-1
E	Haynes <i>et al.</i> AIAA-2013-0774	E-1

1 Project Objectives and Status

1.1 Review of Program Objectives

The primary objective of this research effort is to address the deficiency in the understanding of the effect that near-nozzle and inner-nozzle flow conditions have on jet noise radiation.

This is particularly relevant to future active control efforts because any control strategy will involve modification of the boundary conditions. The approach guiding the current effort is three-fold:

1. high-fidelity characterization of heated, over-expanded supersonic jets,
2. source identification through development of advanced analytical diagnostics, and
3. enhanced computational modeling of hot supersonic jets.

1.2 Project Status

An updated project chart is shown in Figure 1 which details the WBS items from the SOW and the completion percentages as of the end of the reporting period. The research team made steady progress in many areas during the reporting period. Review and research into the characterization of the noise source continues and is guiding data analysis efforts. CFD solutions were completed and used to generate time-resolved flow data for further analysis to study relevant aeroacoustic sources. Significant progress was made on the development and application of the computational phased array beamforming analysis. Analysis of standard stereo-PIV data acquired in October, 2012, was completed and reduced to generate a database for further study and comparison with other diagnostic efforts. Details of new activity and results are presented in the following section.

2 Activity for Current Reporting Period

2.1 Significance of the Jet Conditions

The accurate determination of the jet exit conditions is complicated in general and more so in shock containing supersonic jets. In the current study, focused on conic nozzles, the non-ideal expansion yields shocks that emanate from within the nozzle. As a result, the exit plane is not characterized by a uniform outflow.

The study of the effects of nozzle conditions for subsonic jets has been a topic of discussion among a number of researchers in the last decade. In particular, Viswanathan[1] did an extensive study to vary Reynolds number and temperature ratio independently and found a transition in the Reynolds number relevant for jet noise. It was concluded that at the very least the exit conditions are significant in allowing comparison between data sets. Likewise, the more recent report from Zaman[2], also restricted to subsonic jets, concludes that variations in the nozzle exit boundary layer could explain anomalies in acoustic measurements from seemingly equivalent operating conditions.

For supersonic jets, the recent report by Morris[3] presented some comparisons between model scale jet noise spectra and full scale data. Morris commented that, "The engine data does not roll off as fast as the scale model data at high frequencies. This could be due to a number of reasons, including the difference in turbulence exiting the nozzle due to the engine, or other noise sources from the engine." This would suggest that the correct characterization of the nozzle exit conditions is also of significance for supersonic jet noise particularly when active control methodologies are being developed at model scale.

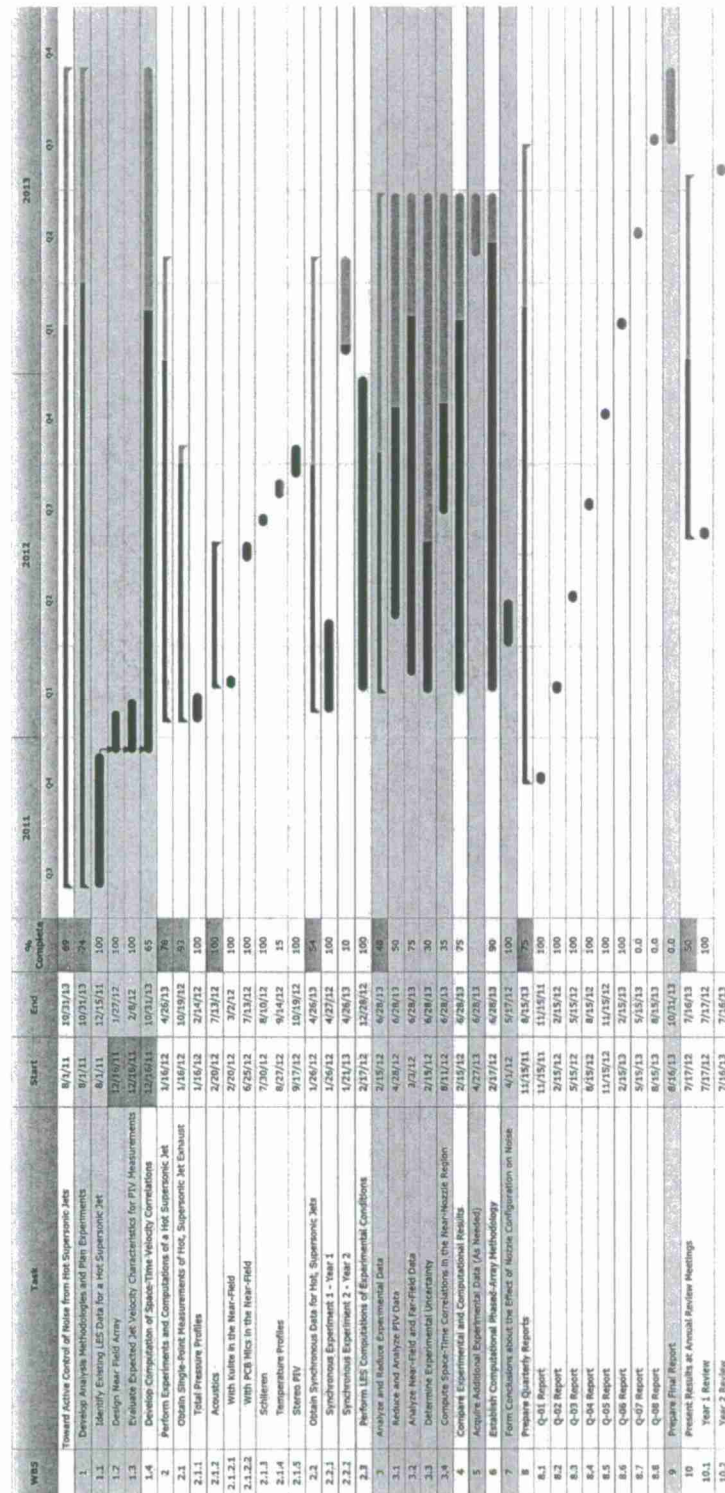


Figure 1. Project chart showing WBS items and current completion status as of the end of the reporting period.

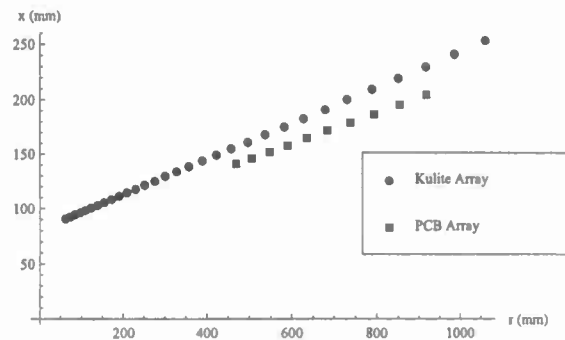


Figure 2. Location of the near-field microphones with comparison to the locations of the Kulite transducers in the February 2012 experiment.

A series of acoustic measurements were obtained to allow analysis of some of these issues. This data, acquired in July 2012, includes 12 B& K microphones on a far-field arc at 55 jet diameters from the nozzle as well as 10 PCB 112A22 ICP transducers in the near-field. The position of the PCB microphones, shown in Figure 2, was chosen to closely follow the line of Kulite transducers in the February 2012 experiment. Data was acquired for two nozzle configurations: (a) conic nozzle without the upstream centerbody, and (b) conic nozzle with the upstream centerbody. The stagnation pressure and temperature was varied to provide a range of NPR from 3.9 to 6.0 and T_{jet}/T_{∞} of 2.3 to 3.5. The run conditions for each event are provided in Table 1.

The inclusion of the upstream centerbody in the nozzle assembly is intended to replicate the engine core in a military nozzle. The aft end of the centerbody is located approximately $2.5 D_j$ upstream of the nozzle throat. The wake from the centerbody yields higher turbulence levels exiting the nozzle. This is evident in the far-field acoustics as shown in Figure 3. The increase is small but observable in the peak noise direction but more pronounced in the forward arc. To further this analysis, the CFD simulation and the anticipated PIV measurements will be used to aid in describing the turbulence levels present and the degree to which this effects the noise production mechanisms.

2.1.1 Near-Field Acoustic Characterization

The near-field acoustic measurements made in February 2012 using the Kulite array have been report previously and are also included in the 2012 INTERNOISE Conference Paper[4], so they are not going to be repeated here. The measurements using the PCB transducers (Figure 2) provide a second reference for comparison. Figure 4 shows the direct comparison between the Kulite and PCB measurements for the same jet conditions.

At first glance the comparison suggests dramatic differences. However, the measurements are in closer agreement when the influence of the setup is considered. The Kulite sensors were flush mounted in a 1 inch wide beam. Acoustically, the beam acts as a finite baffle that alters the frequency response of the installed sensor. Given the acoustic speed to be approximately 330 m/s, the width of the beam corresponds to a $1/2$ -wavelength at a frequency of 6500 Hz. For a finite baffle, a pressure doubling is expected for frequencies higher than the $1/2$ -

Conic with Centerbody

Date	P _{atm} (psi)	T _j (deg. F)	P _o (psi)	Mach	NPR	T Ratio	Event
7/10/2012	14.375562	1398.163491	121.042021	1.742956	5.214842	3.448	5
7/10/2012	14.375425	1342.594434	121.234251	1.743389	5.22159	3.339	6
7/10/2012	14.375456	1109.583585	121.094518	1.741094	5.216709	2.901	7
7/10/2012	14.374967	1000.044245	121.072384	1.740227	5.216059	2.696	8
7/10/2012	14.375403	900.567075	121.060892	1.739453	5.215546	2.508	9
7/10/2012	14.375714	809.75283	121.043961	1.738722	5.214858	2.338	10
7/10/2012	14.375367	1204.273774	121.012914	1.741424	5.213883	3.062	11
7/10/2012	14.390736	1403.806321	83.484092	1.551514	3.904342	3.400	12
7/10/2012	14.390461	1355.352358	83.787458	1.552894	3.914972	3.310	13
7/10/2012	14.389785	1212.535094	83.955281	1.552588	3.920905	3.048	14
7/10/2012	14.389661	1098.50934	84.197269	1.552993	3.929373	2.839	15
7/10/2012	14.389623	1002.072642	83.609451	1.54857	3.908896	2.662	16
7/10/2012	14.389818	915.111415	84.073257	1.550565	3.925012	2.504	17
7/10/2012	14.390414	805.305472	83.903022	1.548525	3.918973	2.304	18
7/10/2012	14.389518	1196.742642	85.356678	1.560796	3.969721	3.016	19
7/10/2012	14.383065	1206.618868	100.242293	1.64306	4.488994	3.034	20
7/10/2012	14.376516	1194.603019	114.391514	1.711757	4.983052	3.011	21
7/10/2012	14.370759	1211.330283	129.787898	1.778679	5.520823	3.041	22
7/10/2012	14.365041	1211.29717	143.121485	1.831111	5.987074	3.039	23

Conic without Centerbody

Date	P _{atm} (psi)	T _j (deg. F)	P _o (psi)	Mach	NPR	T Ratio	Event
7/11/2012	14.411241	1406.686667	120.721317	1.740322	5.193295	3.478	24
7/11/2012	14.410666	1348.769623	121.04801	1.741336	5.204776	3.366	25
7/11/2012	14.409945	1187.632885	121.033159	1.740123	5.204455	3.061	26
7/11/2012	14.410198	1103.060283	121.096799	1.739783	5.206615	2.902	27
7/11/2012	14.41005	1013.507736	121.332702	1.740166	5.214806	2.732	28
7/11/2012	14.410342	902.982642	121.338609	1.739399	5.214972	2.525	29
7/11/2012	14.409662	802.558774	121.694498	1.740261	5.227535	2.336	30
7/11/2012	14.399732	1192.748679	143.849986	1.832433	6.000418	3.051	31
7/11/2012	14.40591	1203.090189	130.160646	1.778844	5.52272	3.065	32
7/11/2012	14.409827	1198.520566	117.997351	1.726849	5.099088	3.052	33
7/11/2012	14.417322	1204.078491	100.782909	1.644576	4.49942	3.057	34
7/11/2012	14.423409	1202.674135	88.278111	1.576668	4.064092	3.052	35
7/11/2012	14.425184	1396.764245	83.84466	1.552413	3.909924	3.405	36
7/11/2012	14.425124	1357.414423	84.482442	1.555852	3.93206	3.331	37
7/11/2012	14.424208	1216.224327	84.341533	1.553732	3.927346	3.072	38
7/11/2012	14.424385	1098.702075	84.333583	1.552593	3.927038	2.855	39
7/11/2012	14.424022	1001.747453	84.431494	1.5523	3.930502	2.678	40
7/11/2012	14.423557	798.189528	84.067917	1.548291	3.918001	2.304	42
7/11/2012	14.423737	907.192264	84.203746	1.550084	3.922667	2.504	43

Table 1. Nozzle operating conditions for the July 2012 data set.

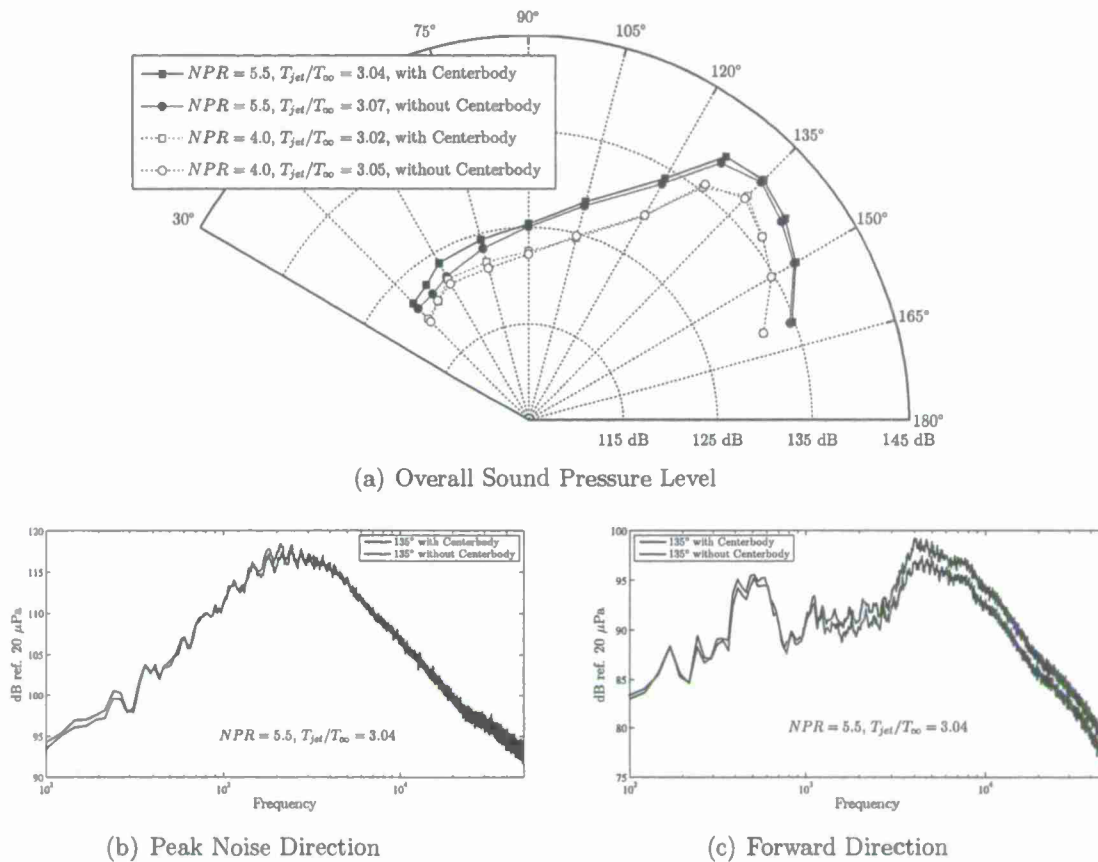


Figure 3. Comparison of the far field acoustics with and without the upstream centerbody in the nozzle assembly.

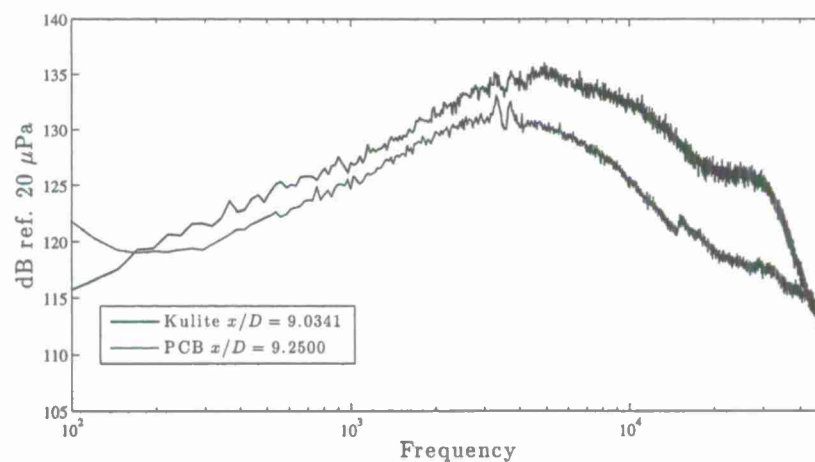


Figure 4. Comparison of Kulite and PCB measurement of near-field acoustics for the same jet conditions

wavelength equivalent and a smaller increase for lower frequencies. Looking at Figure 4 this is exactly the situation. For frequencies above 6500 Hz, the Kulite's report ≈ 6 dB above the PCB measurement. For lower frequencies, the Kulites report about 1-2 dB above the PCB. Therefore, the discrepancy is linked directly to the frequency response of the finite baffle around the Kulite.

Neither the Kulite nor the PCB sensors have a detailed frequency response from the manufacturer. In order to correct the spectral measurements for the frequency response of the assembled sensors, a separate experiment is being performed using a 1 inch subsonic cold jet. The flush mounted Kulite, the PCB transducer, and a calibration traceable B&K 1/4-inch microphone will be placed as equivalent (x, r) positions separated by 120 degrees in azimuth. The B&K microphone will be used to generate a frequency response function for both the Kulite and PCB sensors. Finally, the February 2012 and July 2012 data will be corrected with the appropriate transfer functions to produce a final data set that will be made available for post processing and analysis.

2.2 Exploring Aeroacoustic Source Terms

One of the inherent features of an acoustic analogy is that the result gives a representation of a *non-unique* acoustic source that is consistent with the measured far-field sound.[5] This is true even of recent computational efforts using F-W&H methods to propagate near-field pressure fluctuations to a far-field observer through the application of Green's function integrals. The drawback is that much of the sound generation is hidden from exploration.

Various vortex sound methods have been explored over the years as an alternative or enhancement to acoustic analogies. The "rational" approach of Seiner[6] falls into this category and suggests a noise source indicator resulting from the phase difference between the strain and rotation rates acting on the vorticity. To arrive at this suggestion, Seiner applied a double divergence directly to the incompressible Reynolds stress giving

$$\frac{\partial^2 u_i u_j}{\partial x_i \partial x_j} = -\varepsilon_{ijk}(s_{ij}\omega_k + r_{ij}\omega_k). \quad (1)$$

This neglected variations in the dynamic pressure. The suggestion Seiner made was that any phase shift between the strain and rotation rates in this sum would give rise to sound production.

To date, we have re-derived the expression with the dynamic pressure included as presented in the Fiévet *et al.* abstract for the 2013 Aeroacoustics conference (included in the previous quarterly report):

$$\frac{\partial^2 u_i u_j}{\partial x_i \partial x_j} = \varepsilon_{ijk}(s_{ij}\omega_k + r_{ij}\omega_k) + \left(\frac{\partial u_i}{\partial x_j}\right)^2. \quad (2)$$

Now, we are working to evaluate this expression using the HRLES CFD data set. By developing the post processing tools for the analysis, we are establishing the building blocks to analyze the experimental data that is anticipated from the time-resolved PIV experiments. We are also establishing the necessary dynamic range for the experimental measurements to allow investigation of the acoustic source terms.

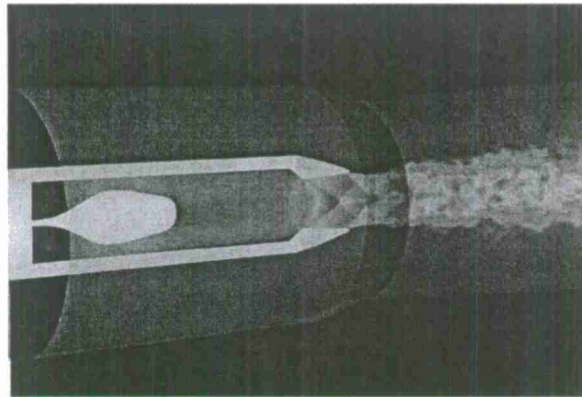


Figure 5. Illustration of the internal geometry rendered in the CFD simulation showing the upstream centerbody which replicates the experimental setup.

Conic $M_d = 1.74$ Nozzle	T_0 (K)	P_0 (kPa)	T_∞ (K)	P_∞ (kPa)	T_0/T_∞	NPR
Over-Expanded	1005	401.76	300	101.33	3.35	3.96
Pressure Matched	1005	531.33	300	101.33	3.35	5.24

Table 2. Stagnation conditions prescribed for the two CFD simulations.

2.2.1 Time-Resolved CFD Data Set for Aeroacoustic Source Analysis

Time resolved data using the Hybrid RANS/LES CFD simulations have been compiled for two jet conditions consistent with the experimental measurements ongoing in this program. Both simulations use the conic jet nozzle with the upstream centerbody as illustrated in Figure 5. The stagnation conditions prescribed for the simulation are listed in Table 2. Additional details about the CFD simulation are given in the AIAA Paper presented at the recent Aerospace Sciences Meeting.[10]

Having run the simulation to convergence, time resolved data was generated for post processing by saving solution snapshots at the equivalent of 200 kHz. A total of three hundred snapshots were saved for each jet condition. All of the data was saved in standard Plot3D format. The solution files contain U_x , U_y , U_z and the thermodynamic variables ρ , P , T . The data has been archived and made available to the other team members for further analysis.

To reduce the file sizes, the full CFD solution domain was not saved in the database. The restricted domain includes 0.0 to 0.8 meters (0 to $15.3 D_j$) in the axial extent and out to 0.22 meters ($4.1 D_j$) in the radial extent as illustrated in Figure 6. This selected region represented 5 zones from the CFD solution. To ease post processing, the 4 outer zones were combined in the reduced output such that 2 zones remained: the inner H-grid in the jet core and an outer O-grid arranged azimuthally as shown in Figure 7

The acoustic and turbulence terms of interest include both mean and fluctuating quantities. Therefore, a "mean" value is needed as the base flow. The simulation was not run long enough to generate converged point-statistics. Instead the 300 available snapshots were

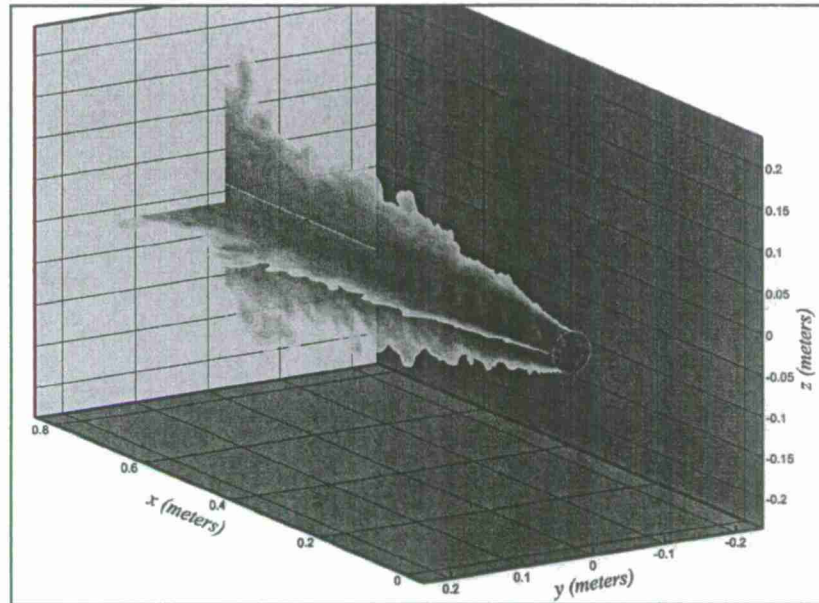


Figure 6. Illustration of computational domain saved in the time-resolved output files for further processing.

averaged followed by azimuthal averaging to generate the final “mean-flow” illustrated in Figure 8.

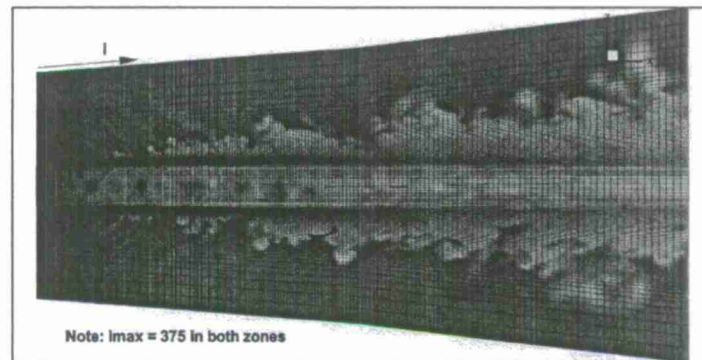
Nozzle exit velocity profiles were extracted from the mean flow calculation. These are of interest due the observation by many authors that the jet noise is measurably effected by the inner-nozzle flow conditions. The nozzle exit boundary layer and turbulence levels are an indicator of these inner-nozzle effects. In Figure 9 it is clear that the presence of shocks inside the nozzle disturbs the radial ρU profile in the over-expanded case.

2.2.2 Computation of Acoustically Relevant Source Terms

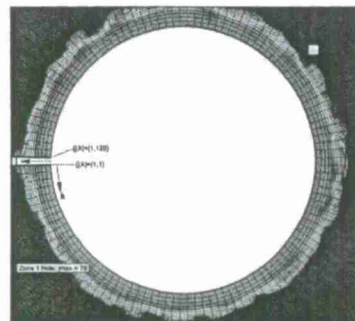
Computing quantities relevant to acoustic generation (i.e. Eq. (2)) requires second order derivatives. A code for computing these derivatives was written based on the text of Anderson[11]. This accounts for the local divergence of the grid coordinates in computing the derivatives in a Cartesian coordinate system. The code for performing the calculations is included here as Appendix A. Subroutines were written to perform the necessary calculation of the local Jacobian and central differencing. With these it is possible to construct any compound derivative of interest. As an example, Figure 10 shows the result of computing $\varepsilon_{ijk} S_{ij} \omega_k$ on one of the instantaneous snapshots. In the coming months, this data will be explored further.

2.2.3 Possible Entropic Effects

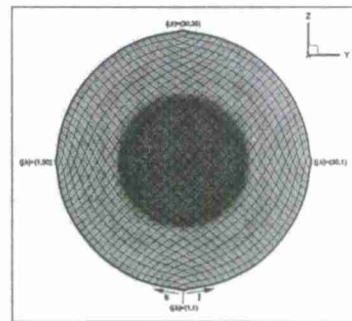
Vortex sound based methods assume incompressible flow which is not an applicable assumption for the jet conditions under study in this work. Nevertheless, it is still of value to



(a) Symmetry Plane



(b) Cross-Plane Zone 1



(c) Cross-Plane Zone 2

Figure 7. Illustrations of the computational grid space retain in the reduced data set for post-processing.

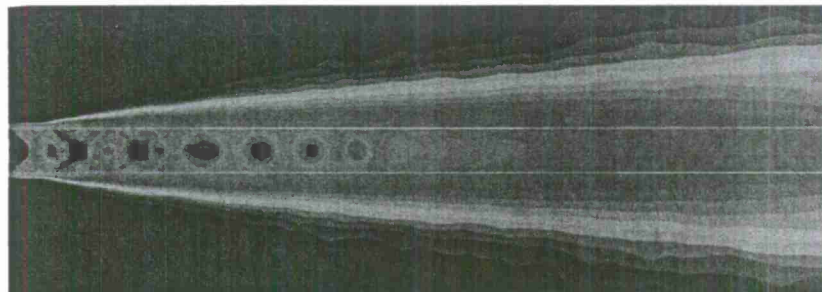


Figure 8. Symmetry plane contour of computed mean axial velocity illustrating the "mean" flow computed from the available 300 time-resolved snapshots.

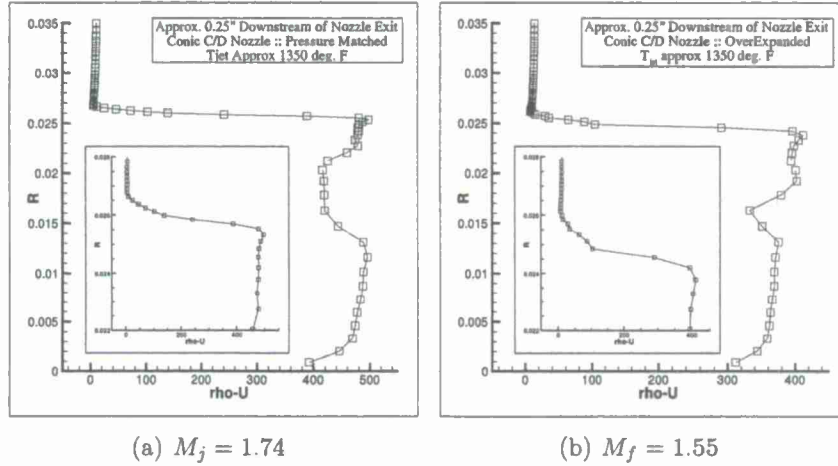


Figure 9. Nozzle exit profiles of ρU_x (kg/m² · s) for the two NPR's simulated.

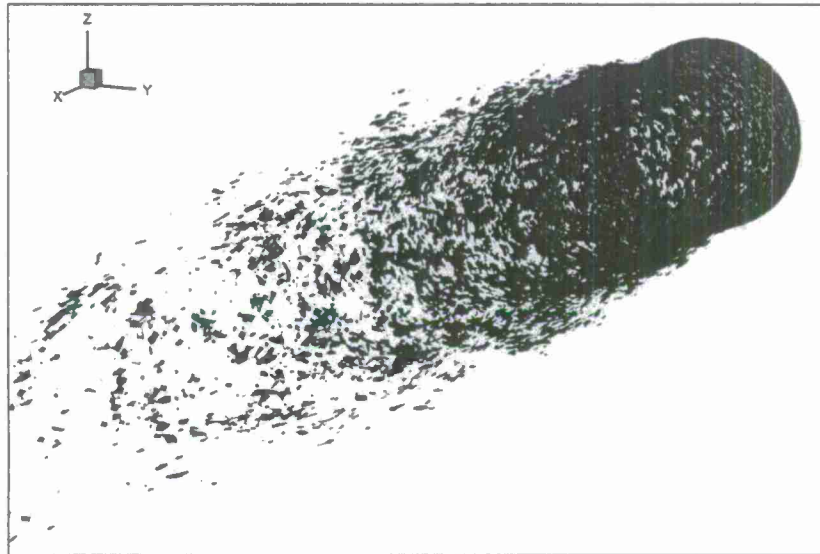


Figure 10. Snapshot of $\epsilon_{ijk} S_{ij} \omega_k$ which appears to be largely isolated to the shear layer.

evaluate such second-order divergence terms as they will still represent source-like behavior. But the compressible nature of the flow needs to be better understood. One possible method of addressing this issue is to investigate other noise source effects that are relevant to compressible flows such as entropy variations.[7] The entropy contribution has been demonstrated to be significant in some cases.[8, 9] The CFD database includes the local thermodynamic variables allowing exploration of the significance of these effects in sound generation for the current jet conditions of interest.

2.3 Updates on Computational Phased Array Work

Significant progress has been achieved on the phased array calculation front since the last quarterly report. The results were presented in the AIAA-ASM conference publication and presentation included in Appendix C and D. These calculations have been performed on the conic nozzle configuration with the centerbody operating at pressure matched conditions. One important result that emerged from our phase array studies was that it would be optimal to use different array sizes depending on the $1/3^{\text{rd}}$ octave band center frequency of interest. Beamforming calculations at lower frequencies will make use of an array of larger size than calculations at higher frequencies. Since the CFD calculations have a high frequency limit based on grid resolution at ~ 10 kHz, we have selected the 2kHz, 3.15 kHz, 5 kHz and 8 kHz frequencies as the focus for future studies.*

Most beamforming calculations to this point have used 45 microphones in a multiple-arm logarithmic spiral arrangement (five spiral arms, each containing nine microphones). However, it was determined that for two lower frequencies, (2 kHz and 3.15 kHz), where a larger array size is warranted, future beamforming calculations will make use of 99 microphones (nine spiral arms, each containing 11 microphones). This is because a larger array requires more microphones in order to avoid aliasing issues. The beamforming calculations at the 5 kHz and 8 kHz center frequencies will use the 45 microphone array; the physical dimension of the array used for the 8 kHz calculations will be smaller than that used for the 5 kHz calculation. These microphone arrays will henceforth be referred to as the small, medium and large aperture spiral array (SASA, MASA and LASA).

Finally, in order to examine the effect of the observer viewing angle on the perceived location of the acoustic sources, the beamforming calculations will be conducted with phased arrays rotated to various azimuthal angles. At each azimuthal location, the phase center of the array will be located 72 inches from the aim point; the aim point is located 25 inches downstream of the nozzle exit on the axis. Figure 11 shows the 3D view of three (out of 9) of the azimuthally oriented array layouts (at 135° , 90° , and 45° to the upstream jet axis). The phase centers for all 9 arrays that will be considered are shown.

*It is relevant to note that other research groups performing computational beamforming have presented results for center frequencies as high as 40 kHz without any verification that their computational methodology and grid are capable of resolving these high frequencies. Direct comparison with experimental data in the current work served as a validity check on our reported results.

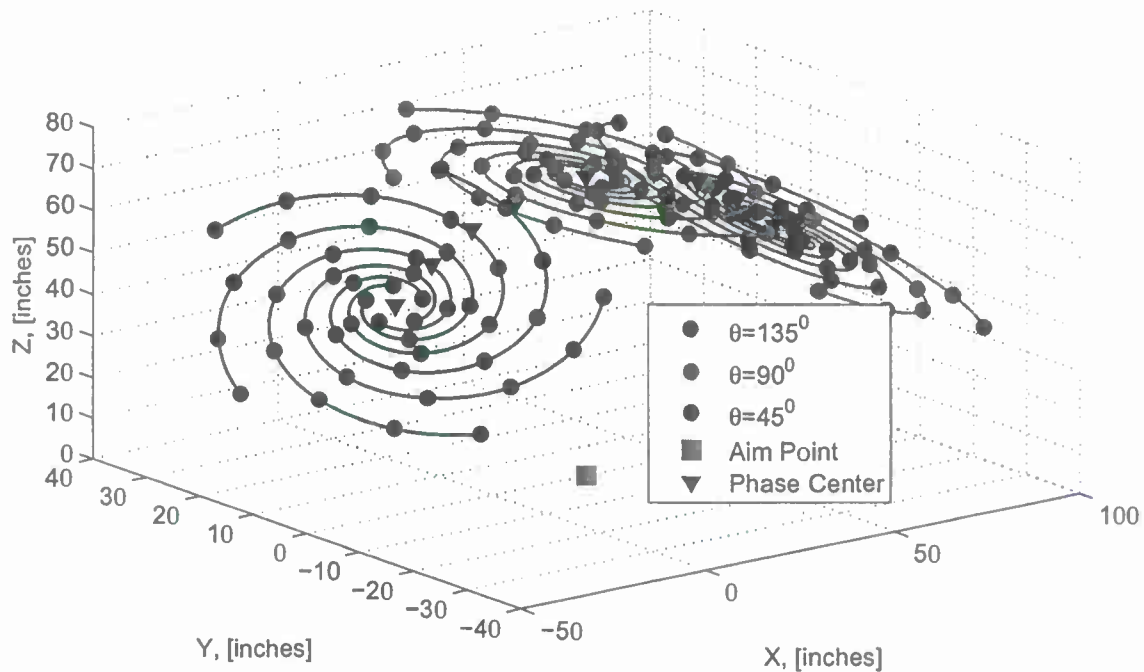


Figure 11. Phased arrays rotated at various angles with reference to the jet axis.

2.4 Stereo PIV Analysis of Jet Characteristics

The last quarterly report noted the acquisition of standard 3-component PIV measurements using the pH stabilized seeding system. Image data were acquired using a pair of PCO.Edge SCMOS cameras with double exposure capability. The jet flow was seeded with 0.3 micron alumina particles. Illumination of the flow was achieved using a NewWave ND:Yag Gemini PIV laser with 150 mJ/pulse. Light sheet forming optics yielded a light sheet thickness of approximately 1 mm. The ambient air was not actively seeded; however, the recirculation in the anechoic chamber was sufficient to yield reasonable seed density in the entrained air.

The entire imaging system was erected on a precision traverse system that has been laser aligned to travel parallel to the geometric axis of the nozzle system as shown in Figure 12. This allowed the entire measurement entry to be completed without any setup changes.

The experimental measurement involved image acquisition at four different axial stations. Each imaging region overlapped slightly to allow alignment of the vector data during post processing. At each axial station, 3 acquisition events were performed yielding 300 image pairs each to give a total of 900 image pairs per station. The full measurement region spans from 1.0 to 8.25 D_j in the axial direction and out to 0.9 D_j in the radial direction. The computed mean velocity for the entire domain is shown in Figure 13 with the individual imaging zones outlined to show the overlap.

For this PIV dataset the conic $M_j = 1.74$ nozzle was used without the upstream center-body. A stagnation temperature of 1355 °F and $NPR = 3.934$ were computed by averaging the conditions for all 12 image acquisition events. A standard deviation in the mean was

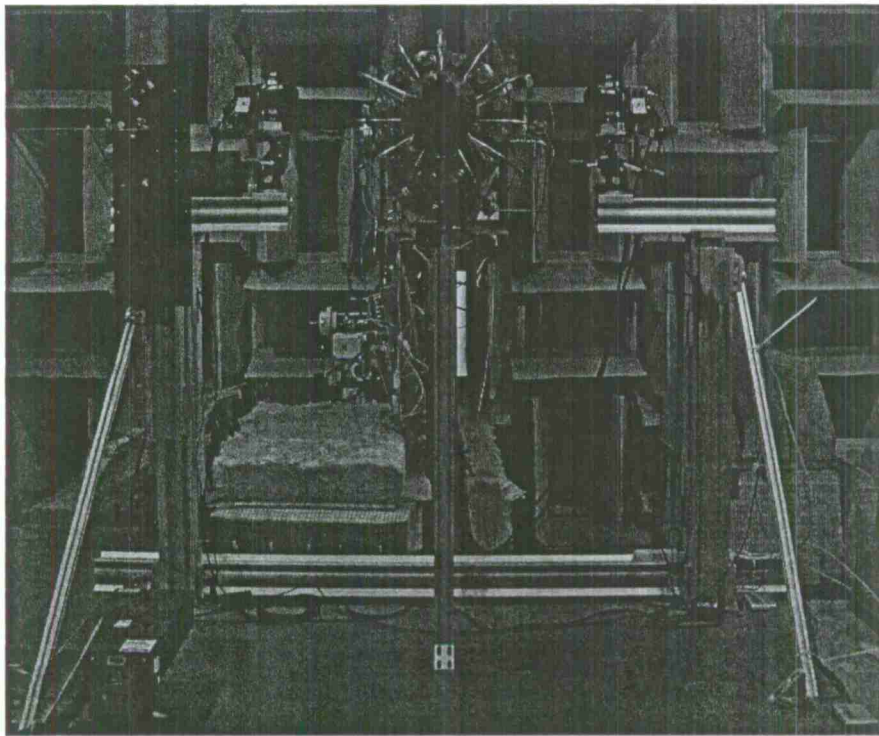


Figure 12. Stereo PIV setup in the NCPA Anechoic Jet Laboratory. All optics are supported from the large breadboard at the bottom of the image which is attached to a precision traverse allowing re-positioning with better than 0.01 inch accuracy.

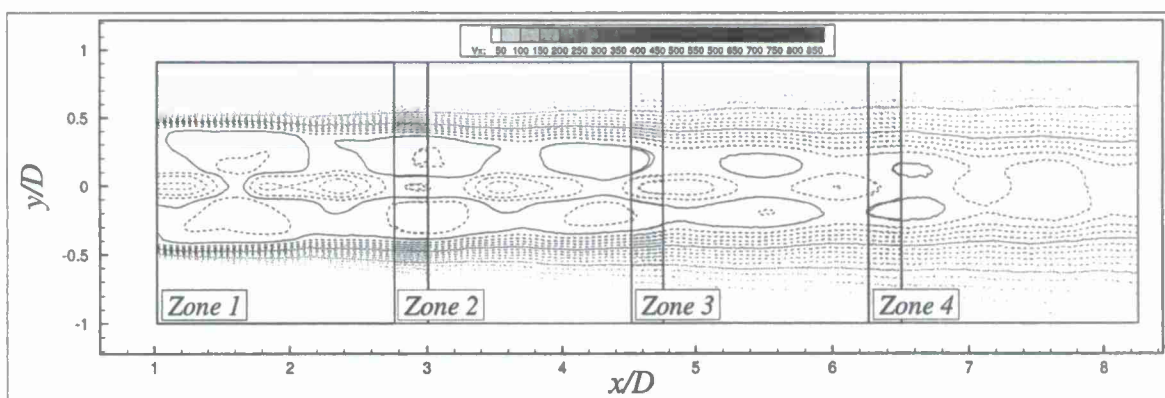


Figure 13. Mean streamwise velocity obtained from standard 3-component PIV measurement of the jet plume.

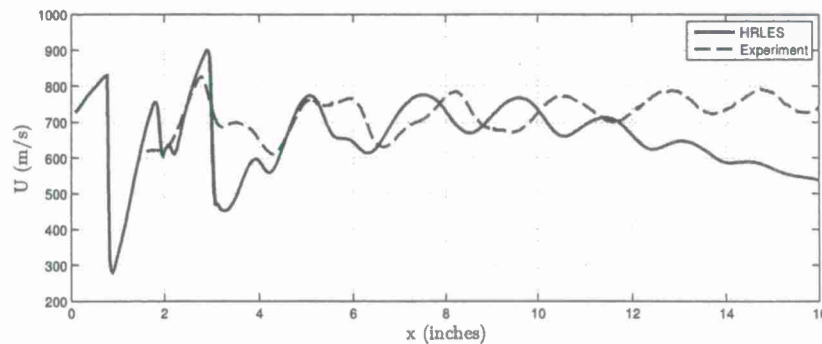


Figure 14. Comparison of the centerline streamwise velocity between the HRLES calculations and PIV data for the conic nozzle without the centerbody operating at overexpanded conditions.

computed from the variance in the average conditions for each individual event. Then an estimate of the uncertainty in the jet conditions was computed as σ/\sqrt{N} where $N = 12$ events. In this way, the estimated uncertainty in T_0 was found to be $\pm 2^\circ\text{F}$ and in NPR was found to be ± 0.002 .

2.4.1 Preliminary Results

Analysis of the image data was completed using DaVis 8. Image pairs were analyzed using a multi-pass method with 128×128 pixel, 0% overlap square windows for the first 4 passes and 32×32 pixel, 50% overlap adaptive windows for the final 2 passes. On each pass, a peak Q ratio limit of 1.3 was applied and a two pass median filter was used to remove erroneous vectors. The final analysis step applied a peak Q ratio limit of 1.1 and again applied a two pass median filter. After completing the image analysis, the vector data was post processed to center the vertical extent on the measured jet axis, and the entire data set was saved into Plot3D format.

Figure 14 shows a comparison of the experimental and CFD results for the centerline velocity decay. There is qualitative agreement between the experiments and CFD, as far as the location of shock cells are concerned, for approximately 6-8 inches downstream of the nozzle exit. Farther downstream there appears to be something similar to a "phase-shifting" between the simulations and experiments. This can be explained by the progressive coarsening of the CFD grid in the downstream direction and was expected.

Figure 15 shows a comparison of the mean streamwise velocity profiles at three axial stations. The experiments and simulations show good agreement with one another at the upstream locations ($x = 3.0$ inches and $x = 5.0$ inches). This agreement starts worsening at axial stations farther downstream ($x = 8.0$ inches) where the simulations start showing a more rapid decay of the streamwise velocity as compared to the experiments (again due to the grid coarsening). The velocity defect at the centerline, that is seen in both experiments as well as the simulations, is a result of the slip plane.

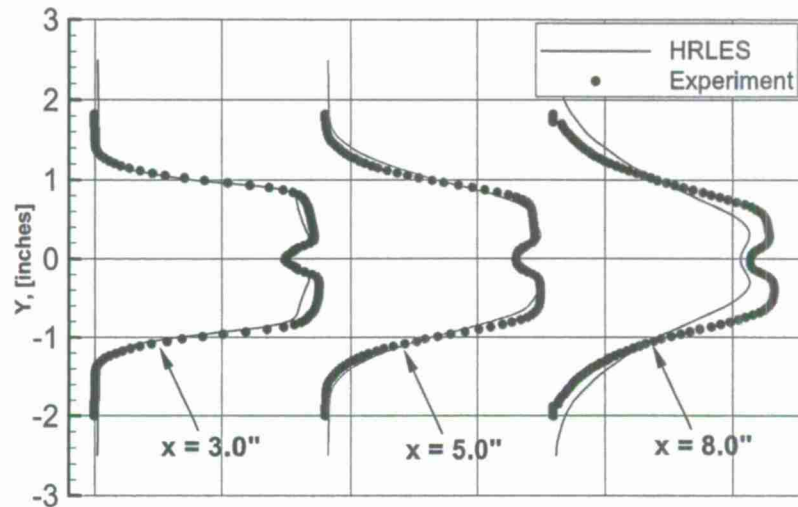


Figure 15. Comparison of the mean streamwise velocity profile at various axial locations between the HRLES calculations and PIV data for the conic nozzle without the centerbody operating at overexpanded conditions.

2.5 Progress on HDR-PIV Diagnostic Efforts

2.5.1 DEVOLS Processing for HDR-PIV

A method for obtaining enhanced signal-to-noise ratios with the high-dynamic-range particle image velocimetry (HDR-PIV) has been established. This dynamic evaluation via ordinary least squares (DEVOLS) method has demonstrated measured improvement over standard PIV for a simulated data set. Figure 16 shows a measurable improvement over standard PIV analysis for a simulated Hamel-Oseen vortex. Complete details of the DEVOLS method and results were presented at the recent 2013 AIAA Aerospace Sciences Meeting (Paper 2013-0774 attached in Appendix E).

2.5.2 Current Status of Experimental Efforts

Efforts in Year 1 to acquire time-resolve PIV data were unsuccessful due to unanticipated operational issues with the Cordin camera system. The camera was sent to Cordin for service and was returned to Auburn U. in December, 2012. The pulse-burst laser system and camera were brought to NCPA by Auburn graduate student Bryan Brock to initiate Year 2 testing during the Spring months. Setup of the experiment is currently underway.

The time-resolve CFD data can serve as a means to develop analysis methods that will be used on the high-frame-rate PIV data anticipated to be generated in the coming months. As such, the CFD solution file was used to select a region of interest near the nozzle exit and generate simulated PIV data.

The measurement domain shown in Figure 17 was chosen as a trade-off between imaging capability and measurement goals. As noted in Section 1.1, the near-nozzle flow conditions are of primary interest in the current effort. To maximize the optical setup, a 1.5 inch field of

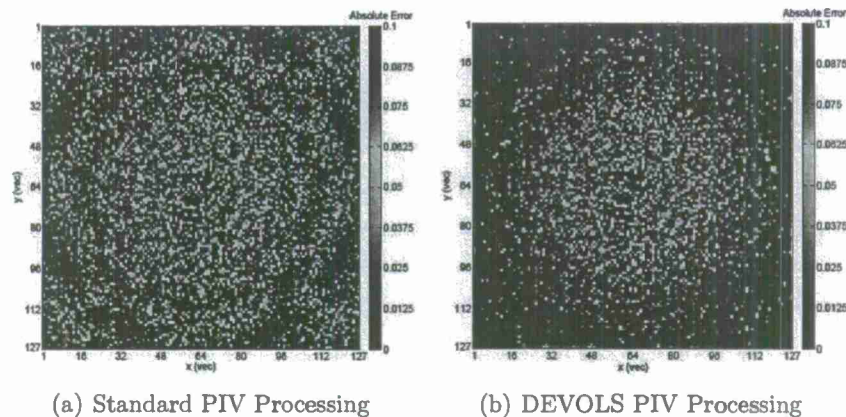


Figure 16. Illustration of the reduced absolute error afforded by application of DEVOLS processing to a simulated time-resolved PIV data set.

view was chosen giving a suitable spatial resolution to resolve the high-shear layer gradients in this region of the jet. Because of the high-shear rates in the region of interest, the high-dynamic-range analysis methods developed in Year 1 will be well suited for analyzing the image data, and the analysis of any phase misalignment between the shear and rotation rate components of the noise source should be observable.

3 Technical/Cost Status & Problem Areas

3.1 Status Summary

Overall, the status of the program is on track and progress is being made in all areas of the research effort. As we generate experimental data and develop the diagnostic efforts, opportunities for collaboration with other jet noise reduction research teams are being identified. We have had discussions with Dr. Kent Gee concerning the sharing of our acoustic data for comparison to his full scale acoustic data. We have also had discussions with Dr. Todd Lowe concerning the possibility of utilizing his laser diagnostic system to measure the jet exhaust characteristics in the NCPA Anechoic Jet Lab. These collaborative opportunities will be developed further during the next reporting period.

3.2 High-Frame-Rate Camera for HDR-PIV

Following service by Cordin, the camera was brought back to NCPA in January 2013 for a second attempt at data collection. Initial results with the camera are positive. The software issues that previous caused the system to lock-up have been eliminated, and the relative focus of the 8 individual imaging units seems to be in closer agreement. The aperture limitations of the optical system are still an inherent drawback of the system. A large aperture 135mm lens has been purchased and is currently being used as the primary lens allowing greater light collection. Currently the system is being readied for measurement in the next week. By performing measurements early in the semester we hope to identify any remaining issues

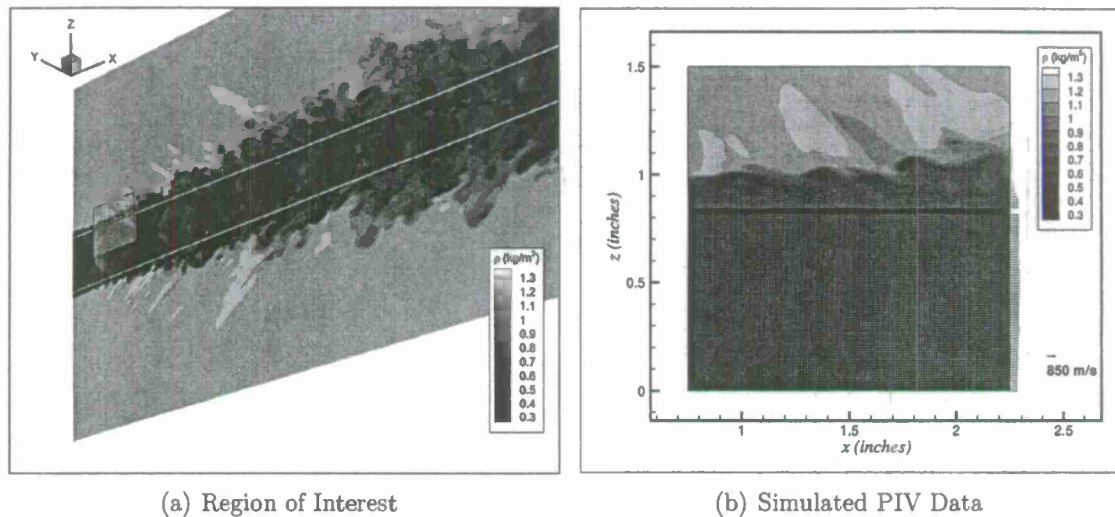


Figure 17. Illustration of the simulated PIV data extracted from the CFD solution.

and be able to address them in order to guarantee a successful synchronized PIV/Acoustics measurement later in the Spring.

Contact has been made with the manufacturer of a new high speed camera, the Kirana. Its capabilities exceed that of the Cordin. The manufacturer has responded with great interest in supporting a demonstration of the Kirana system in April which will provide us with an opportunity to acquire time-resolved PIV measurements with a second imaging system.

3.3 Other Potential Imaging Diagnostic Options

Plenoptic imaging for volumetric PIV is a technology that is in development by our Auburn partners. Measurements were obtained with Auburn's Plenoptic camera last Fall. Initial results of the analysis are very promising. As a result, we are planning to perform a second experiment with the Plenoptic PIV system during the next reporting period with more thorough setup and calibration allowing a detailed analysis of the flow.

4 Publications, Meetings, and/or Travel

4.1 Running List of Publications Produced

- Baars, W., Tinney, C., and Wochner, M. "Nonlinear Noise Propagation from a Fully Expanded Mach 3 Jet." *50th AIAA Aerospace Sciences Meeting*, Paper 2012-1177.
- Murray, N., Lyons, G., Tinney, C., Donald, B., Baars, W., Thurow, B., Haynes, H., and Panickar, P. "A Laboratory Framework for Synchronous Near/Far-Field Acoustics and MHz PIV in High-Temperature, Shock-Containing Jets." *Proceedings of the Internoise 2012/ASME NCAD Meeting*, Paper ASME/NCAD-1270.

- Baars, W. and Tinney, C. "Scaling Model for Nonlinear Supersonic Jet Noise." *Bulletin of the American Physical Society*, 57:17, Abstract D24:8, San Diego, CA. <http://meetings.aps.org/link/BAPS.2012.DFD.D24.8>. [included in Appendix B]
- Panickar, P., Erwin, J., Sinha, N., Murray, N., and Lyons, G. "Localization of Acoustic Sources in Shock-Containing Jet Flows Using Phased Array Measurements." *51st AIAA Aerospace Sciences Meeting*, Paper 2013-0613. [included in Appendix C and D]
- Haynes, R., Brock, B., and Thurow, B. "Application of MHz Frame Rate, High Dynamic Range PIV to a High-Temperature, Shock-Containing Jet." *51st AIAA Aerospace Sciences Meeting*, Paper 2013-0774. [included in appendix E]
- Fiévet, R., Tinney, C., Murray, N., Lyons, G., and Panickar, P. "Acoustic Source Indicators using LES in a Fully Expanded and Heated Supersonic Jet." accepted for presentation at the 2013 AIAA Aeroacoustics Conference.
- Baars, W., and Tinney, C. "Quantifying Shock-Type Acoustic Waveform Structures Emitted by a Fully-Expanded Mach 3 Jet." accepted for presentation at the 2013 AIAA Aeroacoustics Conference.
- Baars, W. and Tinney, C. "Quantifying Supersonic Jet Noise Crackle." accepted for presentation at the *2nd Symposium on Fluid-Structure-Sound Interactions and Control*, 2013.
- Baars, W., Tinney, C., and Wochner, M. "Nonlinear Distortion of Acoustic Waveforms from High-Speed Jets." *J. Fluid Mech.* [in review]

5 Planned Activities for Next Reporting Period

- Continue analysis of noise source indicators using the computational simulation data.
- Bring the uncertainty analysis efforts up to date.
- Conduct year 2 experimental efforts to measure acoustic source quantities.
- Reach out to other JNR program participants to foster potential collaboration.

6 Cited References

- [1] Viswanathan, K., "Aeroacoustics of hot jets," *Journal of Fluid Mechanics*, Vol. 516, 2004, pp. 39-82.
- [2] Zaman, K., "Effect of Nozzle Exit Conditions on Subsonic Jet Noise," *17th AIAA/CEAS Aeroacoustics Conference*, Paper No. 2011-2704, 2011.
- [3] Morris, P. J., "The Reduction of Advanced Military Aircraft Noise," Final Report SERDP Project WP-1583, Penn State University, 2011.

- [4] Murray, N., Lyons, G., Tinney, C. E., Donald, B., Baars, W., Thurow, B., Haynes, H., and Panickar, P., "A Laboratory Framework for Synchronous Near/Far-Field Acoustics and MHz PIV in High-Temperature, Shock-Containing, Jets," *Proceedings of the Inter-noise 2012/ASME NCAD Meeting*, Paper No. ASME/NCAD-1270 [invited], New York City, NY, August 2012.
- [5] Freund, J., "Noise Sources in a Low-Reynolds-Number Turbulent Jet at Mach 0.9," *Journal of Fluid Mechanics*, Vol. 438, 2001, pp. 277–305.
- [6] Seiner, J. M., "A New Rational Approach to Jet Noise Reduction," *Theoretical and Computational Fluid Dynamics*, Vol. 10, 1998, pp. 373–383.
- [7] Peter, A. C., "Entropic Effects in Sound Generation," *Basic Aerodynamic Noise Research*, edited by I. R. Schwartz, Paper No. NASA-SP-207, 1969.
- [8] Colonius, T. and Lele, S. K., "Computational Aeroacoustics: Progress on Nonlinear Problems of Sound Generation," *Progress in Aerospace Sciences*, Vol. 40, No. 6, 2004, pp. 345–416.
- [9] Wang, M., Freund, J. B., and Lele, S. K., "Computational Prediction of Flow-Generated Sound," *Annual Review of Fluid Mechanics*, Vol. 38, 2006, pp. 483–512.
- [10] Panicker, P., Erwin, J., Sinha, N., Murray, N., and Lyons, G., "Localization of Acoustic Sources in Shock-Containing Jet Flows Using Phased Array Measurements," *51st AIAA Aerospace Sciences Meeting*, Paper No. 2013-0613, Grapevine, TX, 2013.
- [11] Anderson, J. D., *Computational Fluid Dynamics*, McGraw-Hill, 1995.

Appendix A: FORTRAN Code for Computing Derivatives from CFD Data

/Users/nathanmurray/ResearchRemote/Research/Analysis/computingDerivatives_1_001.f90 Page 1 of 9
 Saved: 1/31/13 1:37:00 PM Printed For: Nathan Murray

```

1 !-----
2 ! computingDerivatives_1_001.f90
3 !
4 ! Version 1.001
5 ! I have attempted to generalize the process of computing derivatives on a
6 ! computational grid space. This requires the calculation of the Jacobian
7 ! of the transformation between grid units and physical coordinates. By
8 ! placing all the specifics in subroutines and functions, the effort of
9 ! calculating a derivative is reduced to specifying the variable of interest
10 ! and the coordinate direction in which the partial derivative is desired.
11 ! Now, the function calls can be used to construct calculations involving
12 ! multiple derivatives.
13 !
14 ! Thanks to James Erwin (CRAFT Tech) for giving me the building blocks
15 ! to build this code.
16 !
17 ! Details of the computation of the grid metrics using the Jacobian can
18 ! be found in the CFD text by Anderson.
19 !
20 ! The remaining computation of interest would be second partials. This
21 ! code can easily be used to construct mixed second-partial
22 ! (i.e.  $d^2/dx dy$ ), but a savings in computational noise may be gained
23 ! if second-partial such as  $d^2/dx^2$  were computed in a single
24 ! step. However, this would require the addition of a new function that
25 ! would (a) compute derivatives of the local grid metrics AND (b) perform the
26 ! 1st order 2nd-central-difference ...
27 ! i.e.  $[ f(i+1) + f(i-1) - 2f(i) ] / [ dx^2 ]$ 
28 ! This step has not been completed in this version. For now, second-partial
29 ! can be obtained by twice applying the partialOne[] function.
30 !
31 ! (28 Jan. 2013 :: Nathan Murray)
32 !-----
33
34 PROGRAM computingDerivatives
35
36   IMPLICIT NONE
37
38   TYPE func
39     REAL, DIMENSION(:,:,:), POINTER :: f ! can be either grid or function data
40     INTEGER :: ni, nj, nk, nf
41   END TYPE
42
43   TYPE neighborIDs
44     INTEGER :: zID ! Zone number of neighbor
45     INTEGER :: ii ! i-index of neighbor
46     INTEGER :: jj ! j-index of neighbor
47     INTEGER :: kk ! k-index of neighbor
48     LOGICAL :: isBoundary ! TRUE if neighbor is the boundary
49                     ! FALSE for internal nodes
45   END TYPE
46
47   INTEGER :: i, j, k, n, ng, ni, nj, nk, nvar, f
48   INTEGER :: ii, jj, kk
49   INTEGER :: ll, mm, nn
50
51   INTEGER, DIMENSION(3), PARAMETER :: uvwID = (/2,3,4/)
52
53   TYPE(func), DIMENSION(:), POINTER :: gr0 ! the grid
54   TYPE(func), DIMENSION(:), POINTER :: gfun ! the flow variables
55   TYPE(func), DIMENSION(:), POINTER :: dgfun ! the computed derivative
56
57   TYPE(neighborIDs), DIMENSION(3,2) :: nID

```

/Users/nathanmurray/ResearchRemote/ResearchAnalysis/computingDerivatives_1_001.f90 Page 2 of 9
 Saved: 1/31/13 1:37:00 PM Printed For: Nathan Murray

```

64 LOGICAL :: onBoundary
65
66 CHARACTER(1024) :: fn
67
68 WRITE(*,'(A)') "Reading Data"
69
70 WRITE(fn,'(A)') "VolumeData_ConicWithCB_OverExp/SubsetXYZFile.bin"
71 OPEN(UNIT=101,FILE=TRIM(fn),STATUS="old",FORM="unformatted",ACTION="read")
72 READ(101) ng
73 WRITE(*,'(A,I12)') "Number of input zones =", ng
74 ALLOCATE(gr0(ng))
75 READ(101) (gr0(n)%ni,gr0(n)%nj,gr0(n)%nk,n=1,ng)
76 DO n=1,ng
77   ALLOCATE(gr0(n)%f(gr0(n)%ni,gr0(n)%nj,gr0(n)%nk,3))
78   READ(101) gr0(n)%f
79 ENDDO
80 CLOSE(101)
81 WRITE(*,'(A)') "Grid File Loaded"
82
83 WRITE(fn,'(A)') "VolumeData_ConicWithCB_OverExp/Snapshot_001.bin"
84 OPEN(unit=101,file=TRIM(fn),FORM='unformatted',STATUS='old',ACTION='read')
85 READ(101) ng
86 IF (ng.NE. SIZE(gr0)) STOP "grid and function file not same number of blocks"
87 ALLOCATE(gfun(ng))
88 READ(101) (gfun(n)%ni,gfun(n)%nj,gfun(n)%nk,gfun(n)%nf,n=1,ng)
89 DO n=1,ng
90   ALLOCATE(gfun(n)%f(gfun(n)%ni,gfun(n)%nj,gfun(n)%nk,gfun(n)%nf))
91   READ(101) gfun(n)%f
92 END DO
93 CLOSE(101)
94 WRITE(*,'(A)') "Solution File Loaded"
95
96 ! Convert the (x,y,z) grid data to (x,r,phi) ... READ discussion of issues
97 ! in the subroutine below before using this conversion ...
98 CALL convertXYZtoXRPhi(gr0)
99
100 ! Allocate array for output of calculation:
101 ! Variable 1 :: du/dz
102 ! Variable 2 :: epsilon_ijk (s_ijk)*omega_k)
103 ALLOCATE(dgfun(ng))
104 DO n=1,ng
105   dgfun(n)%ni=gfun(n)%ni
106   dgfun(n)%nj=gfun(n)%nj
107   dgfun(n)%nk=gfun(n)%nk
108   dgfun(n)%nf=2
109   ALLOCATE(dgfun(n)%f(dgfun(n)%ni,dgfun(n)%nj,dgfun(n)%nk,dgfun(n)%nf))
110 ENDDO
111
112 DO n=1,ng
113   WRITE(*,'(A,I5)') "Computing Zone ",n
114   DO i=1,gr0(n)%ni
115     DO j=1,gr0(n)%nj
116       DO k=1,gr0(n)%nk
117         ! Find indices for my neighbors -> nID
118         CALL setNeighbors(n,i,j,k,gr0(n)%ni,gr0(n)%nj,gr0(n)%nk,nID)
119
120         ! Ask for derivative of variable in p coordinate direction ...
121         ! In the current dataset the streamwise velocity is variable 2 ...
122         ! partialOne(dataSet,varID,gridData,i,j,k,neighborIDs,derivDirection)
123         dgfun(n)%f(i,j,k,1) = partialOne(gfun,2,gr0,i,j,k,nID,3)
124         ! first partial of variable 2 in gfun w.r.t. direction 3 in gr0 ...
125         ! this is du / dz
126

```

/Users/nathanmurray/ResearchRemote/ResearchAnalysis/computingDerivatives_1_001.f90 Page 3 of 9
 Saved: 1/31/13 1:37:00 PM Printed For: Nathan Murray

```

127      ! Construct the omega dot strain-rate tensor product similar to
128      ! Seiner's rational approach ... however, this is NOT the Seiner
129      ! term of interest ... here I'm computing the TOTAL not the
130      ! FLUCTUATING quantity that is really of interest.
131      dgfun(n)%f(i,j,k,2) = 0.0
132      ! Loop over (ll,mm,nn) = 1 -> 3 to perform tensor product
133      DO ll=1,3; DO mm=1,3; DO nn=1,3
134          IF ( pt(ll,mm,nn) .EQ. 0.0 ) THEN
135              ! pt == 0.0 is the permutation tensor = 0 so we can cycle
136              ! to the next iteration of the DO loop ...
137              CYCLE
138          ELSE
139              dgfun(n)%f(i,j,k,2) = dgfun(n)%f(i,j,k,2) + &
140              pt(ll,mm,nn) * 0.5 * omega(gfun,uvwID,gr0,i,j,k,nID,nn) * &
141              ( partialOne(gfun,uvwID(ll),gr0,i,j,k,nID,mm) + &
142                partialOne(gfun,uvwID(mm),gr0,i,j,k,nID,ll) )
143              ! The above sums up all the terms of
144              ! epsilon_lmn * s_lm * omega_n
145              ! where s_lm is computed as
146              ! 0.5 * ( du_1/dx_m + du_m/dx_1 )
147          ENDIF
148      ENDDO; ENDDO; ENDDO
149
150      ENDDO
151      ENDDO
152      ENDDO
153      ENDDO
154
155      WRITE(*,'(A)') "Writing Output"
156
157      WRITE(fn,'(A)') "DerivativesOutput.bin"
158      OPEN(UNIT=101,FILE=TRIM(fn),FORM='unformatted',STATUS='replace',ACTION='write')
159      WRITE(101) ng
160      WRITE(101) (dgfun(n)%ni,dgfun(n)%nj,dgfun(n)%nk,dgfun(n)%nf,n=1,ng)
161      DO n=1,ng
162          WRITE(101) dgfun(n)%f
163      ENDDO
164      CLOSE(101)
165
166      WRITE(*,'(A)') "Done"
167
168      CONTAINS
169
170      SUBROUTINE convertXYZtoXRPhi(grid)
171      ! convertXYZtoXRPhi assumes 'grid' contains a cartesian grid with variables
172      ! 'x,y,z' and converts to a cylindrical grid with 'x,r,phi'
173      !----- Discussion -----
174      ! This conversion assumes a right-handed coordinate system where 'x' is
175      ! the axis of the cylindrical coordinate system. The calculation of 'r'
176      ! is then straightforward as (y^2 + z^2)^0.5. However, the determination
177      ! of the azimuthal angle phi requires care. The FORTRAN intrinsic ATAN2 is
178      ! aware of this issue and takes into account what quadrant (y,z) is in
179      ! when returning the angle. However, the result is restricted to the
180      ! range -pi/2 -> +pi/2 where the angle is measured as the counter-clockwise
181      ! rotation from the positive 'y' axis. NOTICE -- If this conversion is
182      ! performed prior to computing derivatives there WILL BE ambiguity at the
183      ! negative 'y' axis where a "jump" will appear from +pi/2 to -pi/2 between
184      ! neighboring grid points.
185      !----- Concerning the Present Situation -----
186      ! I have created this problem in some degree by generating 'neighbor' rules
187      ! that allow the azimuthal grid index to wrap ... one way of avoiding the
188      ! above problem is to compute only forward or backward derivatives at the
189      ! negative 'y' axis ... in essence setting the negative 'y' axis as an

```

/Users/nathanmurray/ResearchRemote/Research/FDanalysis/computingDerivatives_1_001.f90 Page 4 of 9
 Saved: 1/31/13 1:37:00 PM Printed For: Nathan Murray

```

190 ! actual boundary. Another possible solution would be the assignment of
191 ! a separate type of boundary ... a periodic boundary at the negative 'y'
192 ! axis ... but this would require a separate set of conditions to handle
193 ! central-differences across the periodic boundary ... for now, I'm not going
194 ! to implement either of these solutions but only mention them here for
195 ! reference.
196 TYPE(func), DIMENSION(:), INTENT(INOUT) :: grid
197 INTEGER :: i,j,k
198 REAL :: r,phi,y,z
199
200 DO n=1,SIZE(grid)
201   DO i=1,grid(n)%ni
202     DO j=1,grid(n)%nj
203       DO k=1,grid(n)%nk
204         y = grid(n)%f(i,j,k,2); z = grid(n)%f(i,j,k,3)
205         grid(n)%f(i,j,k,2) = SQRT(y**2.0 + z**2.0)
206         grid(n)%f(i,j,k,3) = ATAN2(z,y)
207       ENDDO
208     ENDDO
209   ENDDO
210 ENDDO
211
212 END SUBROUTINE convertXYZtoXRPhi
213
214 SUBROUTINE setNeighbors(currentZone,ii,jj,kk,imax,jmax,kmax,neighborID)
215 ! setNeighbors builds the small array 'neighborID' which identifies the grid
216 ! location of all 6 neighbors to the current cell. These are subsequently used
217 ! to compute derivatives as desired. There are some calculations here that are
218 ! strictly dependent on the current data set. The idea was to use this
219 ! subroutine to identify the neighbors so that the computation of derivatives
220 ! could be completely general.
221 INTEGER, INTENT(IN) :: currentZone,ii,jj,kk,imax,jmax,kmax
222 TYPE(neighborIDs), DIMENSION(:,:), INTENT(OUT) :: neighborID
223 ! neighborID [ [i,j,k Direction], [behind,ahead] ]
224
225 ! Initialize all 'isBoundary' logicals to FALSE to ensure they are only
226 ! set to true if necessary.
227 neighborID(:, :) %isBoundary = .FALSE.
228
229 !-----
230 ! Set neighbors in the i-Direction.
231 !-----
232 ! The 'i' direction is the axial direction and is continuous
233 ! without any zonal boundaries in the current data set. All
234 ! I have to check for is the grid space boundaries.
235 ! I can do this using the MIN and MAX commands without
236 ! requiring IF THEN blocks.
237 neighborID(1,1:2)%zID = currentZone
238 neighborID(1,1)%ii = MAX(ii-1,1)
239 neighborID(1,2)%ii = MIN(ii+1,imax)
240 neighborID(1,1:2)%jj = jj
241 neighborID(1,1:2)%kk = kk
242 IF ( ii .EQ. 1 ) THEN
243   neighborID(1,1)%isBoundary = .TRUE.
244 ELSE IF ( ii .EQ. imax ) THEN
245   neighborID(1,2)%isBoundary = .TRUE.
246 ELSE
247   neighborID(1,2)%isBoundary = .FALSE.
248 ENDIF
249
250 ! In the 'j' and 'k' directions, all my neighbors have the
251 ! same ii index, so I can set that here ...
252 neighborID(2:3,1:2)%ii = ii

```

/Users/nathanmurray/ResearchRemote/ResearchAnalysis/computingDerivatives_1_001.f90 Page 5 of 9
 Saved: 1/31/13 1:37:00 PM Printed For: Nathan Murray

```

253
254   IF ( currentZone .EQ. 1 ) THEN
255     !-----
256     ! Set Neighbors in Zone 1 ... the outer zone ...
257     ! The 'j' direction is the radial direction ...
258     ! The 'k' direction is the azimuthal direction ...
259     !-----
260     ! The 'ahead' j-neighbor is always in the current zone
261     neighborID(2,2)%zID = currentZone
262     neighborID(2,2)%kk = kk
263     ! ... but may be on the outer boundary
264     neighborID(2,2)%jj = MIN(jj+1,jmax)
265     IF ( jj .EQ. jmax ) neighborID(2,2)%isBoundary = .TRUE.
266
267     ! If I'm not on the inner boundary ...
268     IF ( jj .GT. 1 ) THEN
269       ! the 'behind' neighbor is straightforward
270       neighborID(2,1)%zID = currentZone
271       neighborID(2,1)%jj = jj-1
272       neighborID(2,1)%kk = kk
273     ELSE
274       ! The 'behind' neighbor is in zone 2 ... the inner zone
275       neighborID(2,1)%zID = 2
276       ! The specific neighbor now depends on which sector I
277       ! am in. A simple INT() function can indicate the sector
278       ! given that there are 30 elements in each of the 4 sectors.
279       IF ( INT((kk-1)/30)+1 .EQ. 1 ) THEN ! sector 1
280         neighborID(2,1)%jj = 1
281         neighborID(2,1)%kk = 30 - kk + 1
282       ELSE IF ( INT((kk-1)/30)+1 .EQ. 2 ) THEN ! sector 2
283         neighborID(2,1)%jj = kk - 30
284         neighborID(2,1)%kk = 1
285       ELSE IF ( INT((kk-1)/30)+1 .EQ. 3 ) THEN ! sector 3
286         neighborID(2,1)%jj = 30
287         neighborID(2,1)%kk = kk - 60
288       ELSE IF ( INT((kk-1)/30)+1 .EQ. 4 ) THEN ! sector 4
289         neighborID(2,1)%jj = 30 - (kk - 90) + 1
290         neighborID(2,1)%kk = 30
291       ENDIF
292     ENDIF
293
294     ! Set the neighbors in the 'k' direction ...
295     ! Both 'ahead' and 'behind' neighbors are in the same zone ...
296     neighborID(3,1:2)%zID = currentZone
297     neighborID(3,1:2)%jj = jj
298     ! ... but there is a wrap-around in the azimuthal direction
299     neighborID(3,1)%kk = kk-1
300     neighborID(3,2)%kk = kk+1
301     IF ( kk .EQ. 1 ) THEN
302       neighborID(3,1)%kk = kmax ! 'behind' neighbor has to wrap
303     ELSE IF ( kk .EQ. kmax ) THEN
304       neighborID(3,2)%kk = 1 ! 'ahead' neighbor has to wrap
305     ENDIF
306   ELSE IF ( currentZone .EQ. 2 ) THEN
307     !-----
308     ! Set Neighbors in Zone 2 ... the inner zone ...
309     ! 'j' and 'k' represent a curvilinear coordinate system
310     !-----
311     ! In zone 2 I have to be careful with the boundaries
312     ! Set the j-Direction neighbors first
313     IF ( jj .EQ. 1 ) THEN
314       neighborID(2,1)%zID = 1 ! behind neighbor in Zone 1
315       neighborID(2,1)%jj = 1 ! All Zone 1 neighbors to Zone 2 have j=1

```


/Users/nathanmurray/ResearchRemote/ResearchAnalysis/computingDerivatives_1_001.f90 Page 6 of 9
 Saved: 1/31/13 1:37:00 PM Printed For: Nathan Murray

```

316     neighborID(2,1)%kk = 30 - kk + 1
317     neighborID(2,2)%zID = currentZone
318     neighborID(2,2)%jj = jj+1
319     neighborID(2,2)%kk = kk
320   ELSE IF ( jj .EQ. jmax ) THEN
321     neighborID(2,1)%zID = currentZone
322     neighborID(2,1)%jj = jj-1
323     neighborID(2,1)%kk = kk
324     neighborID(2,2)%zID = 1 ! ahead neighbor in Zone 1
325     neighborID(2,2)%jj = 1 ! All Zone 1 neighbors to Zone 2 have j=1
326     neighborID(2,2)%kk = kk + 60
327   ELSE ! I'm not on a boundary and the neighbors are straightforward
328     neighborID(2,1:2)%zID = currentZone
329     neighborID(2,1 )%jj = jj-1
330     neighborID(2,2 )%jj = jj+1
331     neighborID(2,1:2)%kk = kk
332   ENDIF
333
334   ! Set the k-Direction neighbors
335   IF ( kk .EQ. 1 ) THEN
336     neighborID(3,1)%zID = 1 ! behind neighbor in Zone 1
337     neighborID(3,1)%jj = 1
338     neighborID(3,1)%kk = 30 + jj
339     neighborID(3,2)%zID = currentZone
340     neighborID(3,2)%jj = jj
341     neighborID(3,2)%kk = kk+1
342   ELSE IF ( kk .EQ. kmax ) THEN
343     neighborID(3,1)%zID = currentZone
344     neighborID(3,1)%jj = jj
345     neighborID(3,1)%kk = kk-1
346     neighborID(3,2)%zID = 1 ! ahead neighbor in Zone 1
347     neighborID(3,2)%jj = 1
348     neighborID(3,2)%kk = 90 + 30 - jj + 1
349   ELSE ! I'm not on a boundary and the neighbors are straightforward
350     neighborID(3,1:2)%zID = currentZone
351     neighborID(3,1:2)%jj = jj
352     neighborID(3,1 )%kk = kk-1
353     neighborID(3,2 )%kk = kk+1
354   ENDIF
355 ELSE
356   ENDIF
357
358 END SUBROUTINE setNeighbors
359
360 FUNCTION partialOne(vFunc,nVar,coord,i,j,k,nID,dir) RESULT(varDer)
361 ! partialOne computes the first derivative of variable 'nVar' in 'vFunc'
362 ! at grid location (i,j,k) in the 'dir' coordinate direction
363 ! using the neighbors defined in nID. The coordinate direction
364 ! corresponds to one of the grid axes ... i.e. (x,y,z) or (x,r,phi)
365 IMPLICIT NONE
366 TYPE(func),DIMENSION(:),INTENT(IN) :: vFunc
367 TYPE(func),DIMENSION(:),INTENT(IN) :: coord
368 INTEGER,INTENT(IN) :: i,j,k,dir,nVar
369 TYPE(neighborIDs),DIMENSION(:,:),INTENT(IN) :: nID
370 REAL :: varDer,d1,d2,d3
371
372 REAL,DIMENSION(3,3) :: gMets
373
374 gMets = setMetrics(coord,i,j,k,nID)
375
376 ! Differencing of the function variable on the computational space
377 d1 = dol(vFunc,nVar,nID,1)
378 d2 = dol(vFunc,nVar,nID,2)

```

/Users/nathanmurray/ResearchRemote/ResearchAnalysis/computingDerivatives_1_001.f90 Page 7 of 9
 Saved: 1/31/13 1:37:00 PM Printed For: Nathan Murray

```

379      d3 = dol(vFunc,nVar,nID,3)
380
381      varDer = gMets(1,dir)*d1 + gMets(2,dir)*d2 + gMets(3,dir)*d3
382
383  END FUNCTION partialOne
384
385  FUNCTION setMetrics(coord,ii,jj,kk,nID) RESULT(gridMet)
386  ! setMetrics returns the 3x3 matrix of grid metrics necessary for
387  ! computing derivatives.
388  IMPLICIT NONE
389  TYPE(func),DIMENSION(:),INTENT(IN) :: coord
390  TYPE(neighborIDs),DIMENSION(:,:),INTENT(IN) :: nID
391  INTEGER,INTENT(IN) :: ii,jj,kk
392  INTEGER :: i,j
393  REAL,DIMENSION(3,3) :: gridMet
394  REAL,DIMENSION(3,3) :: jac
395  REAL :: detJac
396
397  ! differencing physical space (x,y,z) W.R.T. grid directions i,j,k
398  ! i.e. dx/dxi is the difference of "x" in the "xi, or 1" coordinate
399  ! direction.
400  DO i=1,3 ! For each grid index direction i,j,k
401      DO j=1,3 ! For each coordinate direction i.e. x,y,z
402          ! Differencing of coordinate 'j' in the 'i' direction
403          jac(j,i) = dol(coord,j,nID,i)
404      ENDDO
405  ENDDO
406
407  !The jacobian^-1 of transformation -----
408  detJac = 1.0d0/( jac(1,1)*(jac(2,2)*jac(3,3)-jac(2,3)*jac(3,2)) - &
409                jac(1,2)*(jac(2,1)*jac(3,3)-jac(2,3)*jac(3,1)) + &
410                jac(1,3)*(jac(2,1)*jac(3,2)-jac(2,2)*jac(3,1)) )
411
412  ! These are the grid metrics -----
413  ! (1,1) = d_xi/d_x ... (2,3) = d_eta/d_z ... etc.
414  gridMet(1,1) = detJac * (jac(2,2)*jac(3,3) - jac(2,3)*jac(3,2))
415  gridMet(1,2) = -detJac * (jac(1,2)*jac(3,3) - jac(1,3)*jac(3,2))
416  gridMet(1,3) = detJac * (jac(1,2)*jac(2,3) - jac(1,3)*jac(2,2))
417  gridMet(2,1) = -detJac * (jac(2,1)*jac(3,3) - jac(2,3)*jac(3,1))
418  gridMet(2,2) = detJac * (jac(1,1)*jac(3,3) - jac(1,3)*jac(3,1))
419  gridMet(2,3) = -detJac * (jac(1,1)*jac(2,3) - jac(1,3)*jac(2,1))
420  gridMet(3,1) = detJac * (jac(2,1)*jac(3,2) - jac(2,2)*jac(3,1))
421  gridMet(3,2) = -detJac * (jac(1,1)*jac(3,2) - jac(1,2)*jac(3,1))
422  gridMet(3,3) = detJac * (jac(1,1)*jac(2,2) - jac(1,2)*jac(2,1))
423
424  END FUNCTION setMetrics
425
426  FUNCTION dol(vfunc,nVar,nbID,dir) RESULT(der)
427  ! dol computes the difference related to a first derivative
428  ! gives central difference for interior nodes ...
429  ! gives forward or backward difference for boundary nodes ...
430  ! difference is used.
431  IMPLICIT NONE
432  TYPE(func),DIMENSION(:),INTENT(IN) :: vfunc
433  TYPE(neighborIDs),DIMENSION(:,:),INTENT(IN) :: nbID
434  INTEGER,INTENT(IN) :: dir,nVar
435  REAL :: delta,der
436
437  ! If either neighbor in the differencing direction is a boundary ...
438  IF ( nbID(dir,1)%isBoundary .OR. nbID(dir,2)%isBoundary ) THEN
439      delta = 1.0 ! set delta to 1.0 (forward or backward difference)
440  ELSE
441      delta = 2.0 ! set delta to 2.0 (central difference)

```

/Users/nathanmurray/ResearchRemote/Research/FDanalysis/computingDerivatives_1_001.f90 Page 8 of 9
 Saved: 1/31/13 1:37:00 PM Printed For: Nathan Murray

```

442   ENDIF
443   ! The computational space has a delta of "1.0" grid unit per index.
444   ! This delta assumption cancels out when performing the differencing
445   ! on the physical variables so it can be anything.
446
447   ! This gives the (ii,jj,kk) ind
448   der = ( vfunc(nbID(dir,2)%zID)%f(nbID(dir,2)%ii,&
449     nbID(dir,2)%jj,nbID(dir,2)%kk,nVar) - &
450     vfunc(nbID(dir,1)%zID)%f(nbID(dir,1)%ii,&
451     nbID(dir,1)%jj,nbID(dir,1)%kk,nVar) ) / delta
452
453   END FUNCTION
454
455   FUNCTION kd(i,j) RESULT(delta) ! Kronecker delta
456     INTEGER, INTENT(IN) :: i,j
457     REAL :: delta
458
459     IF (i == j) THEN
460       delta = 1.0d0
461     ELSE
462       delta = 0.0d0
463     END IF
464
465   END FUNCTION kd
466
467   FUNCTION pt(i,j,k) RESULT(epsilon) ! permutation tensor
468     INTEGER, INTENT(IN) :: i,j,k
469     REAL :: epsilon
470
471     IF ((i == 1 .AND. j == 2 .AND. k == 3) .OR. &
472       (i == 2 .AND. j == 3 .AND. k == 1) .OR. &
473       (i == 3 .AND. j == 1 .AND. k == 2)) THEN
474       epsilon = 1.0d0
475     ELSE IF ((i == 1 .AND. j == 3 .AND. k == 2) .OR. &
476       (i == 2 .AND. j == 1 .AND. k == 3) .OR. &
477       (i == 3 .AND. j == 2 .AND. k == 1)) THEN
478       epsilon = -1.0d0
479     ELSE
480       epsilon = 0.0d0
481     END IF
482
483   END FUNCTION pt
484
485   FUNCTION omega(vFunc,uvwID,coord,i,j,k,nID,dir)
486     ! omega computes the vorticity in the 'dir' coordinate direction.
487     ! 'uvwID' is a 1x3 array indicating which variables are the velocity
488     ! components in the x,y,z directions. In the current data set this
489     ! should be set to uvwID = (/2,3,4/)
490     IMPLICIT NONE
491     TYPE(func), DIMENSION(:), INTENT(IN) :: vFunc
492     TYPE(func), DIMENSION(:), INTENT(IN) :: coord
493     INTEGER, INTENT(IN) :: i,j,k,dir
494     INTEGER, DIMENSION(:), INTENT(IN) :: uvwID
495     TYPE(neighborIDs), DIMENSION(:, :), INTENT(IN) :: nID
496     INTEGER :: m,n
497     REAL :: omega
498
499     omega = 0.0d0
500     DO m=1,3; DO n=1,3
501       IF ( pt(dir,m,n) .EQ. 0.0 ) THEN
502         CYCLE
503       ELSE
504         omega = omega + &

```

/Users/nathanmurray/ResearchRemote/ResearchAnalysis/computingDerivatives_1_001.f90 Page 9 of 9
Saved: 1/31/13 1:37:00 PM Printed For: Nathan Murray

```
505      pt(dir,m,n)*partialOne(vFunc,uvwID(n),coord,i,j,k,nID,m)
506      ENDIF
507      ENDDO; ENDDO
508
509      END FUNCTION omega
510
511      END PROGRAM computingDerivatives
```


Appendix B: Baars & Tinney "Scaling Model for Nonlinear Supersonic Jet Noise."
APS-DFD-D24.8.

Abstract Submitted
for the DFD12 Meeting of
The American Physical Society

Scaling model for nonlinear supersonic jet noise WOUTIJN BAARS, CHARLES TINNEY, The University of Texas at Austin — Numerous endeavors have been undertaken to investigate nonlinear propagation of sound from jet flows in range-restricted environments. However, only weak observations of cumulative nonlinear effects have been made using these laboratory-scale setups, all the while being observed under full-scale conditions. The inconsistency is caused by the lack of rigor in understanding what the appropriate scaling parameters should be for producing measurable cumulative nonlinearities in laboratory-scale environments. A scaling model will be presented that one could use to guide future studies aimed at investigating this unique component of turbulent mixing noise. At first, the important length-scales for cumulative nonlinear waveform distortion – the shock formation distance and the acoustic absorption length – are written in terms of jet exit parameters. Their ratio, expressed as the effective Gol'dberg number, is a measure of the strength of nonlinear distortion relative to that of dissipation. By computing the individual length-scales and this dimensionless ratio for an experiment that is being designed, one can estimate the presence of cumulative nonlinear distortion beforehand.

Woutijn Baars
The University of Texas at Austin

Date submitted: 12 Aug 2012

Electronic form version 1.4

Appendix C: Panickar *et al.* "Localization of Acoustic Sources in Shock-Containing Jet Flows Using Phased Array Measurements." AIAA Paper 2013-0613.

51st AIAA Aerospace Sciences Meeting including the New Horizons Forum and Aerospace Exposition
07 - 10 January 2013, Grapevine (Dallas/Ft. Worth Region), Texas

AIAA 2013-0613

Localization of Acoustic Sources in Shock-Containing Jet Flows Using Phased Array Measurements

Praveen Panickar,* James P. Erwin† and Neeraj Sinha‡

Combustion Research and Flow Technology, Inc. (CRAFT Tech), Pipersville, PA-18947, USA

Nathan E. Murray§ and Gregory Lyons¶

National Center for Physical Acoustics, The University of Mississippi, University, MS-38677, USA

In this paper, we shall examine the feasibility of using time-resolved hybrid RANS-LES (HIRLES) simulation data to perform noise source localization studies on a hot jet from a conic nozzle operating at pressure matched conditions. The source localization will be performed using a traditional delay-and-sum beamforming technique. This technique requires time-resolved data on a phased array of microphones located in the acoustic farfield of the jet; this data will be obtained by coupling the HIRLES simulation with a Ffowcs Williams and Hawkings equation noise prediction code. Using insights gained from experimental beamforming, we shall show that beamforming using CFD data is a feasible, and potentially less expensive and time-saving, alternative to constructing complicated phased array systems for performing these calculations on experimental data.

I. Background and Motivation

Noise from supersonic jets falls primarily into two categories, either turbulent mixing noise or shock noise. Of these two, turbulent mixing noise is comprised of two sources, both of which are broadband in nature: (a) the eddy Mach wave radiation which propagates downstream relative to the jet flow direction, and (b) fine scale turbulence which is omni-directional. On the other hand, shock noise can be either narrowband (also called jet screech) or broadband (called broadband shock associated noise, or BSAN), and propagates towards the sideline or upstream direction relative to the jet flow. Shock noise most commonly occurs when a convergent-divergent nozzle is operated at off-design conditions. However, jets exhausting from military nozzles typically contain shocks even when operated at design conditions; this is primarily because the internal contour of these nozzles are not shaped in order to ensure a smooth expansion of the gas.

Jet noise contributes significantly to noise-induced hearing loss, structural degradation of airframes, and restrictions to maintenance, testing, and training schedules due to noise pollution of communities surrounding military installations. To this end, it is imperative to gain a better understanding of jet noise generation mechanisms in a turbulent flow. Such an understanding is essential if one is to construct predictive models for jet noise. One approach that has been considered is the beamforming technique using a phased array of microphones.¹ This technique has been shown to provide an estimate of the distribution of noise sources in a

*Research Scientist, Senior AIAA Member.

†Research Scientist, AIAA Member.

‡Technical Director, AIAA Associate Fellow.

§Research Scientist II and Research Assistant Professor of Mechanical Engineering, Senior AIAA Member.

¶Graduate Research Assistant, AIAA Member.

flow. Investigations on the use of phased arrays in aeroacoustics in general, and jet noise in particular, were conducted by many researchers including Brooks and his coworkers²⁻⁴ at NASA Langley, Bridges and his coworkers^{5,6} at NASA Glenn, Papamoschou, Morris and McLaughlin⁷ to name a few. Recently Dougherty⁸ developed a new generalized inverse beamforming method for jet noise and demonstrated its effectiveness in mapping coherent sources and extrapolating directivity patterns using a 2D phased array system.

All the reports referenced in the previous paragraph are based on experimental studies. Working with simulated data removes many of the encumbrances that are present while working in an experimental facility. For instance, in an experimental facility, one is restricted by the size and placement of microphones that comprise the phased array system. It is not possible to use a phased array system to interrogate a cross plane of the jet unless one resorts to a cage array, in which case care has to be taken that the microphones are not damaged by the flow; this can make the aperture of the phased array larger than what would be practically required depending on the frequency of interest. Additionally, moving the system and setting it up at a different location takes a long time since each move requires a recalibration. These difficulties are not present when simulated data is used for phased array calculations; the phased array can be located anywhere in the flowfield. Other practical limitations present in experimental testing, such as the number of microphones available for use, are also not present when looking at simulated data. The major limitation when using simulated data is the cost involved with generating time resolved data; however, this difficulty is gradually being alleviated as supercomputing clusters, with ever-increasing processor counts, become available, and by using these clusters in parallel to provide time resolved data at a reasonably fast rate.

Given all of the limitations discussed previously with experimental phased arrays, it should be noted here that the phased array calculations using simulated data is not meant to replace, or eliminate, the need for these experiments. Rather, the intent is to use the simulated data to carefully guide the experiments and suggest optimized array configurations that lead to more accurate source localization. The simulated phased array data can be used in two specific ways. First, by using a large amount of numerical microphones that can be located anywhere in the acoustic field, beamforming calculations can be used in order to determine source characteristics (frequency and location) that would be difficult to predict given the limited number of microphones available to the experimentalist. Secondly, once these characteristics are known, a virtually limitless amount of array configurations can be tested using only the number of microphones available for a given experiment in a test facility. The configurations that best match the ideal solution can be the focus of the experiments for further testing. The goal of this paper is to present this methodology and consider its application to shock-containing jets for initial validation, before expanding out to other aeroacoustics configurations of interest.

II. Configurations and Objectives

The current work involves a combined experimental and computational initiative in order to examine and understand the inner nozzle and near nozzle flow conditions and their impact on jet noise. To this end, we shall examine a nozzle that consists of a straight walled convergent-divergent section, which we shall refer to as the conic nozzle; the interested reader is referred to Murray et al.⁹ for nozzle geometry details. Based on the throat-to-exit area ratio, the conic nozzle has a prescribed "design" operating Mach number of $M_j = 1.74$.

The primary objective of the current work will be to investigate the feasibility of performing phased array calculations on simulated jet data. This feasibility will be gauged by performing beamforming calculations on the conic nozzle with the centerbody operating at its design (or pressure-matched) condition. This primary objective can be broken up into the following sub-objectives:

1. Compare overall and spectral acoustic characteristics of experimental and computational configurations in the farfield in order to ensure agreement between the two.
2. Acquire fluctuating pressure data using a linear phased array, for the conic nozzle configuration with the centerbody operating at pressure matched conditions, in the anechoic jet laboratory at the NCPA in order to determine an acceptable number of ensembles for constructing the cross-spectral matrix.
3. Perform high-fidelity HRLES simulations of this configuration, and obtain adequate time-resolved data on the ADS (as dictated by the results of the previous item).
4. Using FW-H equations, propagate the acoustics on the ADS to microphone locations on the linear array that was used in the experimental measurements.
5. Perform beamforming calculations of the experimental and computational configurations and compare the source localization results provided by both methods.

The experiments and computational measurements will be performed on heated jets with stagnation temperature of 1005 K (1350 °F) unless specified otherwise.

III. Computational Capabilities and Experimental Setup

The computational simulations were performed using CRAFT Tech's CRAFT CFD® LES code^{10,11} which is a structured Navier-Stokes solver that uses an upwind differencing scheme that is fifth order accurate in space and various time integration schemes including a second order implicit alternating direction implicit (ADI) scheme and various explicit Runge-Kutta schemes. The code is highly parallelized using domain decomposition, with linear speed-up parallel performance on several large supercomputers for very large grids.¹² The calculations were performed using a hybrid RANS-LES (HRLES) model.¹³ The primary advantage of using HRLES is the ability to include the internal nozzle in the jet noise simulations. By including the internal nozzle it becomes possible to smoothly transition the subgrid eddy viscosity from within the nozzle boundary layer to the LES. The intent of the HRLES simulations is to more accurately describe the nozzle and LES interface boundary condition instead of dialing in a steady boundary condition from a precursor RANS solution (zonal RANS/LES). The HRLES framework allows for feedback between the RANS and LES regions and can help appropriately capture realistic fluctuations inside of the nozzle given sufficient, and often times restrictive, grid resolution. Currently the eddy viscosity predicted by the HRLES model tends to smooth the initial shear layer and negatively impact the noise levels in the sideline and upstream directions. In the downstream direction, the primary component of noise is due to turbulent mixing and this component is captured with sufficient accuracy by the zonal RANS/LES method. Thus, by using HRLES, one can expect to improve noise predictions in the sideline and upstream directions and show better agreement with experiments. The computational grid for the current initiative contains approximately 7 million cells and extends $60R_j$ (R_j is the nozzle radius) in the axial (X) direction and had a radius of $30R_j$ at its widest extent. Downstream of this, there is a buffer zone that extends a further $30R_j$ in order to damp out unwanted reflections at the LES flow boundaries. Inside of the buffer zone, rapid grid stretching is employed along with a first order upwind scheme.

Many researchers have contributed to the development of the CFD acoustic analogy method for jet noise.¹⁴⁻¹⁷ In this paper we shall make use of the Ffowcs-Williams and Hawkins (FW-H) equation to compute the far-field noise at desired microphone locations. This solution consists of an integration over a surface surrounding the noise generating mechanisms of the flow.^{18,19} In order to perform this integration, flow variables are recorded on this "permeable" acoustic data surface (ADS) with the desired time resolution. Figure 1 shows the HRLES computational domain with the ADS in place. The time step for the CFD

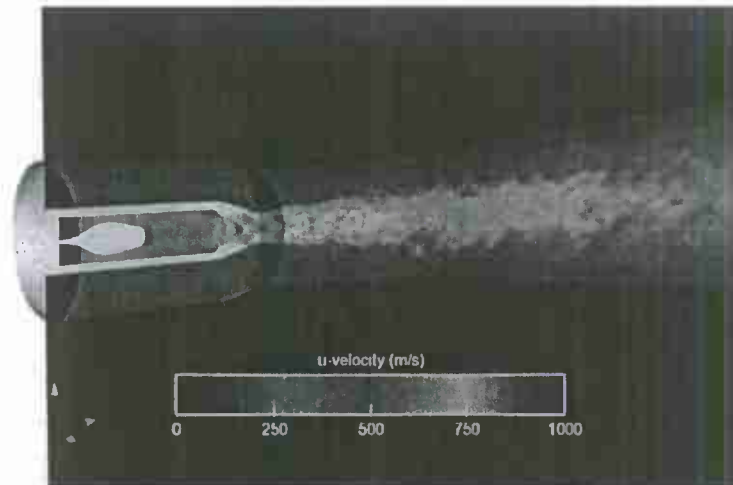


Figure 1. Computational domain with acoustic data surface (ADS), shown shaded, used to predict farfield noise using the Ffowcs-Williams and Hawkins (FW-H) equations.

simulations in the current effort was selected to be 5.0×10^{-8} seconds. For farfield noise and beamforming calculations a sample rate of 200 kHz was determined to be satisfactory, and acoustic variables were recorded on the ADS every 100 LES timesteps. The LES/FW-H codes described here have been extensively used for the prediction of jet noise for a wide variety of subsonic and supersonic jets in both free and impinging jet configurations.²⁰⁻²²

In order to supplement the CFD computations, some experimental phased array tests were conducted in the Anechoic Jet Laboratory (AJL) at the University of Mississippi National Center for Physical Acoustics; facility details can be found in Murray et al.⁹ This phased array system consists of 32 exponentially spaced Kulite pressure transducers (type XT-140, dynamic range = 0-100 psia), mounted on a stainless steel rod. This array was positioned 60.96 cm (24 inches) below the nozzle exit and offset 7.64 cm (2.94 inches) in the axial direction; the downstream end of the rod was inclined at an angle of 15° to the nozzle axis. Figure 2 shows an image of the experimental setup with the nozzle and the pressure transducers mounted in the rod. Digitized fluctuating pressure data from the array was recorded and stored on a National Instruments PXIe (PCI eXtensions for Instrumentation-express) system. The PXIe system has four PXIe-4331 cards (8 channels, 24 bits of resolution, 102.4 kHz maximum sample rate). Each acquisition recorded 1048576 samples per channel at 100 kHz. For a given configuration, at least 10 such acquisitions of data were recorded. Spectral data were calculated by dividing the data in a given run into blocks of 8192 points each; this yielded a frequency resolution of 12.21 Hz. Depending on the number of files used to do the spectral calculations, the number of ensembles that could be averaged for the cross spectral matrix ranged from 1 (only part of one file used) to 1280 (all ten files used).

IV. Results and Discussion

Figure 3 shows the LES time-averaged streamwise velocity component, \bar{U} , of the conic nozzle operating at pressure matched conditions. The sharp throat and the conic diverging section (as opposed to a smooth throat and divergent section that would be produced using the method of characteristics) results in two

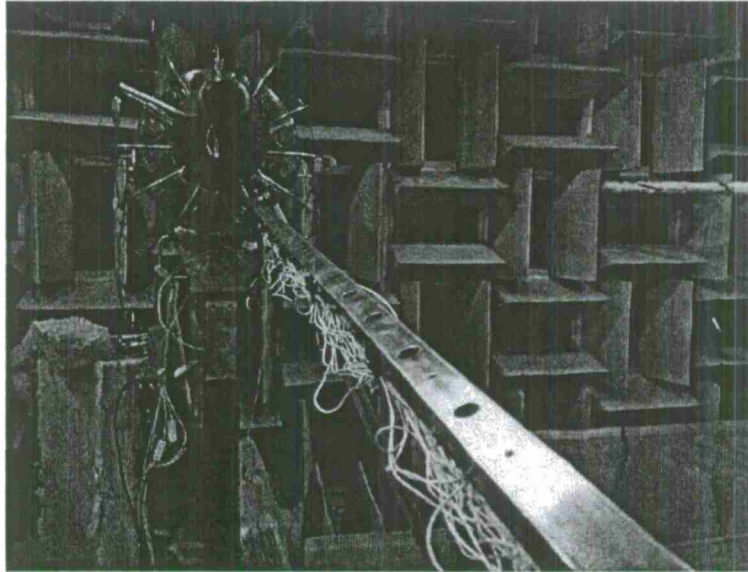


Figure 2. Experimental phased array setup.

separate shock-trains; the first originating at the sharp throat, and the second originating at the nozzle exit. Both shock-trains propagate downstream along the jet column as seen in the figure. In addition to the shock-train, one can also see the slip line along the jet axis where the oblique shock-cells coalesce. Figure 4 shows



Figure 3. Mean streamwise velocity contour of the conic nozzle with upstream centerbody operating at pressure matched conditions.

the normalized (using the jet exit velocity) streamwise velocity along the jet axis. This figure clearly shows the oscillations in the mean velocity, which are a result of the jet undergoing rapid successive expansions and contractions, which shows up in the flow visualization as shock-cell structures.

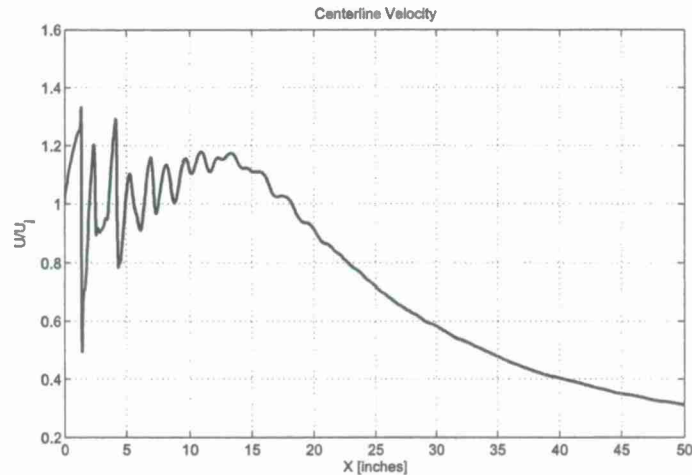


Figure 4. Normalized mean streamwise velocity along the centerline of the jet.

IV.A. Comparison of Farfield Acoustic Characteristics

Prior to performing phased array calculations on the simulated jet data, it is important to compare the simulation and experiments in order to ensure agreement between the two. In the current paper, this agreement will be verified by comparing the farfield acoustic data measured using the arc array of microphones in the AJL to the acoustic levels at the same microphone locations predicted using LES/FW-H methodology. Figure 5 shows a comparison of the overall sound pressure levels (OASPL) between the experimental data and LES/FW-H calculations at the various azimuthal location which are measured with reference to the upstream location. It can be seen that the experiments and simulations agree to within ± 2 dB over most of the measurement angles. The peak level and directivity agrees well with the experimental measurements, including the OASPL directivity at upstream angles, which is a characteristic of shock-containing jets. The agreement worsens at the downstream angles, but this can be attributed to the coarsening of the HRLES grid at the downstream locations and the finite length of the ADS (extending only to $60R_j$).

Figure 6 shows a comparison of the noise spectra at three different farfield microphone locations: 135° (turbulent mixing noise direction), 90° (sideline direction), and 60° (shock noise direction). Once again, the agreement between the experimental measurements and simulations are acceptable to within the restrictions imposed by the grid resolution (~ 10 kHz). In the downstream direction, the Mach wave radiation peak agrees very well with the experimental measurements. The over-prediction of low-frequency noise at all angles is due to the finite LES runtime before noise sampling, and the existence of a long-scale acoustic instability that exists between the inflow and outflow of the LES domain. In the sideline and upstream directions, there appears to be a build-up of energy just before the grid cut-off frequency of around 10 kHz. This build-up is potentially due to the over-prediction of eddy-viscosity by the HRLES model, and holding the initial shear layer steady for too far downstream. When the shear layer destabilizes, the grid resolution in this region is fine and therefore leads to the over-prediction of mid-to-high frequency noise just before the cut-off. To improve the sideline and upstream noise predictions, more grid resolution is required. Nevertheless, the coarse grid used in this study yields acceptable noise predictions which will help guide the development of the source localization in the remainder of the paper.

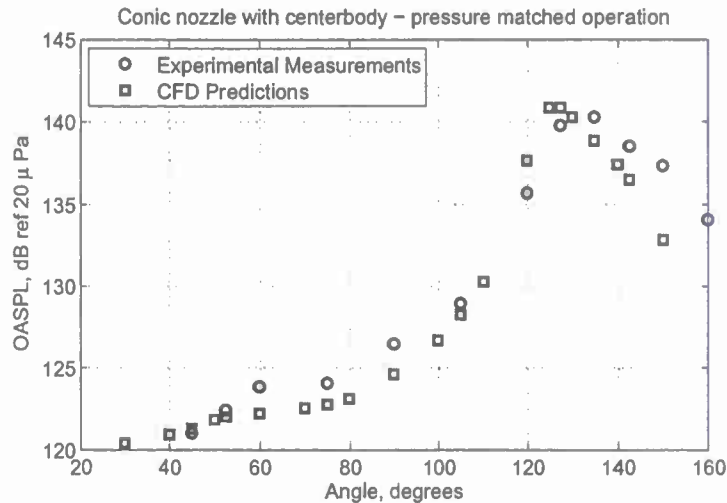


Figure 5. Comparison of the overall sound pressure levels between experimental measurements and FW-H calculations of the simulated jet.

IV.B. Experimental Phased Array Measurements

Prior to performing phased array calculations on the HRLES data, a rudimentary set of experiments were conducted on the conic nozzle configuration with the centerbody using the experimental linear phased array system. The nozzles were operated at cold and heated conditions and fluctuating pressure data was recorded by the linear phased array system. The primary objective of these experiments was to provide guidance to the CFD simulations regarding an acceptable number of ensembles required to generate the cross-spectral matrices used for beamforming calculations. To this end, fluctuating pressure data was acquired by the linear array for the cold nozzle ($T_0 = T_{ambient}$) operated at overexpanded conditions ($M_j = 1.55$). Figures 7 show sample spectra and cross-correlations coefficients calculated for the first six microphones in the array for this cold jet operated at overexpanded conditions. The spectra and cross-correlations shown in figure 7 were calculated using 128 ensemble averages. The spectra clearly show the presence of both shock noise components, i.e., screech and broadband shock associated noise. The screech tone can be clearly seen at approximately 2.6 kHz and the broadband shock noise hump is seen at higher frequencies between 4 and 5 kHz.

In contrast, as shown in figure 8, for heated jets operating at the same overexpanded pressure, screech tones can no longer be clearly discerned. Additionally, it can be seen that the broadband hump has moved to higher frequencies and the correlation levels between the sensors has reduced. This points to a fundamental change in the acoustic sources that we shall examine using phased array calculations.

The data from the phased array system is reduced using the classical delay-and-sum (DAS) beamforming method in the frequency domain. This method assumes that the noise sources are incoherent, point sources. In order to arrive at the beamform map, the following procedure is followed:

- Construct the cross-correlation matrix for each narrowband frequency, $S_f(n, m)$, where n and m are the microphone indices, and f is the narrowband frequency; for the 32 microphones used in this study, this matrix has size 32×32 for each frequency.

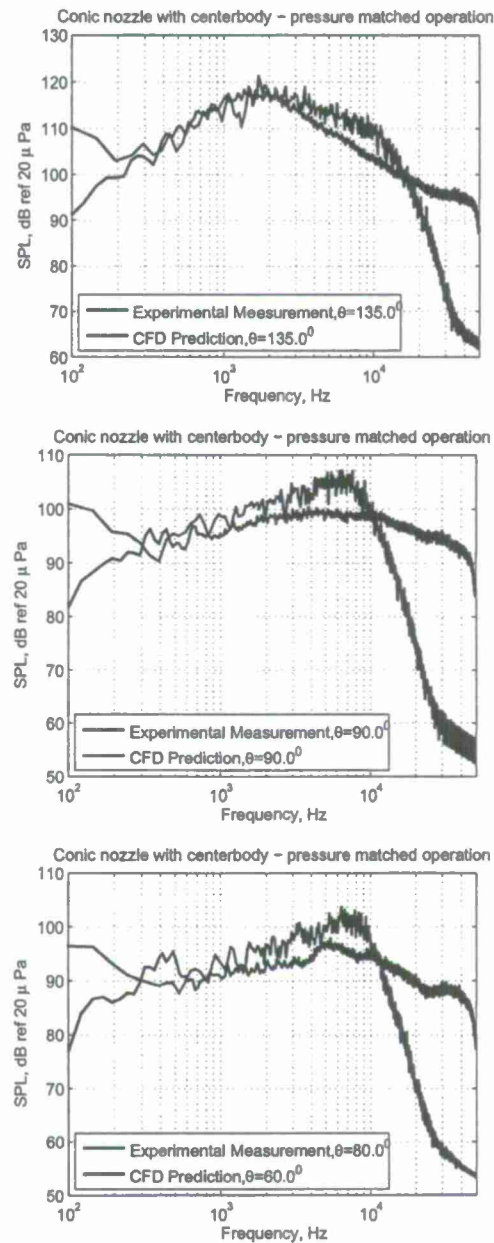
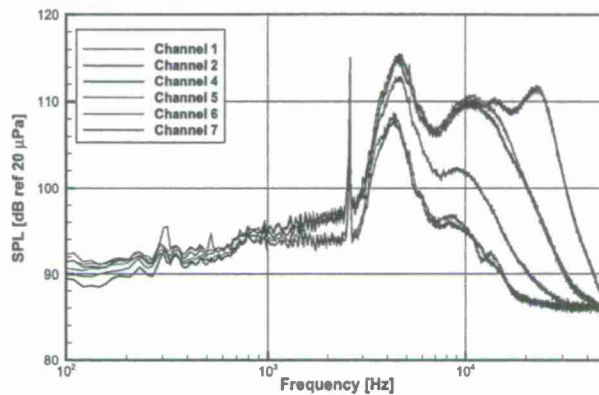
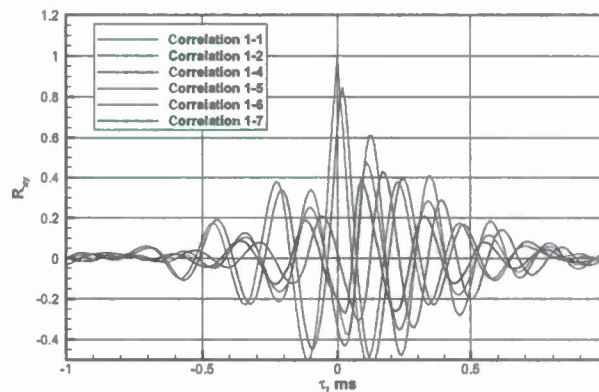


Figure 6. Comparison of the farfield spectral characteristics between experimental measurements and HRLES simulations for the conic nozzle with centerbody operating at pressure matched conditions.



(a) Spectra



(b) Cross correlation coefficients

Figure 7. (a) Spectra and (b) cross correlation coefficients for the first six sensors in the experimental linear phased array. Cold jet, overexpanded operation, $M_j = 1.55$.

- Delete the diagonal element of the cross-correlation matrix at each frequency to give the modified cross-spectral matrix $\tilde{S}_f(m, n)$.
- The beamforming result is calculated using the expression:

$$y_k = w_k^T \tilde{S} w_k, \quad (1)$$

where w_k represents the steering vector for the microphones to a steering point k , and is expressed as:

$$w_{km} = \frac{e^{i \frac{\omega}{c} |\vec{x}_m - \vec{x}_k|}}{|\vec{x}_m - \vec{x}_k|}, \quad (2)$$

where m is the microphone index, $\omega = 2\pi f$ is the circular frequency, c is the speed of sound, and \vec{x} is the vector coordinate location, and $|\vec{x}_m - \vec{x}_k|$ represents the distance between the m^{th} microphone location and the k^{th} scanning plane location.

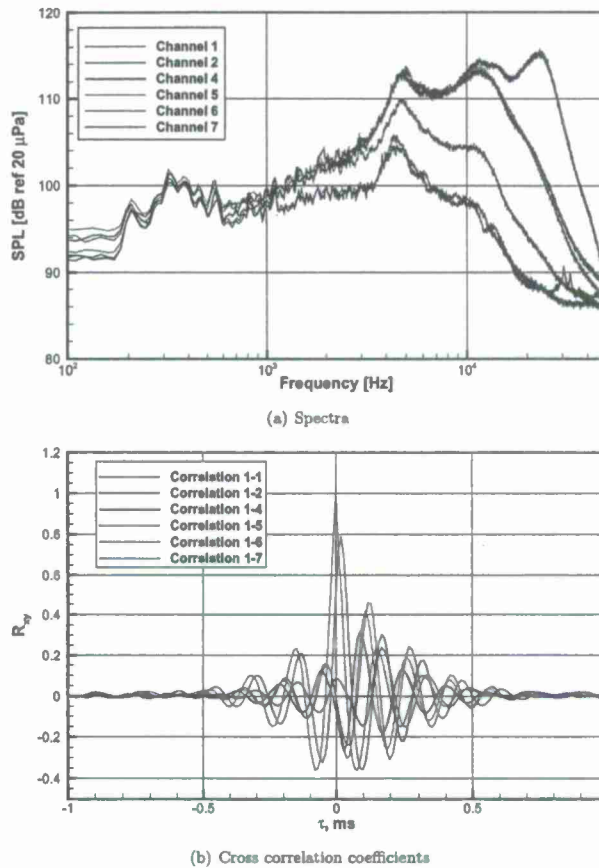


Figure 8. (a) Spectra and (b) cross correlation coefficients for the first six sensors in the experimental linear phased array. Heated jet, $T_j = 1005$ K, pressure-matched operation, $M_j = 1.74$.

Using this method the beamforming result is calculated on a plane of interest, in this case the symmetry plane ($Z = 0$), oriented in the streamwise-vertical (X, Y) direction. Following this, the beamforming results are presented as contour plots corresponding to a specific $1/3^{\text{rd}}$ octave band of interest. This is done by summing the beamforming results at each narrowband frequency comprising the $1/3^{\text{rd}}$ octave band.

For the linear phased array system, the beamforming output is on a scanning line, that extends along the nozzle axis, rather than on a scanning plane. Results are then presented as contour plots on the axial location-frequency, (X, f), plane. For phased array calculations using CFD data, results are presented in the traditional manner, on the (X, Y) plane.

IV.B.1. Determining Optimal Number of Ensembles

When dealing with time-resolved HRLES simulation data, it must be remembered that it is generally not feasible to acquire as much time-resolved data as one can in an experimental study. For instance, the time-resolved experimental data was acquired over a period of ~ 10 seconds; to generate the same amount

of simulation data would take a prohibitive amount of computational time. For this reason, a study was undertaken in order to determine the amount of time-resolved data required for acceptable beamforming results. This study was performed on the cold conic nozzle with the centerbody operating at overexpanded conditions (spectra and cross-correlations shown in figure 7) since this configuration had distinct frequency regimes of interest (screech tones and broadband shock-associated noise) that could be examined for the purpose of this study.

Figures 9(a) and 9(b) show the delay-and-sum beamforming results using 128 ensembles for the cold, overexpanded conic nozzle configuration. This figure clearly shows the broadband shock associated noise, between 4-6 kHz, is localized within 10 inches of the nozzle exit. Additionally, the screech tones at 2.6 kHz, seen better in figure 9(b), extend intermittently (corresponding to the shock-cell intermittency) for almost the entire axial length scanned. Reducing the number of ensembles to 8 reduces the resolution of the beamforming results significantly as shown in figures 9(c) and 9(d); however, one is still able to distinguish the broadband shock-associated noise and screech tone components from the noise floor. Further reduction of the number of ensembles to 4, as shown in figures 9(e) and 9(f), deteriorates the quality of the beamforming results to where it becomes unacceptable. For this reason, it was decided to run the HRLES simulations for enough iterations that would provide 6 ensembles for averaging. In order to run the time-resolved iterations of the HRLES simulations we have used the High Performance Computing (HPC) resources provided by the Department of Defence (DoD). It must be noted that it takes approximately 250,000 CPU hours to run the required number of iterations, which corresponds to approximately 55 days of continuous run time when using 190 CPUs operating in parallel.

IV.C. Phased Array Calculations Using HRLES Data

For the CFD data, the phased array calculations were conducted using two different array designs. Both designs used a 2D array of microphones that were located parallel to the streamwise-vertical, (X, Y) , plane of the jet and offset by a distance of 1.83 m (72 inches) in the Z direction. The first design was similar to the JEDA design discussed in Brooks et al.⁴ and consisted of 41 microphones arranged in 5 concentric circles each containing 8 microphones and an additional microphone at the center. The second design consisted of 45 microphones arranged in 5 logarithmic spiral arms, each containing 9 microphones. Figure 10 shows the microphone locations of both phased array measurement systems. As seen from the figure, both phased array systems have the same effective aperture and size.

As mentioned previously, traditional delay-and-sum beamforming calculations with diagonal removal of the cross spectral matrix were performed, using both phased array systems at various $1/3^{\text{rd}}$ octave band center frequencies. The scanning plane for these calculations was the (X, Y) plane at $Z = 0$. For reference, the nozzle exit plane corresponds to $X = 0$. The results of these calculations are presented as stacks of beamform maps: figure 11 shows the beamform maps for the phased array system consisting of microphones arranged in concentric circles and figure 12 shows the beamform maps for the phased array system with the log-spiral arrangement of microphones. These figures show that the dominant noise source for the jet is located downstream of the nozzle exit at the lower $1/3^{\text{rd}}$ octave band center frequencies. For higher center frequencies, the source regions are located closer to the nozzle exit and are smaller in size compared to those at the lower center frequencies. This result is in broad agreement with experimental work reported in Brooks et al.⁴ and Podboy et al.⁶ Moreover, it is seen that the phased array system using the logarithmic spiral arrangement of microphones does not show striations in the beamforming results similar to what is seen for the phased array system using the concentric circular array of microphones; this is especially evident at higher center frequencies.

Finally, for the purposes of comparison, we present beamforming results from a third array design. This array is similar to the logarithmic spiral array shown in figure 10 and uses the same number of microphones.

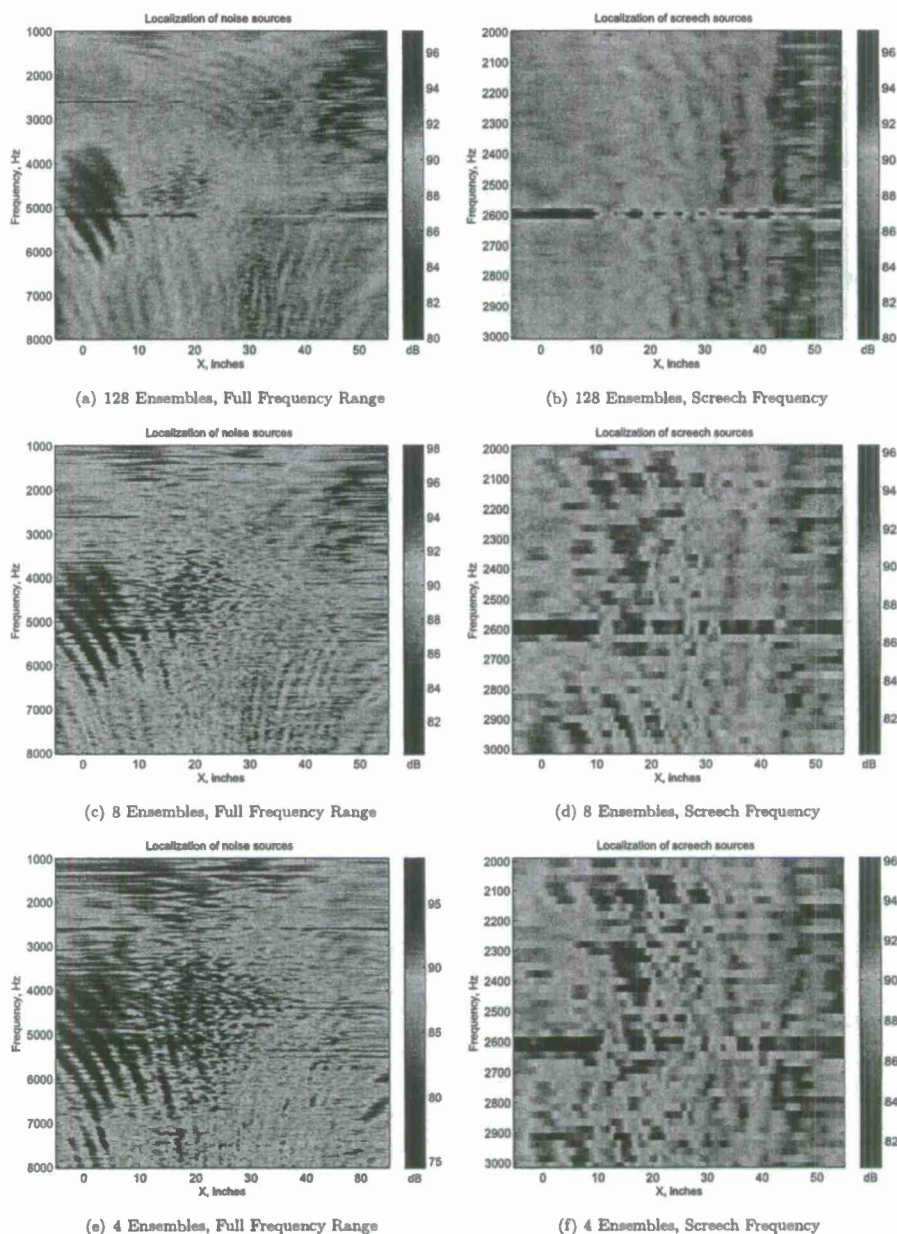


Figure 9. Beamforming results using the linear array of transducers on a cold conic nozzle with the centerbody operating at pressure matched conditions.

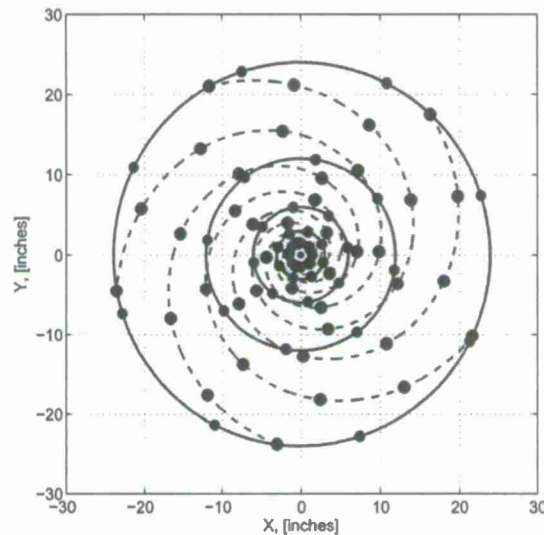


Figure 10. Microphone locations for the phased array systems used in the current study. The microphones on the concentric phased array are shown as filled black circles, and the microphones on the log-spiral array are shown as filled blue circles.

However, this array is ~ 1.5 times larger in diameter; henceforth, we shall refer to the spiral array shown in figure 10 as the small aperture spiral array (SASA) and this new design as the large aperture spiral array (LASA). The beamforming results using the LASA are shown in figure 13. This figure shows the merit of using a phased array of larger aperture for beamforming calculations at the lower center frequencies. It can be seen that for the 3.15 kHz, 5 kHz and 8 kHz center frequencies, the beamforming results using the LASA, figure 13, have better resolution than their counterparts in figure 12 that were calculated using the SASA. However, the disadvantage of using the LASA can be seen from the beamforming results at higher center frequencies where the resolution is diminished when compared to the SASA. This reduction in resolution at higher frequencies can be attributed to spatial aliasing in the LASA, since the microphones are located relatively further apart as compared to the SASA.

Beamforming calculations using simulated data can thus be reliably used to determine acoustic source locations in a jet flow. Due to the quick turnaround time for these calculations, a large number of phased array designs can be tested in a relatively short period of time. This method has the potential for providing guidance for optimal phased array designs and locations, which can then be implemented and verified in an experimental setup.

V. Concluding Remarks

The beamforming results presented in this paper serve to underscore the feasibility of using simulated data in conjunction with a noise prediction code for the purposes of identifying acoustic sources in a flow. It is hoped that these studies can be used to provide insight into acoustic characteristics of various flows of interest to the aeroacoustics community prior to manufacturing and testing expensive models for the laboratory. In this sense, the beamforming calculations using simulated data have been conceptualized in order to provide guidance for optimal array designs for experimental efforts. Simulations of various other jet

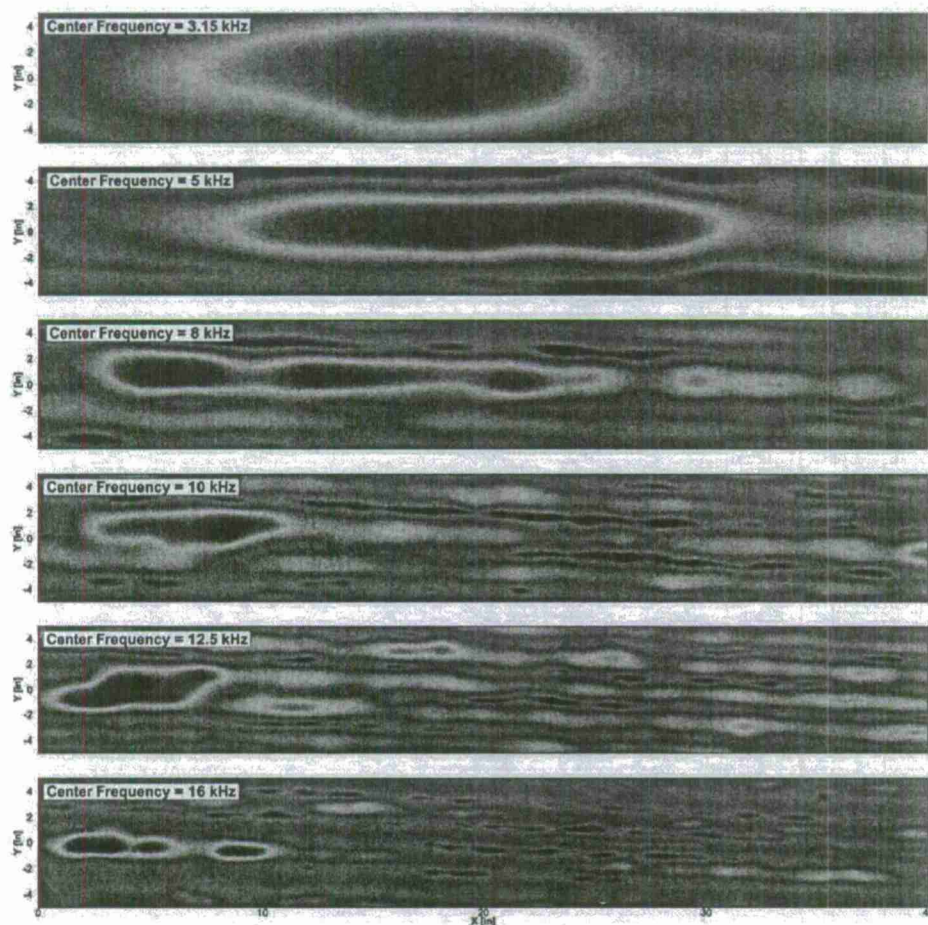


Figure 11. Beamforming maps for the jet from the conic nozzle with the centerbody operated at pressure matched condition using the concentric circular microphone array.

flow configurations of interest, as well as various other aeroacoustic flows, are currently underway. We hope to present results from these studies at future conferences.

VI. Acknowledgements

This work is funded through the Office of Naval Research Jet Noise Reduction program, contract number N00014-11-1-0752, under the direction of Dr. J. Doychak and Dr. B. Henderson. The authors would like to also like to acknowledge the contributions of their co-investigators on the grant, Dr. Charles Tinney (University of Texas at Austin) and Dr. Brian Thurow (Auburn University).

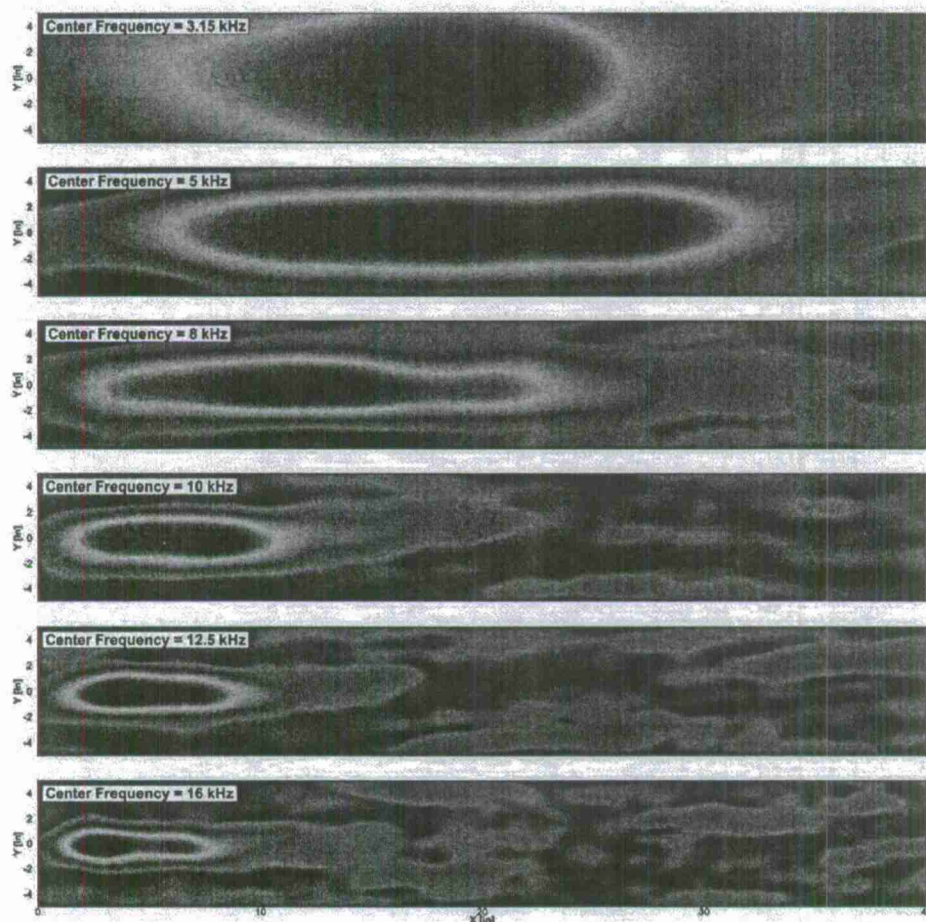


Figure 12. Beamforming maps for the jet from the conic nozzle with the centerbody operated at pressure matched condition using the logarithmic spiral microphone array.

References

- ¹Dougherty, R. P., *Aeroacoustic Measurements*, chap. 2, Experimental Fluid Mechanics, Springer, 2001, pp. 62–97.
- ²Humphreys, W. M., Brooks, T. F., Hunter, W. W., and Meadows, K. R., "Design and use of microphone directional arrays for aeroacoustic measurements," *American Institute of Aeronautics and Astronautics Paper 1998-0471*, 1998.
- ³Brooks, T. F. and Humphreys, W. M., "A deconvolution approach for the mapping of acoustic sources (DAMAS) determined from phased microphone arrays," *Journal of Sound and Vibration*, Vol. 294, 2006, pp. 856–879.
- ⁴Brooks, T. F., Humphreys, W. M., and Plassman, G. E., "DAMAS Processing for a Phased Array Study in the NASA Langley Jet Noise Laboratory," *American Institute of Aeronautics and Astronautics Paper 2010-3780*, 2010.
- ⁵Agboola, F. A. and Bridges, J. E., "Jet Noise Source Localization Using Linear Phased Array," *NASA Technical Memorandum-2004-213041*, 2004.
- ⁶Podboy, G. G., Bridges, J. E., and Henderson, B. S., "Phased Array Noise Source Localization Measurements of an F404 Nozzle Plume at Both Full and Model Scale," *NASA Technical Memorandum-2010-216636*, 2010.

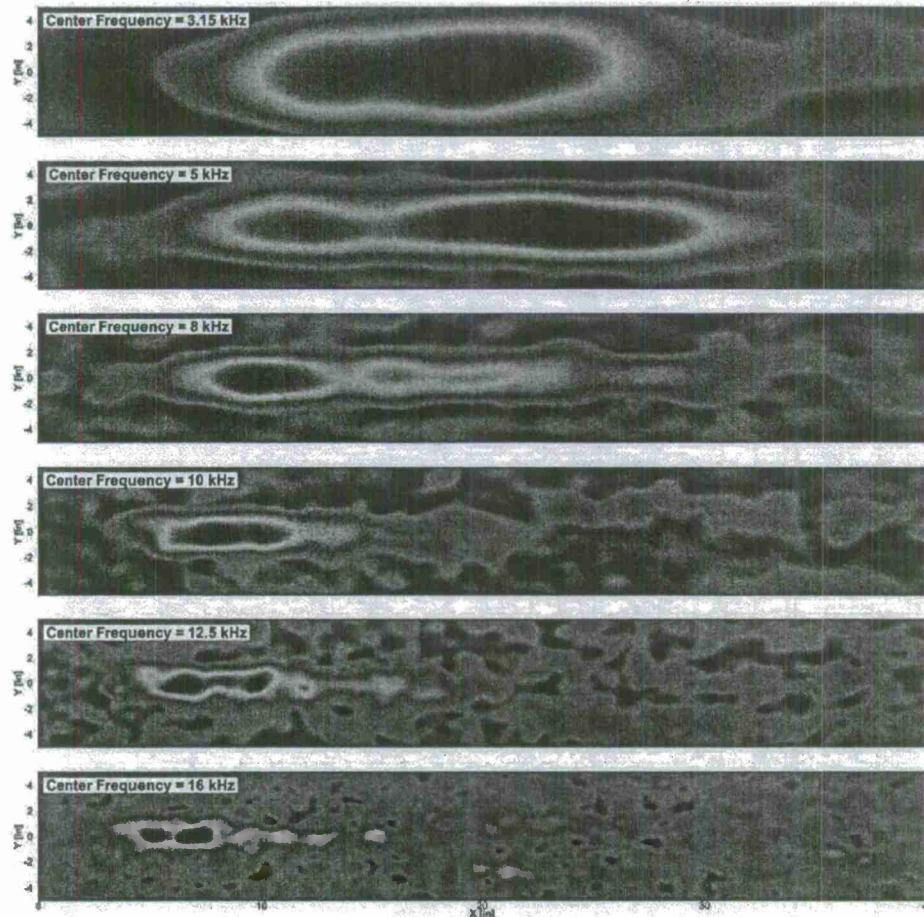


Figure 13. Beamforming maps for the jet from the conic nozzle with the centerbody operated at pressure matched condition using the large aperture logarithmic spiral microphone array.

⁷Papamoschou, D., Morris, P. J., and McLaughlin, D. K., "Beamformed Flow-Acoustic Correlations in a Supersonic Jet," *AIAA Journal*, Vol. 48, 2010, pp. 2445–2453.

⁸Dougherty, R. P., "Improved Generalized Inverse Beamforming for Jet Noise," *American Institute of Aeronautics and Astronautics Paper 2011-2769*, 2011.

⁹Murray, N., Lyons, G., Tinney, C. E., Donald, B., Baars, W., Thurow, B., Haynes, H., and Panickar, P., "Synchronous Near/Far-Field Acoustics and MHz PIV in High-Temperature, Shock-Containing Jets," *Proceedings of the Internoise 2012/ASME NCAD meeting, Paper ASME/NCAD-1270*, 2012.

¹⁰Kannepalli, C., Arunajatesan, S., and Dash, S., "RANS/LES methodology for supersonic transverse jet interactions with approach flow," *American Institute of Aeronautics and Astronautics Paper 2002-1139*, 2002.

¹¹Calhoun, W., Kannepalli, C., Arunajatesan, S., and Dash, S., "Analysis of Scalar Fluctuations at High Convective Mach Numbers," *American Institute of Aeronautics and Astronautics Paper 2002-1087*, 2002.

¹²Erwin, J. P., Sinha, N., and Rodebaugh, G. P., "Hot Supersonic Noise Predictions using High-Resolution Large Eddy Simulation," *2012 High Performance Computing Modernization Program Contributions to DoD Mission Success*, 2012.

- ¹³Arunajatesan, S. and Sinha, N., "Hybrid RANS-LES modeling for cavity aeroacoustics predictions," *International Journal of Aeroacoustics*, Vol. 2, 2003, pp. 65-93.
- ¹⁴Freund, J. B., "Noise sources in a low-Reynolds-number turbulent jet at Mach 0.9," *Journal of Fluid Mechanics*, Vol. 438, 2001, pp. 277-305.
- ¹⁵Lyrantzis, A., "Surface integral methods in computational aeroacoustics From the (CFD) near-field to the (Acoustic) far-field," *International Journal of Aeroacoustics*, Vol. 2, No. 2, 2003, pp. 95-128.
- ¹⁶Shur, M. L., Spalart, R. P., Strelets, M. K., and Garbaruk, A. V., "Further Steps in LES-Based Noise Prediction for Complex Jets," *American Institute of Aeronautics and Astronautics Paper 2006-0485*, 2006.
- ¹⁷Bodony, D. J. and Lele, S. K., "Current Status of Jet Noise Predictions Using Large-Eddy Simulation," *AIAA Journal*, Vol. 46, 2008, pp. 364-380.
- ¹⁸Brentner, K. S. and Farassat, F., "An analytical comparison of the acoustic analogy and Kirchhoff formulation for moving surfaces," *AIAA JOURNAL*, Vol. 36, No. 8, 1998, pp. 1379-1386.
- ¹⁹Farassat, F., "Derivation of Formulations 1 and 1A of Farassat," *NASA Technical Memorandum-2007-214853*, 2007.
- ²⁰Sinha, N., Erwin, J., and Kannepalli, C., "LES Predictions of Noise Emissions From a Low-Bypass Ratio Military Gas Turbine Engine," *Journal of Engineering for Gas Turbines and Power*, Vol. 133, No. 4, 2011, pp. 041202.
- ²¹Erwin, J. P. and Sinha, N., "Near and Far-Field Investigations of Supersonic Jet Noise Predictions Using a Coupled LES and FW-H Equation Method," *ASME Conference Proceedings*, Vol. 2011, No. 54617, 2011, pp. 91-100.
- ²²Erwin, J. P., Sinha, N., and Rodebaugh, G. P., "Large Eddy Simulations of Supersonic Impinging Jets," *Journal of Engineering for Gas Turbines and Power*, Vol. 134, No. 12, 2012, pp. 121201.

Appendix D: Presentation Slides from Panickar *et al.* AIAA-2013-0613.

Localization of Acoustic Sources in Shock-Containing Jet Flows Using Phased Array Measurements

51st AIAA Aerospace Sciences Meeting 2013

Paper: 2013-0613

Session: AA-05, Jet Noise III

January 9th, 2013

Praveen Panickar, James Erwin, and Raj Sinha

*Combustion Research & Flow Technology, Inc. (CRAFT-Tech),
6210 Keller's Church Road, Pipersville, PA 18947*

Nathan Murray, and Gregory Lyons

*National Center for Physical Acoustics,
The University of Mississippi, University, MS-38677*

Funding for this work was provided by the Office of Naval Research under a project that is being jointly conducted by the University of Mississippi, The University of Texas at Austin, Auburn University and CRAFT Tech. Supercomputing resources were provided by the Department of Defense High Performance Computing Modernization Program (DoD HPCMP).



OUTLINE OF THE PRESENTATION

- Motivation and problem definition,
- Flow configuration and geometry,
- CFD methodology,
- Experimental facility,
- Flow characteristics from CFD,
 - Mean flow characteristics,
 - Farfield acoustics and comparison with experimental measurements,
- Insights from experimental beamforming calculations,
- Beamforming using CFD data,
- Conclusions and future work.



• Page 1 • Prev • Next • Last • Full Screen • Close

MOTIVATION AND PROBLEM DEFINITION

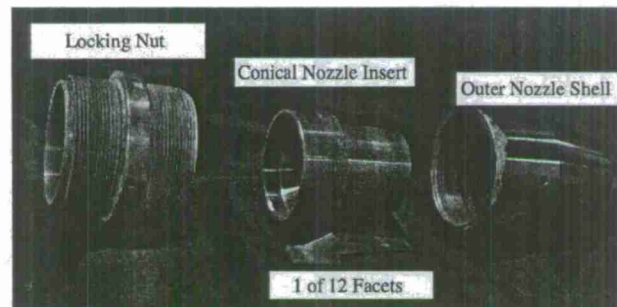
- Jet noise from military aircraft engines fall into two categories: turbulent mixing noise and shock noise,
- Better understanding of the characteristics of these components is necessary to further efforts in development of control and suppression strategies,
 - Changes with jet operating conditions (NPR and TTR),
 - Changes with nozzle geometry,
- Beamforming techniques can provide valuable insight into the location and distribution of acoustic sources in jet flows,
- These techniques, combined with high fidelity simulation data, can be used to guide the design of acoustic suppression devices in a more cost effective way compared to expensive fabrication and laboratory testing.

Perform beamforming calculations on simulated jet flows in order to demonstrate the feasibility of obtaining acoustic source localization and distribution information; identify important parameters and establish the guidelines necessary for reliably performing these calculations.



• Page 2 • Prev • Next • Last • Full Screen • Close

FLOW CONFIGURATION AND GEOMETRY

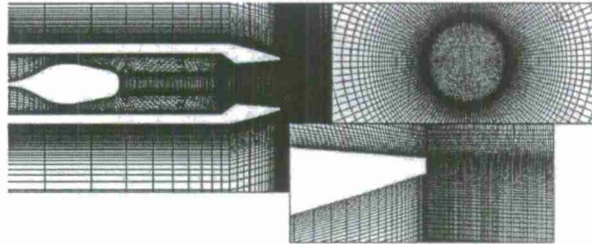


- 2 inch exit diameter CD nozzle with conic convergent and divergent sections, operated with a centerbody upstream of the convergent section,
- Nozzle design Mach number based on area ratio = 1.74,
- Nozzle stagnation temperature = 1350 °F.



• Page 3 • Prev • Next • Last • Full Screen • Close

CFD METHODOLOGY



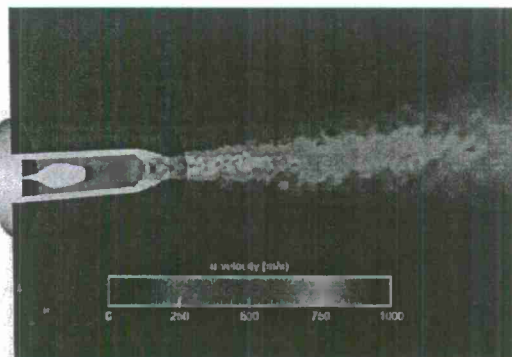
- ~ 7 million grid points,
- CRAFT CFD® solver using hybrid RANS-LES (HRLES) model with time step $\approx 5e-8$ seconds,
- 5th order (spatially) upwind differencing scheme and various time integration schemes including a 2nd order ADI and various Runge-Kutta schemes,
- Parallelized using MPI.



• Page 4 • Prev • Next • Last • Full Screen • Close

CFD METHODOLOGY

HRLES SIMULATION - FARFIELD ACOUSTICS

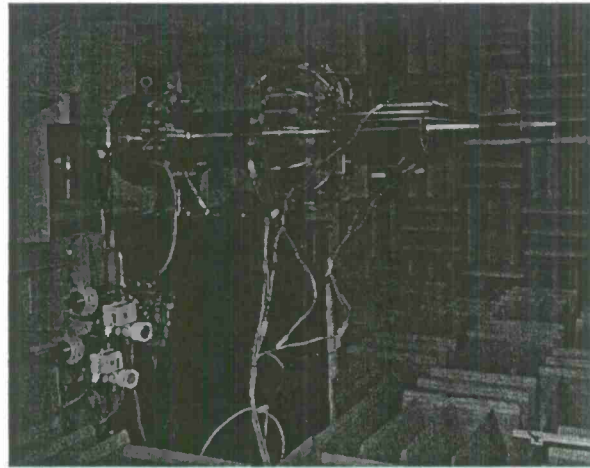


- Time resolved data recorded on an acoustic data surface; this data is used to compute the noise at desired farfield microphone locations using the Ffowcs-Williams and Hawkins (FW-H) method.



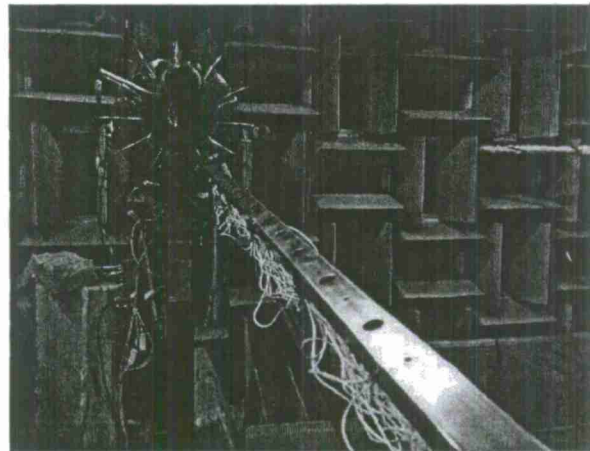
• Page 5 • Prev • Next • Last • Full Screen • Close

EXPERIMENTAL FACILITY



• Page 6 • Prev • Next • Last • Full Screen • Close

EXPERIMENTAL FACILITY



• Page 7 • Prev • Next • Last • Full Screen • Close

MEAN FLOW CHARACTERISTICS

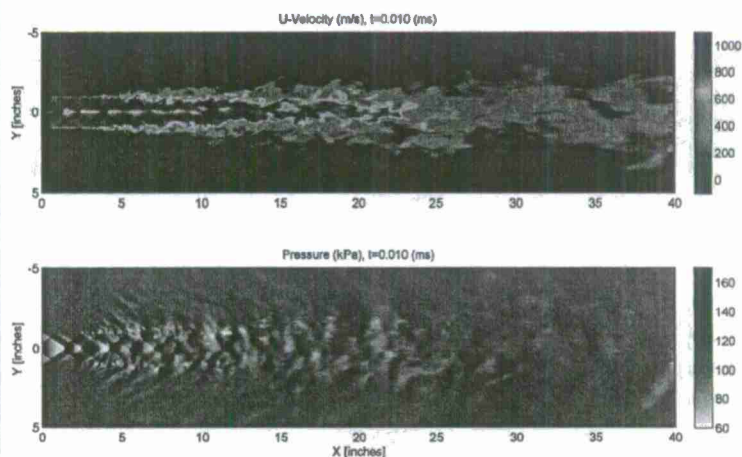


- Time resolved simulations: CFD timestep = 5.0×10^{-8} seconds,
- Wake from centerbody clearly seen
- Double-diamond shock cell structure due to shocks downstream of the sharp throat and at the nozzle exit can also be clearly seen.

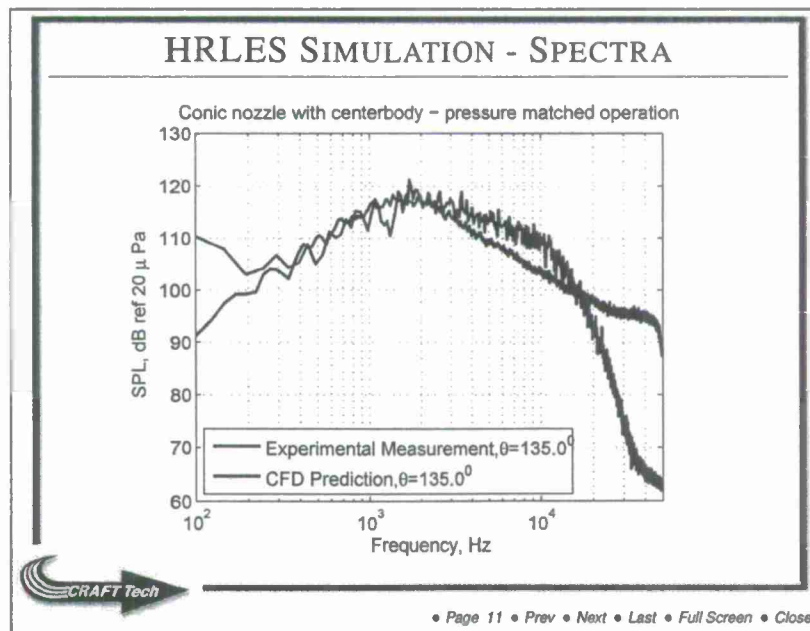
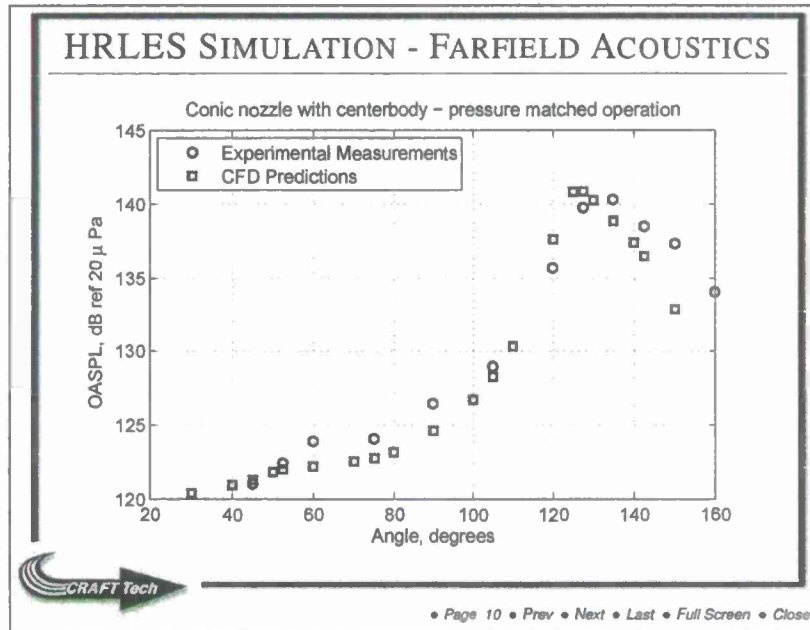


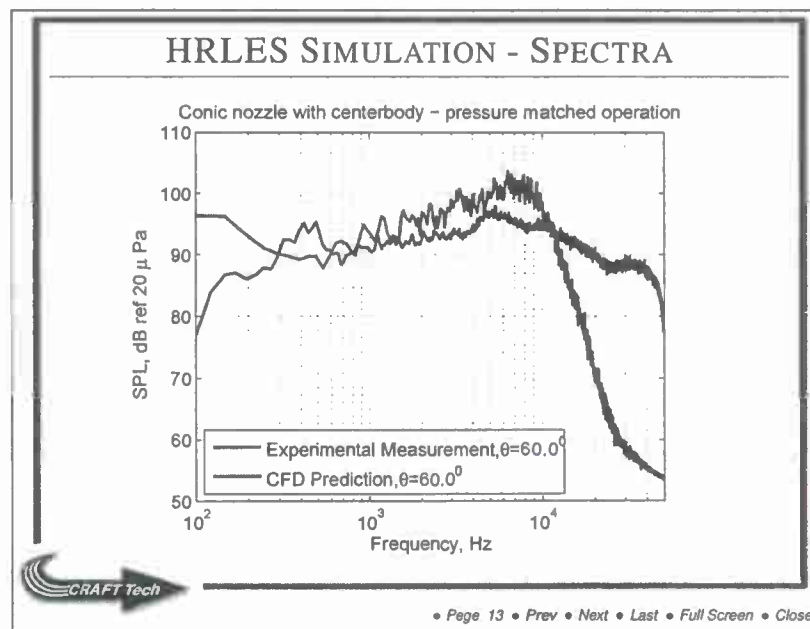
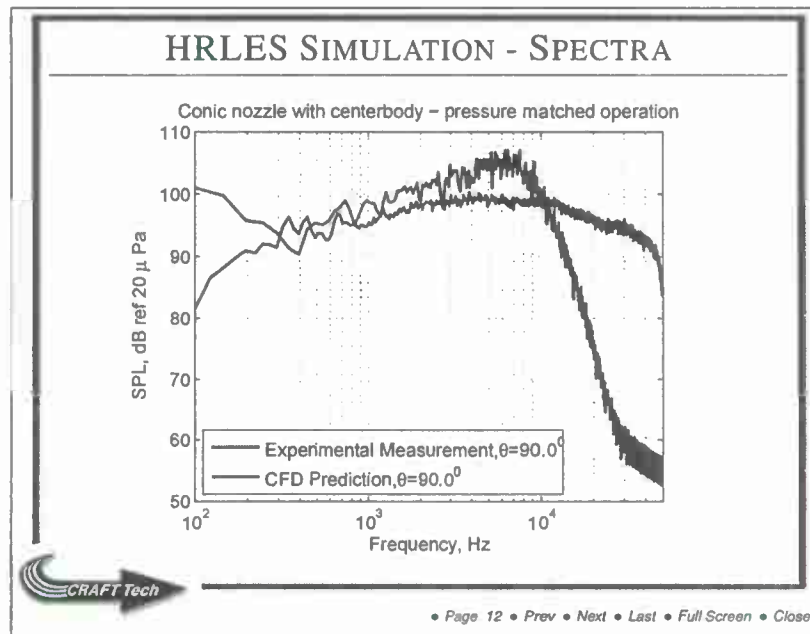
• Page 8 • Prev • Next • Last • Full Screen • Close

INSTANTANEOUS VELOCITY AND PRESSURE



• Page 9 • Prev • Next • Last • Full Screen • Close





PHASED ARRAY CALCULATIONS

PROS AND CONS OF PHASED ARRAY CALCULATION IN CFD DOMAIN

- Use acoustic data surface and Ffowcs-Williams Hawking method to calculate time resolved data at desired microphone location; these locations may not be feasible in a laboratory setting due to spatial or flowfield restrictions.
- Allows for rapidly reconfigurable phased arrays of different designs that can be used to simultaneously "view" the jet flowfield,
 - Can use different phased array design for different frequencies of interest without associated costs of building and setting up a new array.
- Allows for use of many more microphones than practically feasible in experimental work.
- The challenge lies in obtaining 'enough' ensembles in order to sufficiently resolve cross-correlation estimates between the microphones.

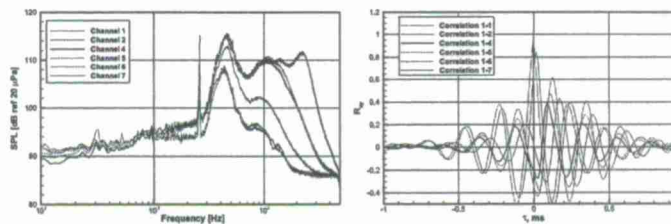


• Page 14 • Prev • Next • Last • Full Screen • Close

EXPERIMENTAL PHASED ARRAY STUDY

EFFECT OF NUMBER OF ENSEMBLES

- Linear array of 32 microphones with logarithmically varying spacing between them,
- Selected configuration of cold, overexpanded jet ($M_j = 1.55$) from a conic nozzle with a centerbody,
- Sample rate = 100 kHz, 1024×1024 samples acquired.
- Traditional delay-and-sum (DAS) beamforming calculations.

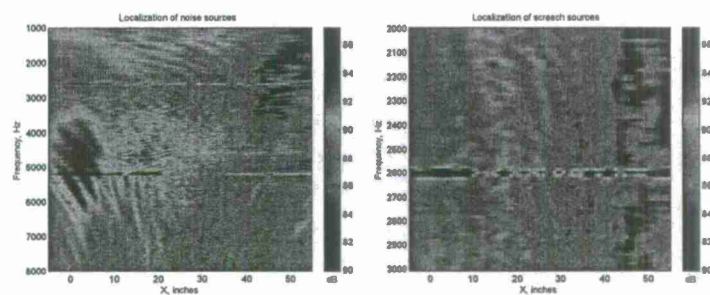


• Page 15 • Prev • Next • Last • Full Screen • Close

EXPERIMENTAL PHASED ARRAY STUDY

128 ENSEMBLES

- Blocksize of 8192 points, $\Delta f = 12.21$ Hz...

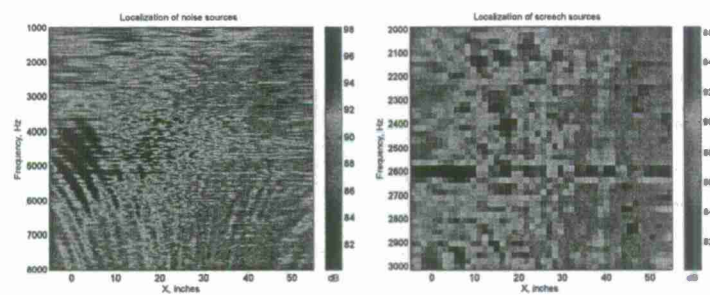


• Page 16 • Prev • Next • Last • Full Screen • Close

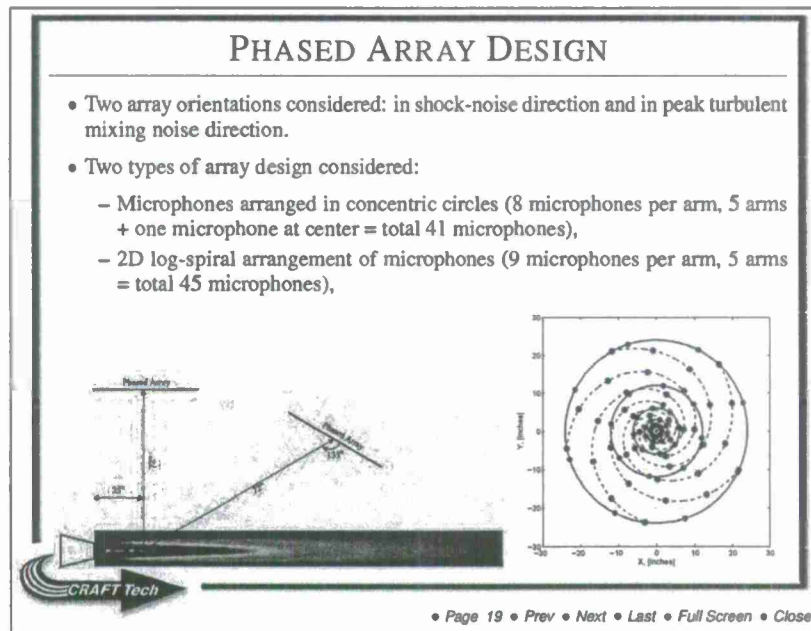
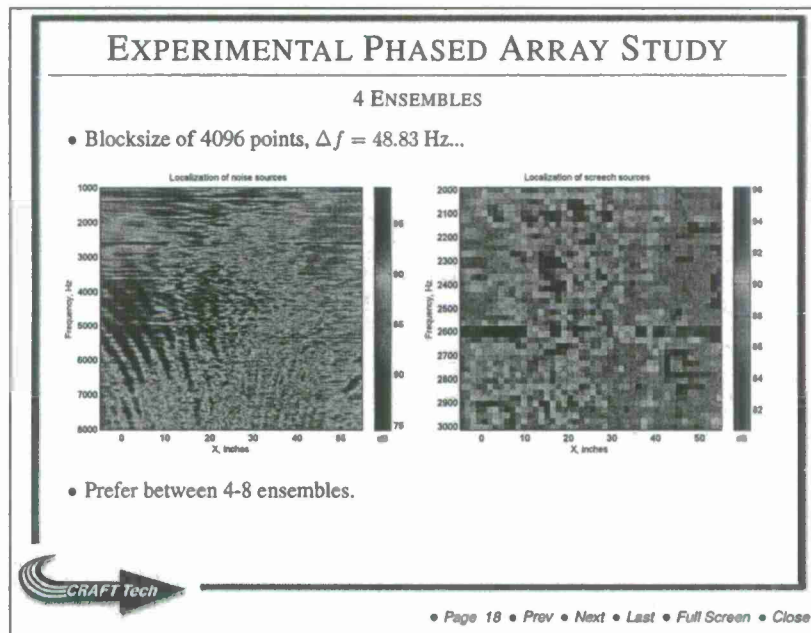
EXPERIMENTAL PHASED ARRAY STUDY

8 ENSEMBLES

- Blocksize of 4096 points, $\Delta f = 24.41$ Hz...



• Page 17 • Prev • Next • Last • Full Screen • Close



CFD PHASED ARRAY METHODOLOGY

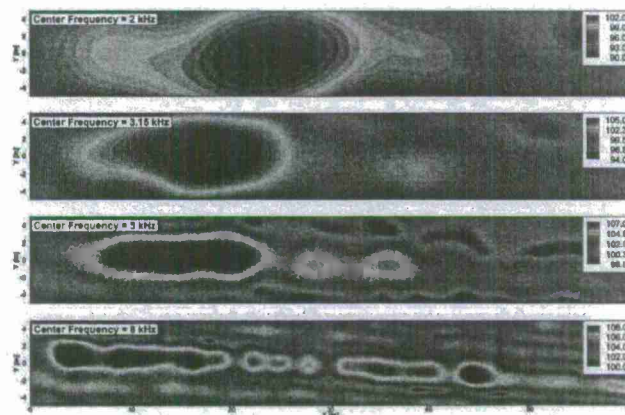
- Using FWH method, obtain time resolved, fluctuating pressure data at phased array microphone locations,
- Calculate and save cross-spectral matrices (CSM) at each narrowband frequency, $G_f(m,n)$, where m and n are microphone indices and f is the narrowband frequency,
 - Hanning window applied in time domain,
 - 6 bins containing 4096 points each, frequency resolution, $\Delta f = 48.83$ Hz,
 - Diagonal elements of the CSM are deleted (reduces self noise from microphones),
- Perform classical beamforming (a.k.a delay-and-sum beamforming) calculations in the $X - Y$ (streamwise-vertical) plane with spatial resolution of $\Delta x = \Delta y = 0.25$ inches.
- Array offset for 2D phased arrays = 72 inches.
- Beamforming results presented in 1/3rd octave bands by summing results at each constituent narrowband frequency between the high and low frequency limits of that band.



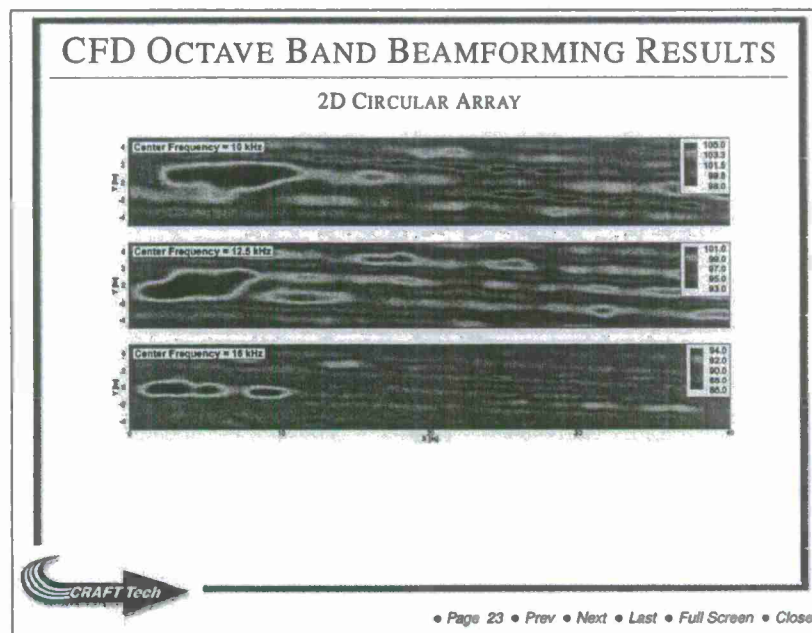
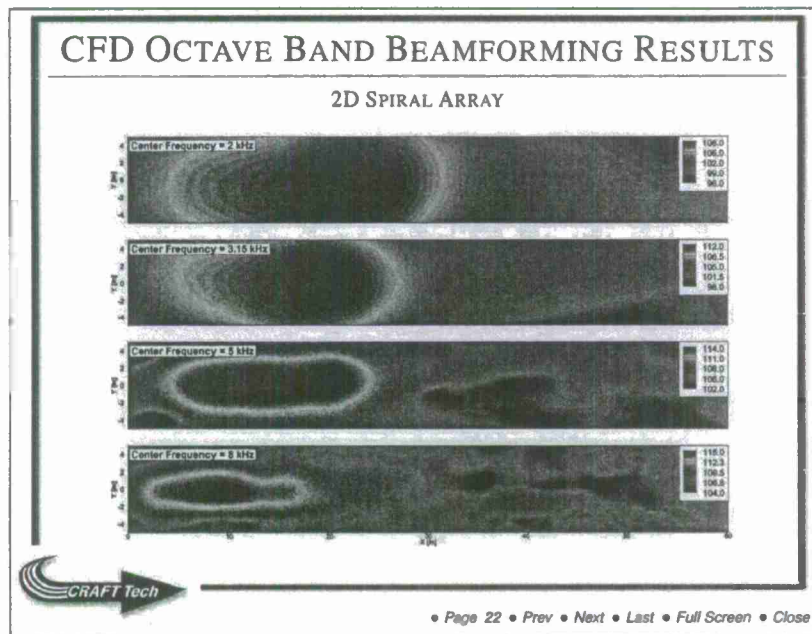
• Page 20 • Prev • Next • Last • Full Screen • Close

CFD OCTAVE BAND BEAMFORMING RESULTS

2D CIRCULAR ARRAY

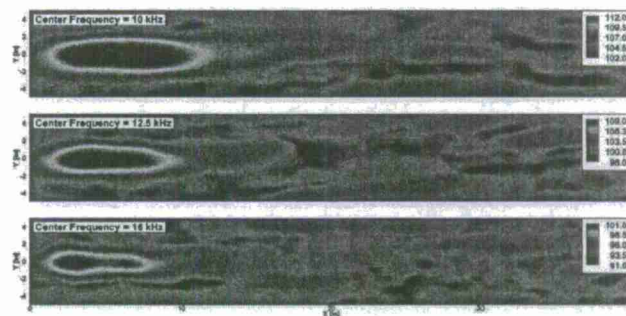


• Page 21 • Prev • Next • Last • Full Screen • Close



CFD OCTAVE BAND BEAMFORMING RESULTS

2D SPIRAL ARRAY



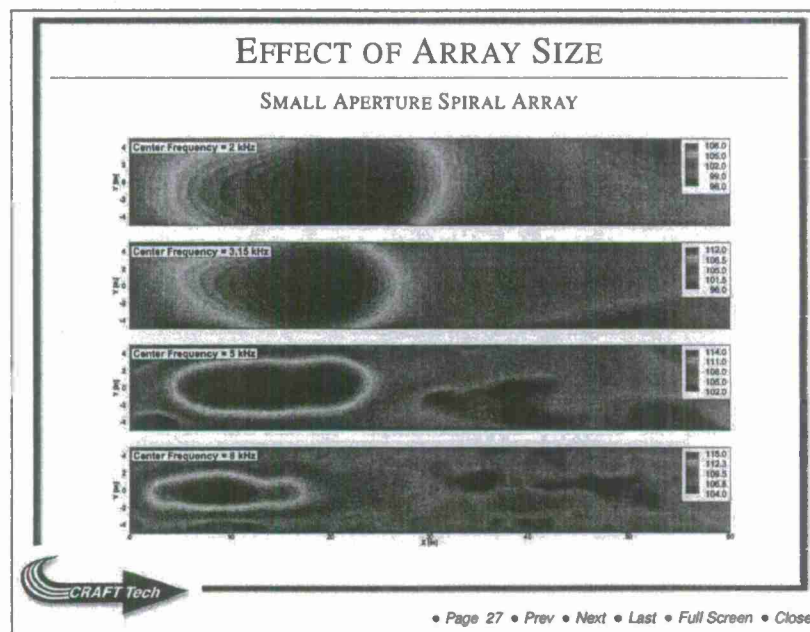
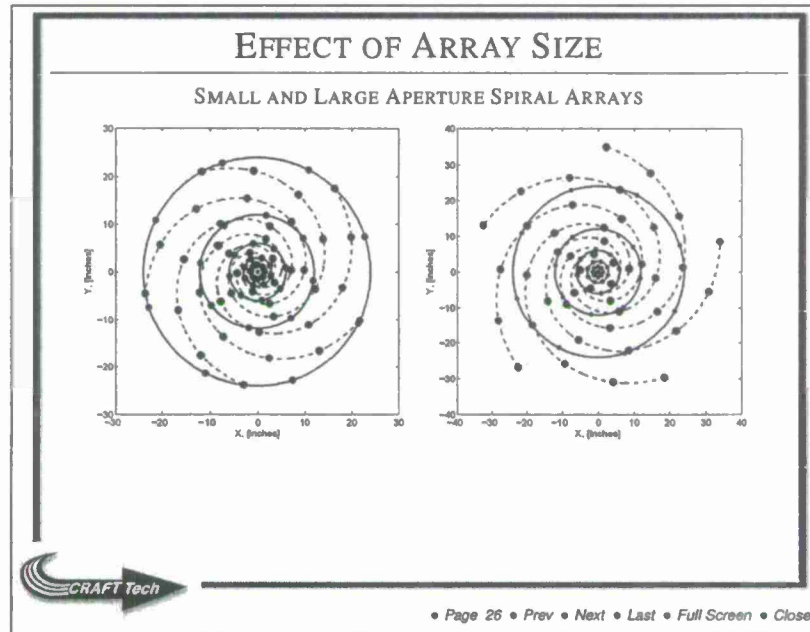
• Page 24 • Prev • Next • Last • Full Screen • Close

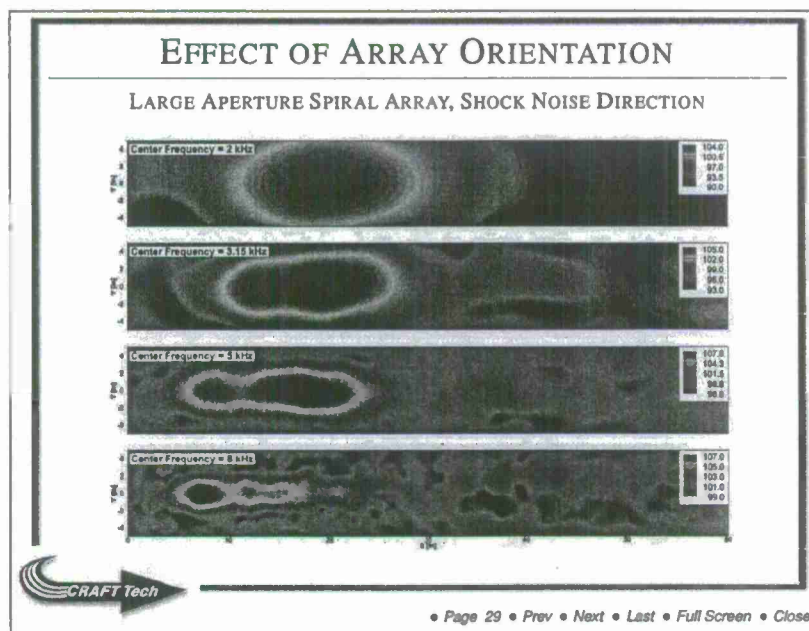
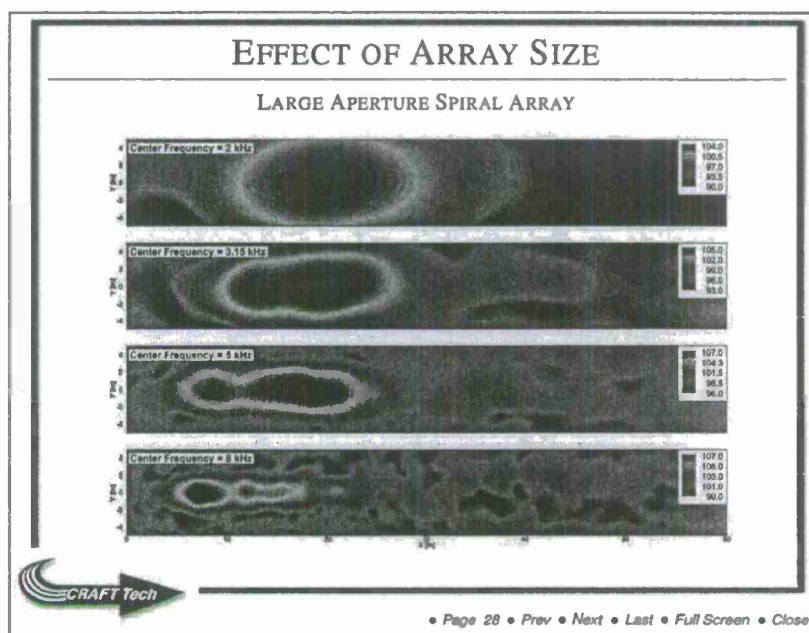
INSIGHTS FROM PRELIMINARY BEAMFORMING CALCULATIONS

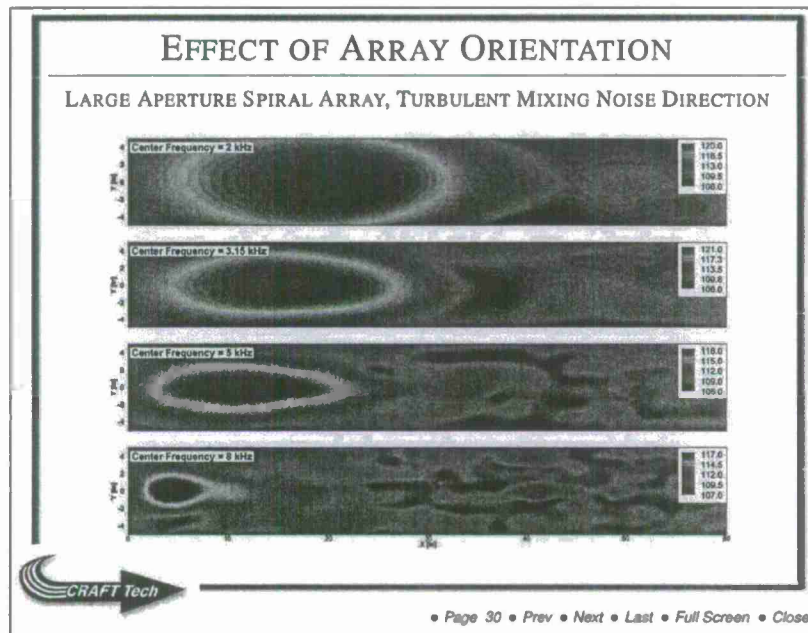
- DAS beamforming shows the presence of acoustic sources that appear to move closer to the jet exit as the 1/3rd octave band center frequency is increased.
 - At the lower frequency the source region extends as much as 12-15 nozzle diameters downstream of the nozzle exit,
 - At the higher frequencies, the sources appear as distinct packets, probably corresponding to the shock cell pattern.
- Results emphasize the feasibility of beamforming calculations on CFD simulations as a viable technique to study acoustic source characteristics of various jet configurations.
- Results are in qualitative agreement with references showing experimental beamforming studies on hot, shock-containing jets (Dougherty and Podboy (AIAA Paper 2009-3186), Brooks, Humphreys and Plassman (AIAA Paper 2010-3780), and Podboy, Bridges and Henderson (2010 NASA TM)).



• Page 25 • Prev • Next • Last • Full Screen • Close







CONCLUSIONS AND FUTURE WORK

- Beamforming of simulated data is a feasible alternative to building experimental phased arrays for localizing acoustic sources in a jet flow
 - Eliminates restrictions on number of sensors that can be used,
 - Allows for design and calculations using multiple sensor arrays that would not be practically feasible (space and cost considerations),
- Produce simulation data with higher frequency resolution to resolve locations of high-frequency sources,
- Extend beamforming methods to include different free jet flow configurations and geometries,
- Determine dependence, if any, of amount of time-resolved data required given different flow situations,
- Incorporate additional beamforming methods (DAMAS, GINV and CLEAN-SC).

[Page 31](#) • [Prev](#) • [Next](#) • [Last](#) • [Full Screen](#) • [Close](#)

Appendix E: Haynes *et al.* "Application of MHz Frame Rate, High Dynamic Range PIV to a High-Temperature, Shock-Containing Jet." AIAA Paper 2013-0774.

51st AIAA Aerospace Sciences Meeting Including the New Horizons Forum and Aerospace Exposition
07 - 10 January 2013, Grapevine (Dallas/Ft. Worth Region), Texas

AIAA 2013-0774

Application of MHz frame rate, high dynamic range PIV to a high-temperature, shock-containing jet

R. Harris Haynes*, Bryan A. Brock*, and Brian S. Thurow†

Department of Aerospace Engineering, Auburn University, 211 Davis Hall, Auburn, Alabama 36849, USA

An experimental investigation is described for the study of a high-temperature, shock-containing jet emanating from a conic-section, converging-diverging nozzle. Particle image velocimetry (PIV) measurements were acquired for a flow field centered axially at the end of the jet potential core and radially along the lower half of the shear layer. For all cases the nozzle was operated at over-expanded conditions, and PIV images were acquired through the combined use of a pulse burst laser and a high-speed, gated intensified CCD framing camera. Because the system could acquire sequences of 16 images at MHz frame rates, temporally resolved measurements were able to be obtained. Each component of the unique PIV system is described in detail along with the experimental setup. In addition, a computational procedure developed for high dynamic range (HDR) analysis is presented with accompanying, sample results. Estimations of the measurement errors associated with these results are also given. Finally, steps for improving the quality of the experimental data as well as the analysis procedure are offered as suggestions for future investigations.

I. Introduction

The work presented in this paper is part of a larger, collaborative effort to investigate the turbulence associated with jet noise generation. In addition to particle image velocimetry (PIV), synchronous near-field and far-field acoustic measurements were obtained to better quantify the noise generated by supersonic flows emanating from converging-diverging (C-D) nozzles. Such noise is associated with typical variable-area nozzles found on modern, high-performance, military aircrafts and consequently is of interest due to concerns over noise-induced hearing loss as well as degraded operational awareness. The cumulative data from these studies provides temporally resolved, synchronous characterization of the near-nozzle velocity field, the hydrodynamic pressure field, and the acoustic far field. By studying the noise-generating features of high-temperature, shock-containing jets using several measurement techniques, the hope is that a better understanding of near-nozzle flow conditions and their impacts on jet noise radiation can be obtained.

The following sections provide a comprehensive overview of the experimental research that was performed for this paper, that is, the acquisition of time-resolved (TR) PIV data for the near-nozzle flow field encompassing the collapse of the jet potential core (descriptions and preliminary results for the near-field and far-field acoustic investigations are available in Murray et al.¹). The aeroacoustic motivation for this work is provided by introducing the problem of jet noise. Following such background information, accompanying sections are given that depict the experimental setup and the corresponding, operational parameters. The specialized facility where measurements were performed is described in conjunction with the unique PIV system that was used. It should be noted that results obtained for this experimental investigation will be presented at a later time. The aim of this paper is to discuss the development of a high dynamic range (HDR) processing scheme that will supplement conventional forms of PIV data analysis. The proposed HDR algorithm and its validation using synthetic particle images are presented in section IV. Steps for improving this HDR procedure are offered in the final section along with other concluding remarks.

*Graduate Research Assistant, Department of Aerospace Engineering. Student Member AIAA.

†Associate Professor, Department of Aerospace Engineering. Senior Member AIAA.

II. Experimental overview

Despite over 60 years of research in jet aeroacoustics, a limited understanding persists in regards to turbulent jets and the mechanisms responsible for turbulent noise generation. Not only has a universal definition of turbulent noise sources eluded theorists, but what constitutes a source mechanism and how such mechanisms can be rendered less efficient (as it pertains to sound generation) remain unknown. From an experimental standpoint attempts to model, measure, and control turbulent jets have been thwarted by instrumental constraints. More often than not, such constraints have resulted from inadequate sensitivities and insufficient frequencies to accurately capture or noticeably influence phenomena of interest. Until a better understanding of source mechanisms is achieved, efforts designed to eliminate or even minimize jet noise radiation will continue to be at the forefront of aeroacoustic research.

For the purposes of this paper in connection with the Jet Noise Reduction (JNR) program of the Office of Naval Research (ONR), jet noise corresponds to the high-amplitude sound generated by air-breathing propulsion systems, namely low-bypass turbine engines. At present it represents one of the most acute noise sources for the Department of Navy and has been linked to adverse biological, mechanical, and environmental effects. Such effects include but are not limited to the noise-induced hearing loss of Navy personnel, the structural degradation of Naval airframes, and the restriction of maintenance, testing, and training schedules due to noise pollution in communities surrounding Naval installations.² To counteract these issues and combat the problem of jet noise, attempts are being made to realize and establish jet noise reduction technologies through coordinated science efforts. The multitude of experiments undertaken in this investigation represents one such effort. As mentioned, while the overall project goal is to obtain a benchmark-quality data set that includes time-dependent, velocity-field measurements along with synchronized near-field and far-field pressure signals, the research presented in this paper is solely concerned with the characterization of the near-nozzle velocity field.

II.A. Anechoic Jet Laboratory

Experiments were conducted in the Anechoic Jet Laboratory (AJL) at the Jamie Whitten National Center for Physical Acoustics (NCPA) on the campus of the University of Mississippi. The AJL is a small facility purpose built for the study of high-temperature, supersonic jet noise.³ To overcome the shortcomings of previous facilities, specifically the NASA Langley Small Anechoic Jet Facility (SAJF), the AJL is designed to allow for aspiration of the test chamber. Using a 10,000 standard cubic feet per minute (SCFM) fan, ambient air can be pulled through the facility at speeds of approximately 1 ft/s (measured without jet flow in the anechoic section). Because of upstream and downstream *stagnation* chambers, the air actually percolates into the 19-by-20-by-8 ft test chamber (measured between the wedge tips) through 50% porosity sliding panels in the upstream and downstream walls. This mode of operation results in a very even temperature distribution throughout the room while maintaining an acoustically anechoic environment. By aspirating the entire chamber, problems associated with localized heating can be minimized along with adverse effects on the jet entrainment due to the enclosed space. Figure 1 provides a view of the test chamber in the AJL with various measurement systems in place.

The jet rig visible in figure 1 and shown specifically in figure 2 is supplied air from an 1100 hp Ingersoll-Rand Centac compressor through a desiccant dryer system. A maximum volumetric flow rate of 5000 SCFM of dry (-40°F) air at 125 psia enables continuous operation of the facility at desired test conditions. Control valves operated in a closed-loop system allow the exit Mach number to be maintained within 1% of a specified value. Heat can be added to the flow through the use of a gaseous propane burner system as shown in figure 2(b). The actual propane combustor is housed well upstream of the nozzle assembly and is followed by a ceramic flow straightener and settling chamber. Although multiple nozzle assemblies exist for this system, only the configuration shown in the schematic that includes the centerbody section was utilized for the work in this paper. Investigations to characterize the effects produced by the other nozzle assemblies are currently underway. The compilation of results for each of these configurations will be presented in a future work.

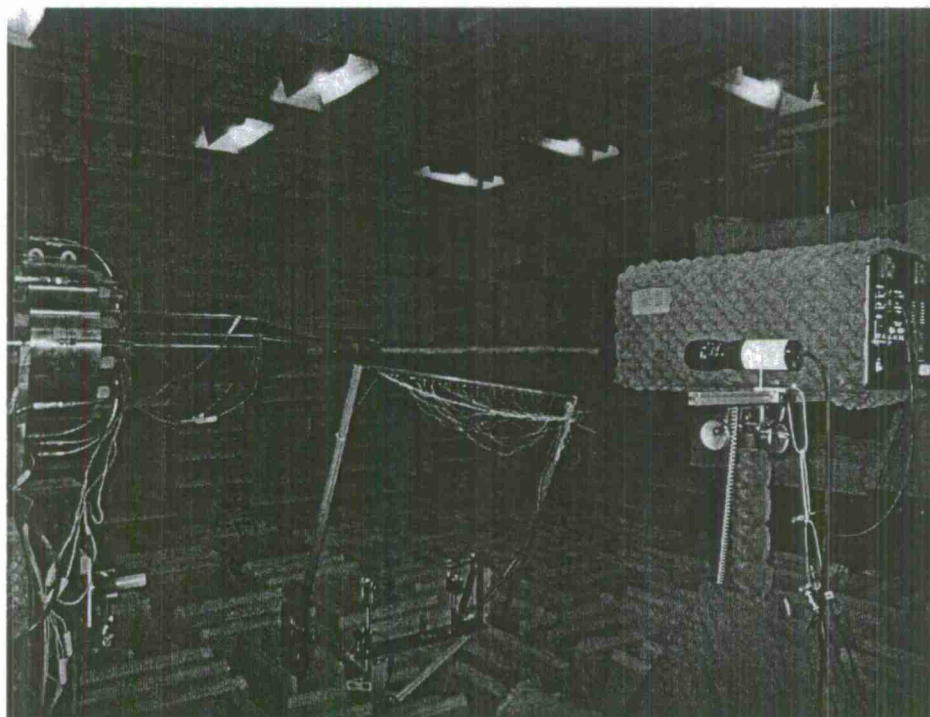
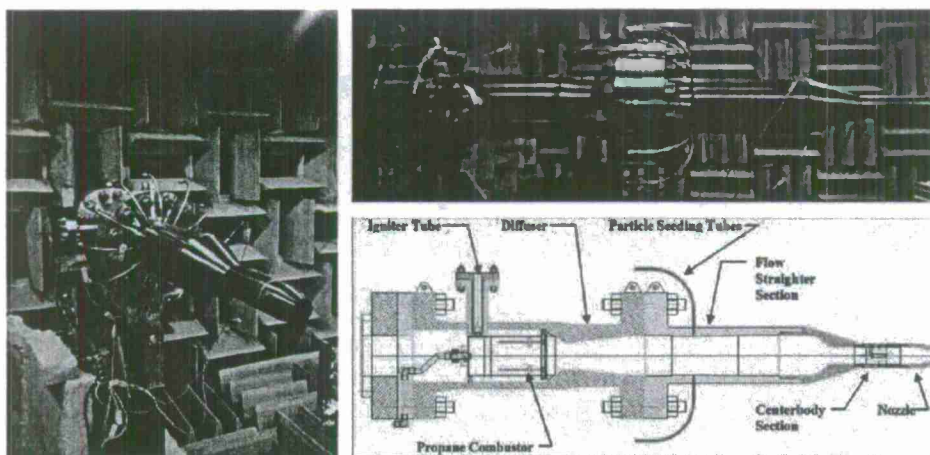


Figure 1. Experimental setup in the test chamber of the Anechoic Jet Laboratory (AJL).



(a) Jet rig in the AJL

(b) Jet rig schematic (Murray et al.¹)

Figure 2. AJL propane burner system and nozzle assembly.

II.B. MHz frame rate PIV system

A MHz frame rate PIV system was developed through the combined use of a pulse burst laser and a high-speed, gated intensified CCD framing camera. For its ability to acquire sequences of 16 images at MHz frame rates, the system allowed temporally resolved velocity-field measurements to be obtained for a high-temperature, supersonic jet. Each component of the unique PIV system is explained in detail along with the experimental setup. Although this system was synchronized with both near-field and a far-field pressure measurement devices, only the PIV system is considered for the purposes of this paper.

II.B.1. Pulse burst laser

As has been described in previous publications,⁴⁻⁶ a pulse burst laser system developed at Auburn University allows a specified number of high-energy, MHz rate laser pulses to be formed for a given burst of low-energy, short-duration pulses. It should be noted that several upgrades have been made to this system since these publications, including a new JDSU NPRO 126 continuous-wave (CW) Nd:YAG laser to enhance the pulse-to-pulse stability of each burst. This component in particular results in more consistent illuminations between images and thus better results in the PIV cross-correlations. In addition to the CW laser, three supplementary amplification stages have been incorporated into the system (for a total of six amplification stages) to increase the overall energy available for each burst and consequently each individual laser pulse. A schematic of the upgraded pulse burst laser system is shown in figure 3.

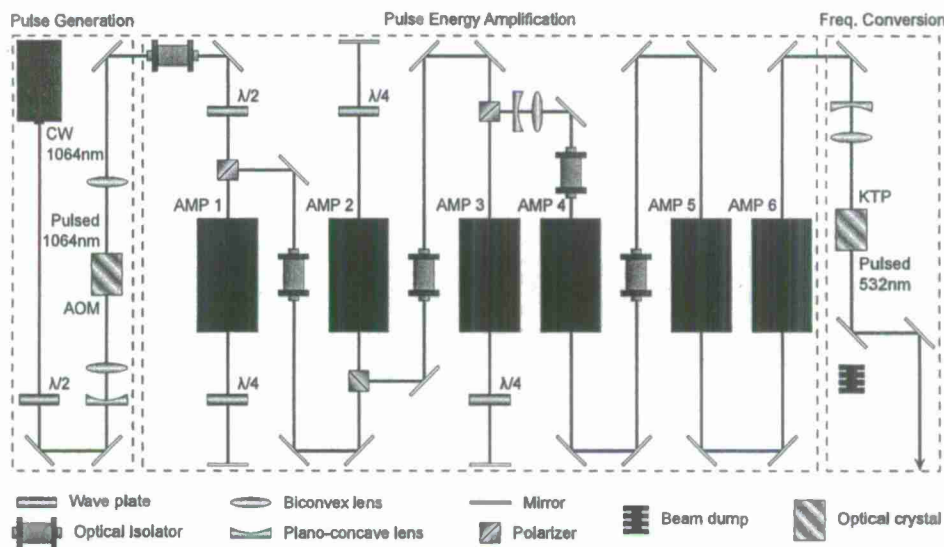


Figure 3. Pulse burst laser system utilized for time-resolved (TR) PIV (top view).

The design of the pulse burst laser system can be divided into three fundamental parts as indicated in the schematic: the pulse generation, the pulse energy amplification, and the frequency conversion. As the name suggests, the function of the pulse generation stage is to slice the output of the CW laser into a burst of low-energy, short-duration pulses. Slicing is achieved through the use of an acousto-optic modulator (AOM) that relies on the principles of the acousto-optic (AO) effect. In particular, a piezoelectric transducer is used to produce acoustic waves inside an optical crystal such that the traveling waves cause variations in the index of refraction of the crystal. To an optical beam, these variations appear as a sinusoidal grating in which the wavelength is equal to the acoustic wavelength. By controlling when and how frequently acoustic waves are produced inside the crystal, the generation of a specified number of short-duration pulses is possible depending on how often the CW input beam is disturbed. As with most AO devices, the AOM operates in

the Bragg regime where most of the incident light can be diffracted into the first-order beam fairly efficiently. This diffracted beam constitutes the desired burst of pulses utilized in experimental applications.

Following the formation of low-energy (nanjoule order), short-duration pulses, the remaining stages of the pulse burst laser consist of pulse energy amplification and frequency conversion. Amplification is provided by six flashlamp-pumped Nd:YAG rod amplifiers of increasing diameter and is necessary if the pulses are to be used for fluid-mechanical measurements. The first three amplifiers are used in a double-pass arrangement, whereas the final three allow only for single passes. Without going into detail, wave plates and polarizers provide the necessary means for achieving double passes through the first three amplifiers. Optical isolators between each of the first five amplification stages prevent problems associated with parasitic lasing and amplified spontaneous emission (ASE). By the end of the amplification chain, pulse energies have increased by a factor of more than 10^7 – 10^8 and generally reach levels in excess of 50 mJ/pulse^a.

The final stage of the pulse burst laser system is the conversion of the beam's wavelength from 1064 nm to 532 nm. This conversion is achieved via a nonlinear process inside a KTP crystal and results in an unavoidable loss of pulse energy. Nevertheless the beam, now in the visible spectrum, can be used for fluid-mechanical measurements including PIV and other flow visualization applications.

II.B.2. Cordin 222-4G high-speed camera

Images are acquired using a Cordin 222-4G gated intensified CCD framing camera that is capable of recording 16 images at a maximum, equally spaced rate of 2,500,000 frames per second^b. Such images are captured with a 2048×2048 px² resolution, although the true resolution is less due to the inherent intensification process. The camera is able to achieve extremely high acquisition rates because it contains eight independently controlled optical pathways, each incorporating a microchannel plate (MCP) for signal intensification and ultimately terminating with a Kodak KAI-4022 CCD sensor. Schematics of the camera, including an interior view that illustrates four of the optical pathways, are shown in figure 4. By allowing each CCD to record 2 images, 16 total images can be acquired over a user-specified time period. Furthermore, because each pathway is independently operated, temporal spacing between frames is variable and can be set in an asynchronous fashion. Such flexibility even allows eight simultaneous exposures to be made. This feature is desirable since it enables eight theoretically identical particle images to be obtained, with any differences being directly attributable to error. More discussion on this topic will be given in the follow-up paper that includes the experimental results. For this work it is sufficient to note that because the camera can acquire 16 images over a user-specified, extremely short time period, temporal resolution is possible for all captured fluid motions. Additionally, the ability to obtain several particle images at varying time intervals relative to one another has provided the means of performing HDR PIV. Such measurements offer significant improvements over conventional PIV results since optimum temporal separations can be selected for different particle locations depending on the local velocity.

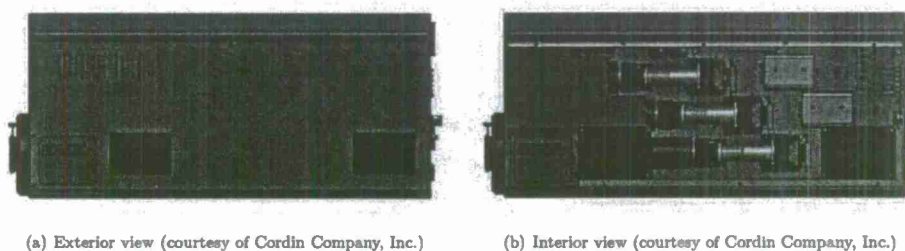


Figure 4. Side profiles of the Cordin 222-4G camera utilized in the TR PIV investigation.

^aThis value is measured after the frequency conversion stage and thus accounts for the loss in energy associated with doubling the frequency of the Nd:YAG laser beam via a KTP crystal.

^bThis rate assumes a necessary CCD transfer time of 3.2 μ s (specified by Cordin) to ensure that the second exposure does not include images from the first exposure.

II.C. Experimental arrangement

The combined use of the pulse burst laser and the Cordin high-speed camera allowed TR PIV measurements to be made on a high-temperature (1350°F), supersonic jet. For all cases only a smooth bore C-D nozzle with an upstream centerbody section (shown in figures 5(a) and 5(b)) was considered at over-expanded conditions (Mach 1.55). Such conditions are typical of aircraft exhaust during takeoff and low-altitude operation. The actual nozzle consisted of two conic sections, one contracting and the other expanding, joined together to form a supersonic nozzle with a very sharp radius of curvature at the throat. This near discontinuity at the throat is significant since it allows shocks to exist even when the nozzle is operated at fully expanded conditions (Mach 1.74). To illustrate this effect, a mean profile of the near-nozzle velocity field determined by CFD is shown in figure 5(c). As indicated in the profile, the streamlined centerbody section was positioned well upstream of the nozzle contraction. It should be noted that this nozzle assembly without the centerbody piece represents a 1/10th scale model of the military power setting for the General Electric F414 engine.

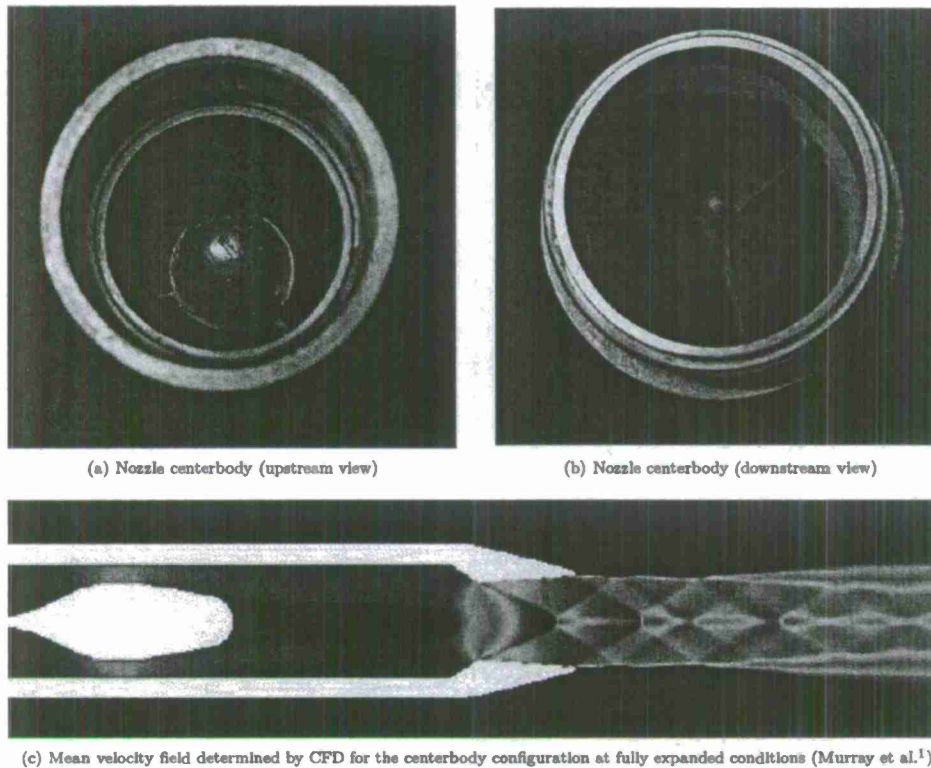


Figure 5. The centerbody section included in the nozzle assembly is shown in (a) and (b). The shock structures existing at fully expanded conditions are evident in (c).

The field of view for this work was chosen along the bottom shear layer of the jet and was centered at a distance 14 inches (7 jet diameters) downstream of the nozzle exit. This distance was selected based on previous measurements indicating the collapse of the jet potential core. The region imaged was slightly less than 16 square inches and was illuminated by a laser sheet directed vertically upwards and spanning axially along the centerline of the jet. This particular orientation was chosen for a variety of reasons including both the need to minimize disruptions in the anechoic environment as well as to ensure the most direct observation

of any shear layer without passing the light sheet through the jet prior to imaging. This last point was especially important to prevent problems associated with aero-optical distortions. Figure 6 illustrates the position of the imaged region relative to the nozzle exit and the jet centerline (drawing not to scale).

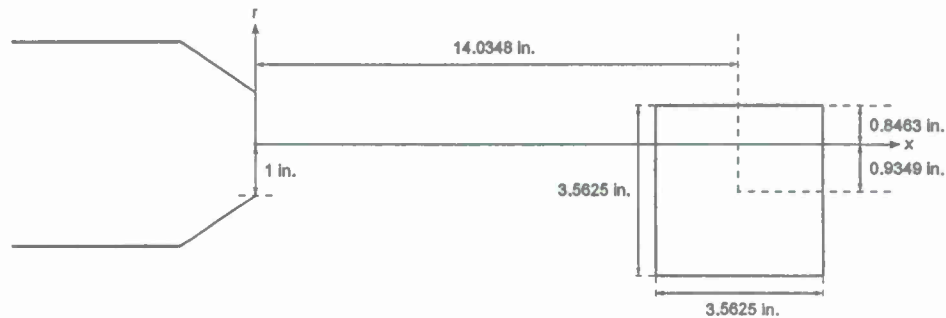


Figure 6. Position of the imaged region in the TR PIV investigation relative to the nozzle exit plane and the jet centerline (side view). The square region indicates the camera's field of view.

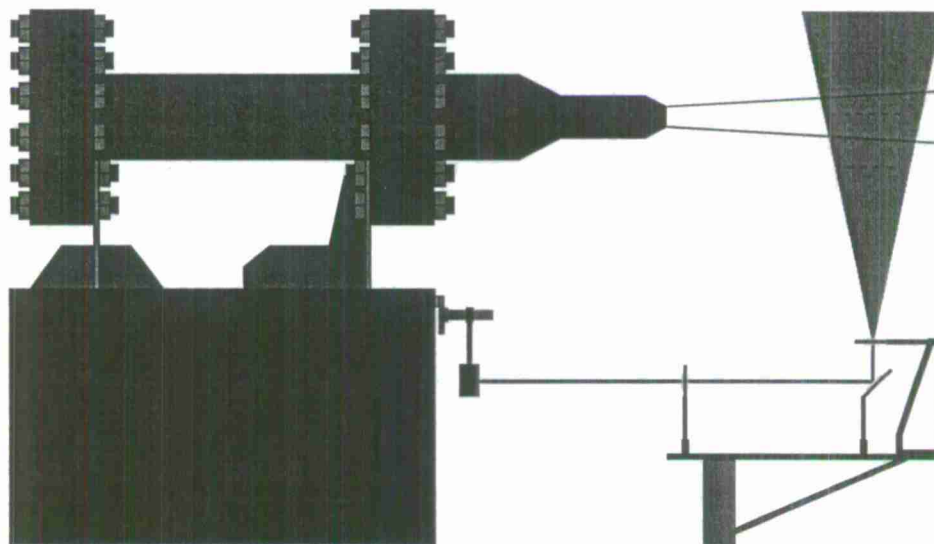


Figure 7. Experimental arrangement for the TR PIV application (side view). The square region enclosed by the dashed line indicates the camera's field of view.

Particle seeding for light scattering was achieved using aluminum oxide (Al_2O_3) particles nominally $0.1 \mu\text{m}$ in diameter. A nitrogen-pressurized reservoir filled with these particles was connected to the burner system upstream of the nozzle assembly and immediately following the propane combustor and diffuser, respectively. Four seeding tubes were attached around the burner system symmetrically to provide a uniform seeding density throughout the jet. To alleviate particle clumping, a spinning propeller inside the reservoir formed a cloud of aluminum oxide particles that was subsequently dispersed into the particle seeding tubes. Each connection between the reservoir and a tube was made in the supersonic portion of a miniature de Laval nozzle located at the entrance to each tube. This arrangement ensured that any surviving particle clumps were sheared apart before being injected into the burner system.

A schematic of the experimental setup is shown in figure 7. The 532 nm wavelength beam from the pulse burst laser was passed into the anechoic chamber perpendicularly to the jet axis and opposite the location of

the camera. A turning mirror attached to the stand for the burner system allowed the beam to be directed downstream of the nozzle exit before encountering a 1000 mm biconvex spherical lens and a second turning mirror. The beam was then redirected vertically upwards through a cylindrical lens to form the laser sheet required for light scattering. Extreme care was taken to ensure that this light sheet was oriented both orthogonally to the axis of the camera lens as well as to the nozzle exit plane. Additionally, the placement of the spherical lens allowed the thinnest portion of the light sheet to persist across the camera's field of view.

PIV measurements were obtained by synchronizing the framing rate of the camera with the pulse-generating rate of the pulse burst laser system. The chosen rate for all cases was 1 MHz, meaning the 16 images acquired by the camera enclosed a temporal window spanning 15 μ s. To achieve the most consistent pulse-to-pulse intensity within each burst, 60 laser pulses were generated for a given burst, and the most stable 16 pulses were selected for synchronization with the 16 camera frames. The duration of each laser pulse was approximately 20 ns such that no image streaking was observed. A Nikon Nikkor F-mount 70-300 mm objective zoom lens (f/4-5.6G) was used with the Cordin camera to acquire all image sequences.

III. The dynamic velocity range in TR PIV

In addition to the lack of three-dimensionality available in PIV, the limited dynamic velocity range represents one of the largest problems currently plaguing the technique.⁷ Although several methods have been developed to extend this range, flows containing a wide velocity distribution still present a major challenge to PIV algorithms. Because particle displacements in these flows can differ drastically depending on the local velocity, computational procedures must be designed to account for temporal variations in particle-image patterns. This section describes a few such approaches that aim to increase the dynamic velocity range of TR PIV measurements. The need for temporal resolution in acquired image sequences is explained first, and various strategies for evaluating these sequences are then presented. Notable techniques included in the discussion are multi-frame PIV, adaptive multi-frame PIV, and adaptive multi-step ensemble correlation. A method known as multiple pulse separation PIV is also mentioned for its relevance to improving the dynamic velocity range, however this technique only provides time-averaged results.

The current interest in TR PIV arises from the need to obtain local accelerations and thus instantaneous pressure fields in unsteady flow environments. Accurate measurements of velocity time derivatives are required in order to evaluate the Lagrangian accelerations of fluid particles and subsequently integrate the spatial field of the pressure gradient.⁸ For the experiments of interest and other applications involving aeroacoustics, the accuracy of such measurements is even more important since double temporal derivatives are required to use the PIV data with corresponding aeroacoustic analogies.⁹ As a result, reliable temporal derivatives must be achieved in PIV measurements if accurate, subsequent flow quantities are to be obtained.

One approach for improving the accuracy of PIV results is to increase the dynamic velocity range of the data. According to Adrian,¹⁰ this range is defined as the ratio of the maximum velocity to the minimum resolvable velocity. Likewise it can also be expressed in terms of the maximum and minimum resolvable particle displacements. Mathematically these relationships can be written as follows.

$$DVR \equiv \frac{u_{max}}{\sigma_u} = \frac{[\Delta x_{max} / \delta t]}{[\sigma_{\Delta x} / \delta t]} = \frac{\Delta x_{max}}{\sigma_{\Delta x}} \quad (1)$$

In equation 1, the dynamic velocity range is represented by DVR, and the maximum and minimum resolvable particle displacements are shown as Δx_{max} and $\sigma_{\Delta x}$, respectively. It should be noted that only velocity magnitudes are assumed in this definition. Thus if negative velocities occur, then u_{max} is defined as the larger of the maximum positive velocity or the maximum magnitude of the negative velocity. At present a DVR of approximately 200:1 is the standard for two-dimensional PIV measurements.¹¹ In applications where ranges begin to exceed this value, the accuracy of vectors in the low-velocity regions starts to deteriorate. For this reason data acquisition rates are generally chosen such that only flow phenomena of interest are properly sampled. Unfortunately this mode of imaging means that vectors calculated in other flow regimes have the potential of being highly inaccurate. Consequently high dynamic range techniques have been developed to improve the evaluation of temporally resolved image sequences.

Although increasing the time interval between subsequent frames is not a preferred method for improving the DVR, a few studies have managed to achieve satisfactory results by applying this approach locally. The problem with using larger temporal separations is the reduction one experiences in the signal-to-noise ratio. A greater pulse separation leads to increased losses between in-plane and out-of-plane particle pairs. To

overcome this limitation, procedures known as multi-frame (MF) PIV have been developed that utilize temporally resolved, single-frame image sequences to locally optimize particle-image displacements.

One of the first MF methods designed to improve the performance of TR PIV is suggested by Fincham and Delerce.¹² The approach revolves around a hierarchical processing scheme that considers the effects of local fluid deformation calculated during successive passes. Following an initial correlation of two frames with a temporal separation of δt , displacement estimates are made for the deformation and correlation of frames separated by larger time intervals ($2\delta t$, $3\delta t$, etc.). By utilizing larger time intervals in subsequent correlations, average pixel displacements are increased and thus the overall DVR enhanced.

Pereira et al.¹³ introduce an alternative MF technique for dealing with temporally resolved image sequences. Termed adaptive multi-frame (AMF) PIV, the technique aims at the minimization of errors found in low-velocity regions by adjusting locally and dynamically the interframe time between particle-image pairs. As before, the algorithm operates on a local basis such that a constant level of accuracy is achieved for all velocity ranges. Hain and Kähler¹⁴ propose a further development of this technique by taking higher-order effects into account. For this case images that symmetrically straddle a shared, central frame are considered. By locally optimizing the particle-image displacements, an optimum temporal separation can be chosen for each interrogation window that minimizes the relative measurement error.

A final method designed to enhance the precision and robustness of TR PIV measurements is introduced by Sciacchitano et al.¹⁵ The technique, referred to as adaptive multi-step ensemble correlation (AMEC), includes aspects of the MF approaches described previously as well as a method known as correlation ensemble averaging.¹⁷ For a short series of recordings separated by a constant time interval, optimum temporal separations are locally evaluated based on error-minimization criteria. Correlation signals acquired at different temporal spacings are linearly combined through the use of homothetic transformations. From comparisons with state-of-the-art PIV processing techniques, the AMEC method has proven to increase the reliability of measured vectors and to significantly reduce both precision and acceleration errors.

Until recently it has not been practical to use MF methods in high-speed flows due to limitations imposed by laser and camera repetition rates. To avoid the use of excessive temporal separations in TR PIV applications, a multiple pulse separation (MPS) technique is proposed by Persoons and O'Donovan.¹⁵ In this technique a series of double-frame images with different pulse separations is recorded such that a sequence with the following temporal distribution is obtained $\{[t, t + n_1\tau], [t + \delta t, t + \delta t + n_2\tau], \dots\}$. The inter-frame time (δt) remains constant, whereas the pulse separation time (τ) grows according to a monotonically increasing multiplier (n_1 , n_2 , etc.). Once a desired sequence has been acquired, vector fields for all pulse separation values are evaluated using standard PIV algorithms. A pulse separation optimality criterion is then applied locally to compute a final displacement field. Because the results encompass multiple pulse separation values, the DVR is dramatically increased compared to velocity fields achieved by conventional methods. Despite this improvement, the MPS technique applies only to mean flow and turbulence quantities since it is unable to provide temporally resolved results.

IV. Dynamic evaluation via ordinary least squares (DEVOLS)

As noted in the previous section, flows containing a wide velocity distribution present a major challenge to PIV algorithms. The reason is because particle motions in these flows (particle displacements in recorded images of these flows) can vary greatly depending on the local velocity. Since the entire range of flow velocities and thus particle motions cannot be adequately captured in a single interframe time, the temporal spacing in conventional PIV applications must be chosen such that only flow phenomena of interest are properly sampled. To overcome this problem and others related to temporal variations in particle-image patterns, HDR techniques like the ones described previously are currently being developed.

This section presents a novel HDR approach designed specifically for the experiments of interest, that is, the characterization of the near-nozzle velocity field in a supersonic jet using TR PIV measurements. The conceptual idea for the approach is based largely on the MF method developed by Hain and Kähler.¹⁴ Using the correlation results of symmetrically centered image pairs with increasing temporal separations, a single velocity field can be constructed entirely from local evaluations. This approach differs from the previous ones, however, in that individual vectors are determined from the combined influence of measurements achieved at multiple interframe times. By considering the results of several image pairs in each local evaluation, significant improvements can be made regarding measurement accuracy and individual vector quality. The following subsection discusses the proposed HDR processing scheme, termed dynamic evaluation via ordinary

least squares (DEVOLS), and its implementation into the experimental analysis. Validation for the procedure is given in the latter subsection by using synthetically generated images with known particle displacements. The effects that particle density and image noise have on the algorithm are specifically addressed.

IV.A. Proposed DEVOLS processing scheme

In the experiments of interest the ability to obtain 16 particle images at varying time intervals with respect to one another has provided the means of performing HDR PIV. Unlike conventional PIV where only one temporal spacing is available for all velocity determinations, the multiple combinations of image pairs in this investigation enable a single velocity field to be constructed from the results of several different local evaluations. In spatial regions where little or no particle motions are observed between subsequent frames, the results of image pairs spanning greater temporal distances are also considered. Thus it is entirely possible for vectors in the low-velocity regions of a flow field to be determined using the results of all available image pairs. In this way the DVR is dramatically improved because velocity ranges corresponding to a variety of interframe times are properly and simultaneously sampled.

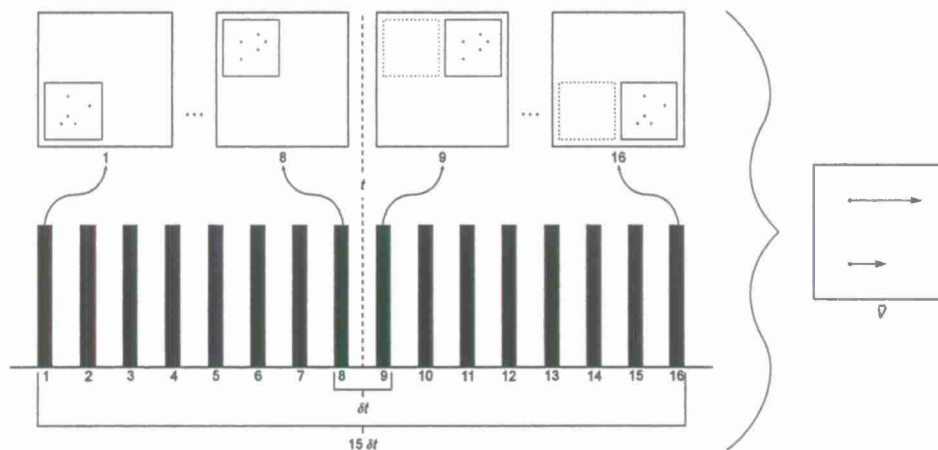


Figure 8. Basic principle of high dynamic range (HDR) PIV in relation to the experiments of interest. A single velocity field at t can be determined by combining the local evaluations of various image pairs. Depending on the local velocity, the number of image pairs utilized for a single vector evaluation is variable. The increased dynamic velocity range compared to conventional PIV allows improved measurements to be obtained.

A schematic illustrating the basic principle of HDR PIV in relation to the experimental investigation is shown in figure 8. As mentioned, sequences of 16 images were able to be obtained in which the δt between subsequent frames was specified to be $1 \mu s$. This particular interval was chosen such that the maximum flow velocities and their corresponding particle-image displacements would produce optimum results in the correlation analyses between consecutive frames. By setting the data acquisition rate to properly sample the maximum flow velocity, the slower velocity ranges were inherently oversampled and thus all image pairs could be used. Considering the temporal arrangement of all 16 frames in the schematic, the velocity field located between frames 8 and 9 is determined by considering the local results of all 8 image pairs symmetrically straddling the point designated t . It should be noted that velocity fields at other points in time could also be computed, however this particular position allows the maximum number of image pairs to be used with central finite differencing. As is evident, for regions of the velocity field containing the highest local velocities, that is, the largest particle displacements between consecutive images, only the image pair shown in red is considered for analysis. Contrarily for regions containing little or no particle motions, multiple image pairs spanning larger temporal distances are considered. The image pair shown in blue represents the case of maximum temporal spacing and spans the entire sequence window of $15 \delta t$ or $15 \mu s$. By using the information available across all 16 frames instead of only consecutive images, significant improvements in desired flow measurements can be made. Revisiting the mathematical relation discussed previously, the reason is because the DVR is increased by a factor of 15 compared to conventional PIV methods. The following equations demonstrate

this effect by combining the individual correlation results for the minimum and maximum interframe times.

$$\begin{array}{ll} \delta t : & 15 \delta t : \\ \boxed{u_{max,1} = \frac{\Delta x_{max}}{\delta t}} & (2) \quad \quad \quad \boxed{u_{max,15} = \frac{\Delta x_{max}}{15 \delta t}} & (4) \\ \sigma_{u,1} = \frac{\sigma_{\Delta x}}{\delta t} & (3) \quad \quad \quad \boxed{\sigma_{u,15} = \frac{\sigma_{\Delta x}}{15 \delta t}} & (5) \end{array}$$

Considering only the relations denoted by the rectangular boxes above (equations 2 and 5), an improved DVR is obtained.

$$DVR \equiv \frac{u_{max,1}}{\sigma_{u,15}} = \frac{[\Delta x_{max} / \delta t]}{[\sigma_{\Delta x} / (15 \delta t)]} = 15 \frac{\Delta x_{max}}{\sigma_{\Delta x}} \quad (6)$$

In the DEVOLS processing scheme all eight symmetrically centered image pairs are correlated in an initial step. This step represents the most computationally expensive and time-consuming portion of the procedure since each correlation utilizes multiple passes along with several of the latest PIV processing techniques (window deformation and subpixel refinement schemes). To perform the correlation analyses, Dantec Dynamics software (DynamicStudio v3.31: Smart Software for Imaging Solutions) is used. In order for a final velocity field to be accurately constructed from local results, it is imperative that the same number of interrogation windows be used in each of the eight correlations. This requirement ensures that the vector spatial locations in each displacement field are positioned and scaled in a 1:1 ratio.

Following the eight correlation analyses, error-minimization criteria are employed to select the most accurate vectors determined at each spatial location. Such criteria are user-specified to allow for increased processing flexibility. To avoid errors stemming from particle accelerations, displacement measurements are restricted by a maximum displacement limit. This upper bound ensures that high velocity regions are only assessed by image pairs spanning the smallest temporal separations. Contrarily it enables low velocity regions to be evaluated by the maximum number of image pairs. In most cases the highest accuracies are achieved when particle displacements are required to satisfy the one-quarter rule. This rule suggests that in-plane displacements should not exceed one-quarter of the interrogation window size used in the correlation analyses.¹⁸ Although this rule is rendered obsolete by the use of multi-pass/multi-grid algorithms in the correlation analyses (except for the initial coarse grid), it provides a reasonable albeit rudimentary condition for the current processing scheme. As will be described below, the algorithm at present requires valid particle-image displacements to increase in a linear fashion over increasing temporal spacings. Modifications to the program in the near future will remove this assumption by inherently accounting for local acceleration effects. More on this topic is given in the concluding remarks section.

In addition to the particle displacement limit, a specified level of sensitivity is applied by the DEVOLS algorithm when considering the validity of vectors. This criterion is based on the notion that for negligible particle accelerations, all image pairs should in principle provide the same velocity measurement for a given spatial location. Because particle motions under a zero-acceleration condition remain constant with time, a linear trend is observed if their displacements are plotted over time. Considering only the measurements at a single spatial location satisfying the maximum displacement restriction, a linear trend should be observed if they are plotted against their corresponding interframe times. Therefore using ordinary least squares (OLS) statistics, a linear regression line can be fit to the data in which the slope is indicative of the local velocity. A measure of how well this regression line fits the displacement measurements is provided by the coefficient of determination, denoted R^2 . Depending on the user-specified sensitivity level, i.e., the minimum-allowable R^2 value, displacement measurements with the largest residuals are simply rejected until either the R^2 value exceeds the required tolerance or only a single, default measurement remains. The default measurement in the current algorithm corresponds to the particle displacement determined by the image pair spanning the shortest δt . Thus the default velocity measurement for each spatial location represents the conventional PIV measurement associated with the overall data acquisition rate. In the experiments of interest this interval is the 1 μs separation time between consecutive, subsequent frames. Only the default value is used at each location unless supplementary measurements provided by the additional image pairs are deemed valid by the user-specified, error-minimization criteria.

To better explain the DEVOLS processing scheme, consider the plot shown in figure 9. In this example all eight displacement measurements for a given spatial location are plotted against their corresponding

interframe times. Because 32×32 px² interrogation windows were specified during the correlation analyses, a maximum displacement limit was set at 12 pixels. This value is slightly larger than the one-quarter rule would suggest. Based on this restriction (depicted by the dashed red line in the plot), five of the eight measurements are immediately rejected. As mentioned, imposing a displacement restriction serves to minimize effects caused by particle accelerations. Such effects become increasingly pronounced over excessive particle displacements since the algorithm currently assumes only linear trends. Considering the remaining three measurements, a linear regression line is computed using OLS statistics with the added constraint that the line pass through the origin (since the limit of $\Delta x = 0$ as $\delta t \rightarrow 0$). Because the minimum R^2 value was specified to be 0.975, the measurement with the largest residual (labeled *Outlier* in the plot) is rejected. After computing a second OLS regression line, the new R^2 value is found to exceed the specified tolerance. Thus the slope of this final regression line represents the local velocity determined for this particular spatial location. The process is repeated for all spatial locations until a final velocity field is achieved.

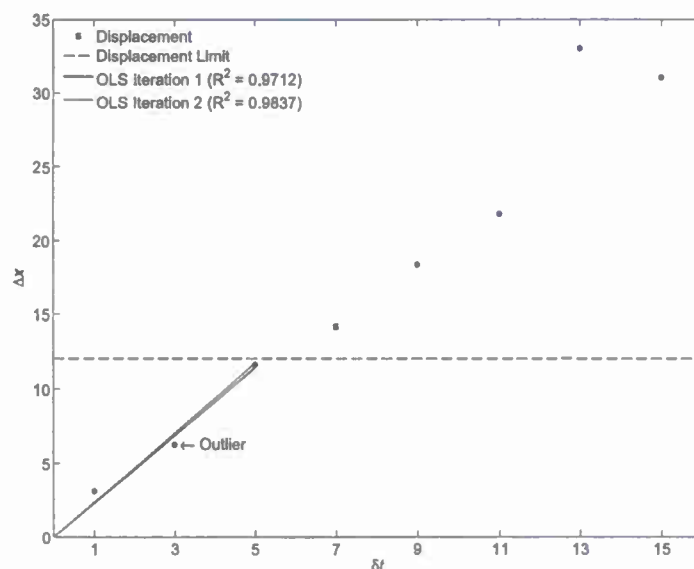


Figure 9. Graphical explanation of the DEVOLS processing scheme applied at a single spatial location. Measurements are deemed invalid based on a maximum displacement limit of 12 pixels and a minimum R^2 tolerance of 0.975 (both of these criteria are specified by the user). The slope of the final OLS regression line is indicative of the local velocity.

IV.B. DEVOLS validation

To validate the DEVOLS processing scheme described previously, a time-resolved sequence containing 16 synthetically generated particle images was considered. The particle density (ρ_{img}) in each image was chosen such that on average each interrogation window would contain 24 particles. The particle diameters were allowed to vary at most by 1 pixel from a nominally specified value of 5 pixels^c. In addition, the particles were allowed to exit the field of view based solely on their in-plane motions. The particles could also vary in depth within the light sheet (sheet thickness for the range [0 1] was set at 0.3), although such positions were fixed since no out-of-plane motion was permitted. For this initial case only zero-noise conditions were simulated. To maintain consistency with the Cordin CCD sensors, the image sizes were specified to be 2048×2048 px². It should be noted that the program used to generate this sequence was a modified version

^cLarge particle-image diameters were specified to better resemble the particles recorded in the experimental images. As mentioned, the resolution in these images is inherently reduced due to the intensification process associated with the camera. Consequently the minimum resolvable particle diameter associated with this camera is slightly larger than would be expected for a non-intensified CCD camera with a comparable sensor size.

of the synthetic particle-image generator in PIVlab, the time-resolved digital particle image velocimetry tool for MATLAB.¹⁹

The flow field simulated in the synthetic image sequence was a Hamel-Oseen vortex centered at the position (1024.5, 1024.5). The maximum circulation in terms of maximum particle displacement between consecutive, subsequent frames was limited to 8 pixels. This value was chosen such that the one-quarter rule would be satisfied for 32×32 px² interrogation windows over a single interframe time. A 50% overlap was specified for these windows during the correlation analyses. A vortex was chosen to validate the DEVOLS processing scheme because it provides a geometrically simple case of flow containing a wide velocity range. Depending on the interframe time, portions of the flow field are inherently under-sampled or drastically over-sampled when investigated by conventional PIV. This effect is evident in the individual correlation results presented in figure 10. A small δt provided by the central image pair can resolve the high-velocity regions

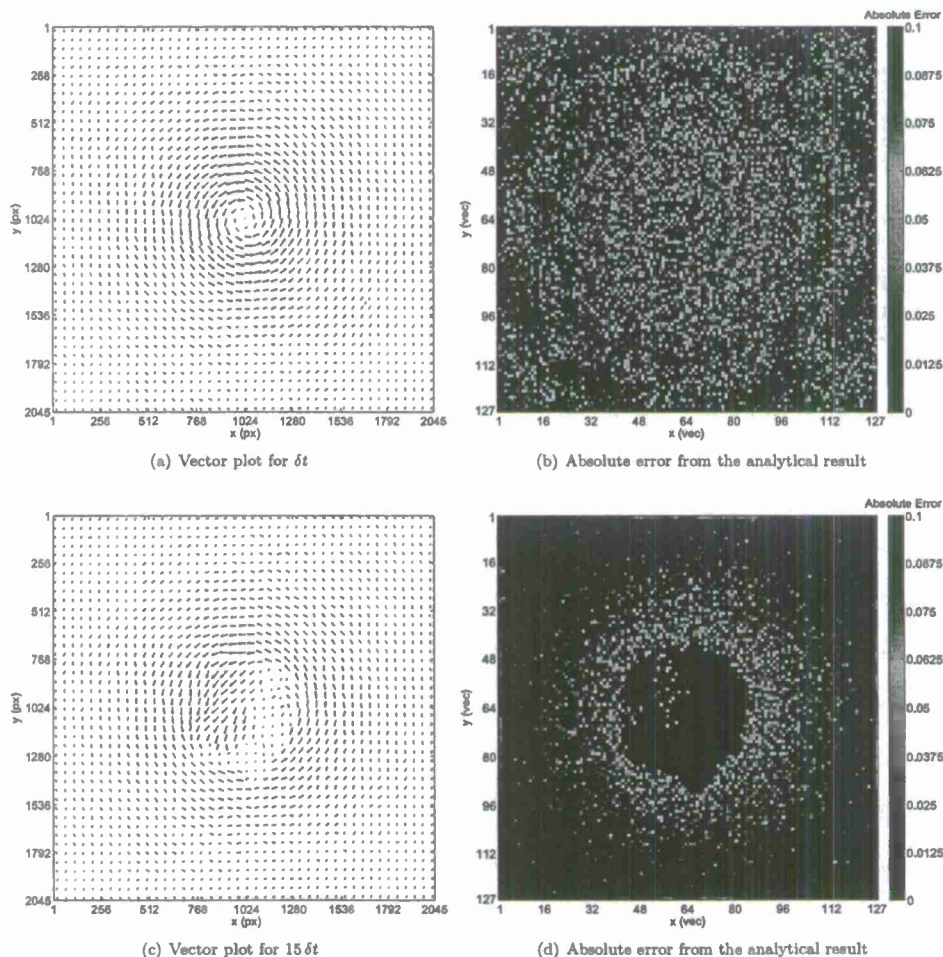


Figure 10. Velocity fields determined by the image pairs spanning δt and $15\delta t$, respectively. Every third vector is shown for clarity since each field contains over 16,000 vectors. As is evident by the corresponding absolute error plots, in both cases a single interframe time is insufficient to resolve the full DVR of the flow. The contour color is indicative of the total deviation in pixels from the analytical solution.

near the vortex core but in doing cannot adequately resolve the remaining low-velocity regions (figure 10(a)). As a result, particle motions in these regions approach the limit of minimum resolvable displacement and thus the measurement accuracy for individual vectors is of poor quality. Contrarily a large interframe time provided by the image pair spanning the entire temporal window of $15\delta t$ is unable to resolve the core (figure 10(c)). In this case, however, the low-velocity regions surrounding the core and nearing the image edges are highly resolved. The contour plot presented alongside each vector plot corresponds to the total deviation, or absolute error, in pixels that exists for that particular measurement (δt and $15\delta t$, respectively). The patterns visible in each plot illustrate the trends described previously. For both cases the low DVR in the measurements severely limits the viability of conventional PIV applications. It should be emphasized that because this investigation represents the ideal case of zero noise, the individual correlations perform very well. Still, the patterns visible in the absolute error plots clearly illustrate the effectiveness of the algorithm.

Using the DEVOLS method described previously, any number of displacement results from the eight correlation analyses can be considered at each spatial location to obtain a more accurate measurement of the velocity field. The fact that multiple interframe times are able to be used allows this measurement to characterize a much higher DVR of the flow than before. The plot shown in figure 11(a) contains the final HDR result. The error minimization criteria specified in the DEVOLS algorithm for this case were 12 pixels for the displacement limit and 0.975 for the R^2 tolerance. Unless specified, these values should be assumed for the HDR results contained in the remainder of this paper. As before, the total deviation in pixels from the analytical solution is shown in figure 11(b).

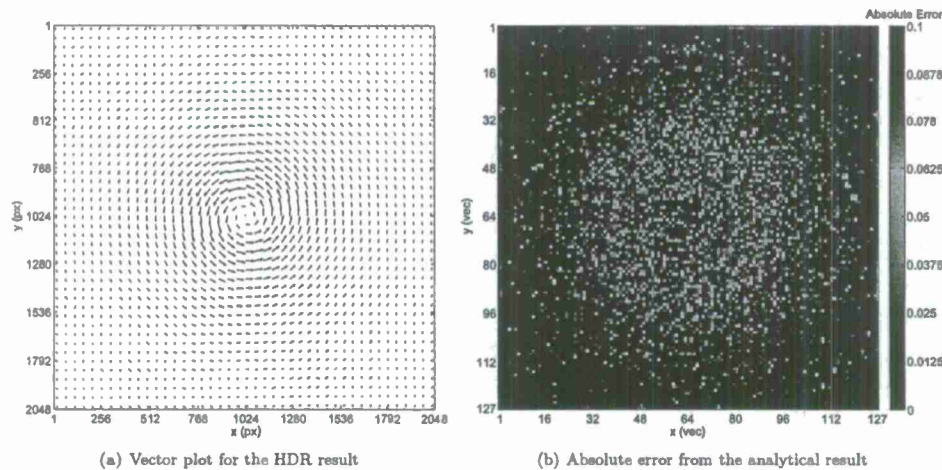


Figure 11. Velocity field and absolute error for the HDR result, respectively. The HDR result characterizes the DVR of the flow much better than the results shown in figures 10(a) and 10(c) since it is not restricted to a single interframe time. The pattern visible in the contour plot clearly illustrates this fact.

From the plots above, the measurement accuracy in the HDR result is much better than in the results shown previously for a single interframe time. The obvious reason is because the DEVOLS processing scheme can locally utilize the displacement results of multiple image pairs and thus multiple interframe times to more accurately sample the variety of flow regimes. For this flow field only the image pair spanning the shortest δt should ideally be used to sample the high-velocity regions near the vortex core. Contrarily multiple image pairs with successively increasing temporal separations should be used to sample flow regimes located at increasing spatial distances from the core. Considering the plot shown in figure 12(a), this exact trend is observed. The contour coloring scheme is indicative of the number of displacement measurements (N_{vec}) utilized by the DEVOLS algorithm to determine the final OLS regression line at each vector location. Because the minimum velocities in this flow field were still significantly higher than the minimum resolvable limit (assumed to be 0.1 pixels), only half of the image pairs were able to be used at any given location based on the specified settings (12 pixel displacement restriction and 0.975 R^2 tolerance). Figure 12(b) also illustrates this trend by plotting the velocity profile measured along the central, horizontal slice through

the vortex. As is evident, the HDR result shown in red almost exactly matches the analytical solution, whereas the individual correlation results show significant deviations. The results derived from the image pairs spanning the largest temporal distances are especially ineffective at resolving the high-velocity regions near the core.

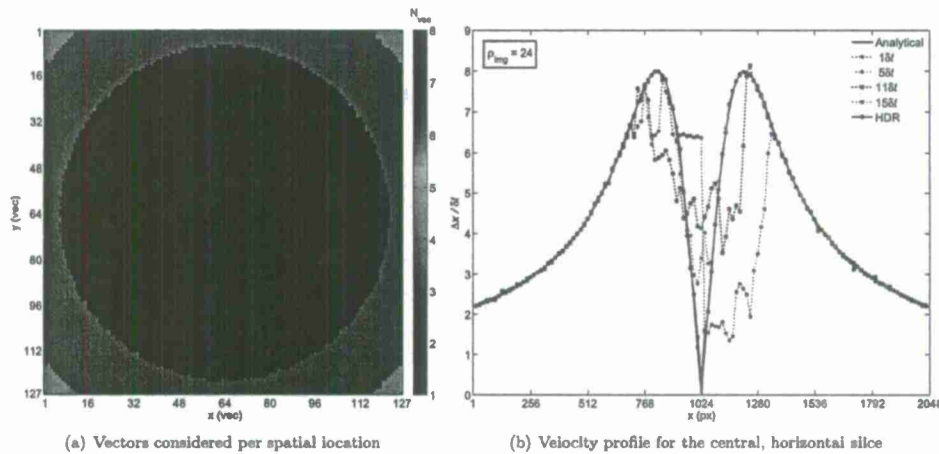


Figure 12. Results for the vector evaluation field as well as the central velocity profile, respectively. The trends observed in both cases indicate that only the image pair spanning the shortest temporal distance is capable of accurately resolving the high-velocity regions near the vortex core. Contrarily multiple image pairs spanning increasing temporal distances are able to resolve the low-velocity regions. Thus an increased number of displacement results can be utilized to determine the velocity vectors located at increasing spatial distances from the core.

IV.B.1. Varying particle density

To characterize the effect that different particle densities have on the DEVOLS algorithm, five temporally resolved image sequences were synthetically generated for the Hamel-Oseen vortex previously described. All parameters (particle diameter and variation, allowable depth within the light sheet, zero out-of-plane particle motion, maximum circulation or particle displacement between subsequent frames, and zero noise conditions) were held constant between the sequences except the total particle number. In each case this total particle number was chosen such that a desired, average number of particles would be found in the interrogation windows. Similarly as before, 32×32 px² windows were specified in the correlation analyses with a 50% overlap. The particle densities considered in this investigation and written in terms of particles per interrogation window are as follows: 3, 6, 12, 24, and 48. The HDR results shown previously for a particle density of 24 correspond to the same image sequence utilized in this investigation.

Considering the plot shown in figure 13, the particle densities chosen for this investigation did not appear to affect the DEVOLS algorithm in any appreciable way. A few blips are noticeable for $\rho_{img} = 3$, however the overall velocity profile still closely resembles the analytical result. One would expect the measurement error to increase for densities below 3 due to the lack of particles and consequent ambiguity in the correlation analyses. One would also expect the error to increase above 48 due to the increased overlapping of particle images in the recordings. Quantifying such levels where the DEVLOS processing scheme begins to experience significant errors relative to conventional PIV algorithms is certainly a topic warranting further investigation.

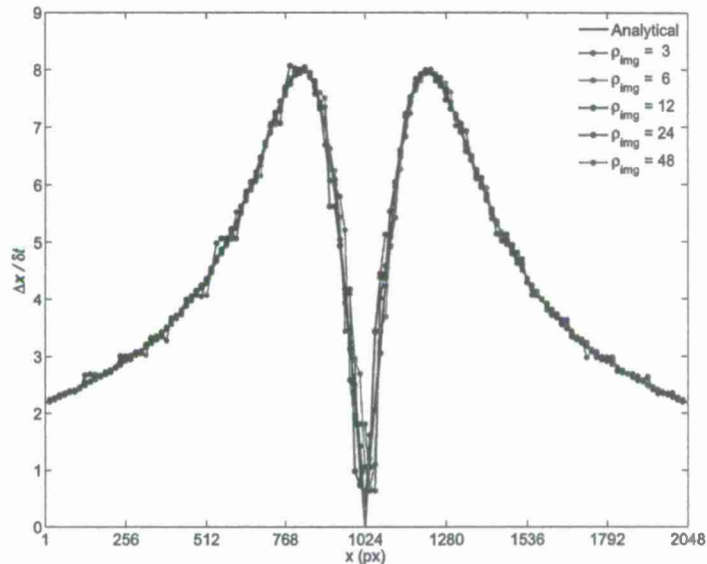


Figure 13. HDR results for the Hamel-Oseen vortex in which the particle density was varied. Five temporally resolved image sequences were synthetically generated to contain 3, 6, 12, 24, and 48 particles per interrogation window. The velocity profile shown corresponds to the central, horizontal slice through the vortex.

IV.B.2. Varying noise conditions

Two investigations were conducted to characterize the effects that different noise sources have on the DEVOLS algorithm. In both cases four image sequences of increasing noise levels were considered against a baseline sequence with zero noise. As before, a Hamel-Oseen vortex was simulated in the particle motions, and all parameters were held constant between sequences except for the variable in question. In both investigations the chosen particle density was 24 ($\rho_{img} = 24$), and care was taken to ensure that the initial positions of all particles remained the same. Thus all image sequences were identical in terms of particle density, particle distribution, and particle motion, however they differed in the prescribed level of noise.

Salt and pepper noise The first investigation was designed to simulate losses-of-pairs in the correlation analyses. This feat was accomplished by increasing the level of salt and pepper noise in the image sequences. Such noise affects the individual images within a sequence differently by randomly turning a number of pixels *on* to the maximum intensity value or *off* to the minimum intensity value. The number of pixels affected in each image is governed by a specified noise density (ρ_{noise}) applied to all of the images for a given sequence. Multiplying this value by the total number of pixels in each image provides the total number of pixels affected. Noise densities of 0, 0.025, 0.05, 0.075, and 0.1 were considered in this investigation. Sample particle images for $\rho_{noise} = 0$ (baseline) and $\rho_{noise} = 0.075$ are shown in figure 14, respectively.

The plot shown in figure 15 contains the HDR results of the five image sequences considered, namely the baseline case as well as the four cases of increasing noise. Similarly to before, this profile corresponds to the local velocity measurements along the central, horizontal slice through the vortex. As expected, the number of deviations from the analytical solution appears to increase with increasing noise density, although all results resemble the analytical solution rather closely. The fact that large deviations appear at different positions for different image sequences indicates that the salt and pepper noise applied to each sequence was sufficiently random. Thus the losses-of-pairs in the correlation analyses that resulted in the observed spikes were clearly due to the noise and not some artifact in the underlying particle-image distribution.

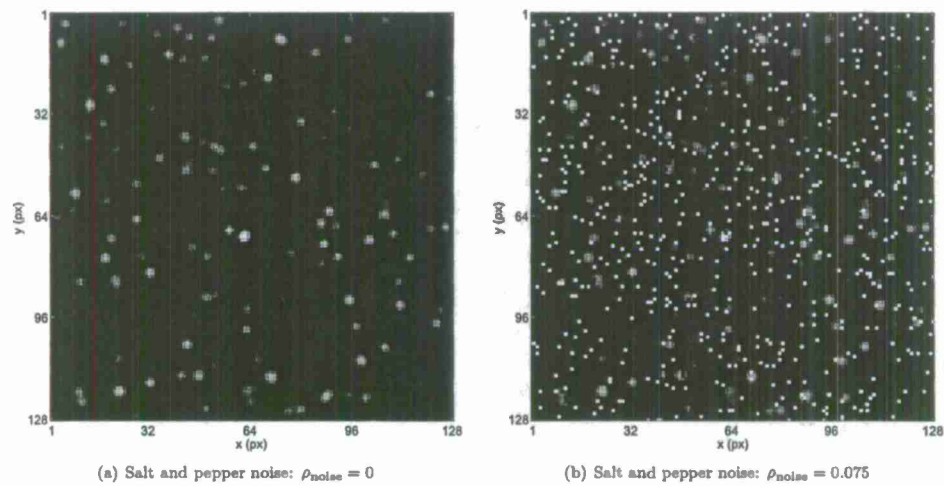


Figure 14. Image regions containing different levels of salt and pepper noise. Each region measures $128 \times 128 \text{ px}^2$ and contains an identical particle density and particle distribution.

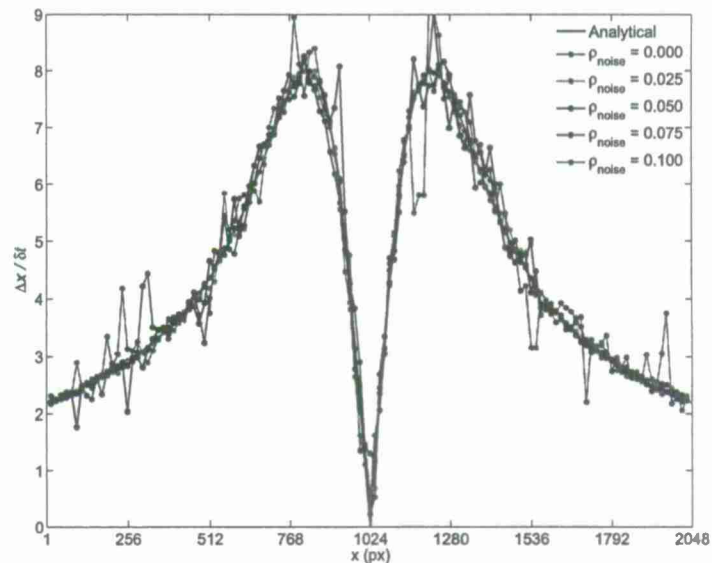


Figure 15. HDR results for the Hamel-Oseen vortex in which the level of salt and pepper noise was varied. Five temporally resolved image sequences were synthetically generated to contain noise densities of 0, 0.025, 0.05, 0.075, and 0.1 (where the density multiplied by the number of pixels per image yields the total number of pixels affected). The velocity profile shown corresponds to the central, horizontal slice through the vortex.

The plots shown in figure 16 correspond to the HDR result for $\rho_{\text{noise}} = 0.075$. Figure 16(a) shows the entire velocity profile, whereas figure 16(b) contains an enlarged view of the region indicated by the axes. Despite several wild deviations from the analytical solution by the individual correlation results, the HDR curve follows the analytical result rather closely. As expected, the correlations of image pairs with the largest temporal separations were mostly affected in the high-velocity regions. Thus large deviations are visible around the peaks just outside the central core. In contrast the image pair spanning a single δt was mostly affected in the low-velocity regions near the image edges. Although the observed deviations for this case are significantly less than those seen for the large interframe times, they are clearly visible in the zoomed view.

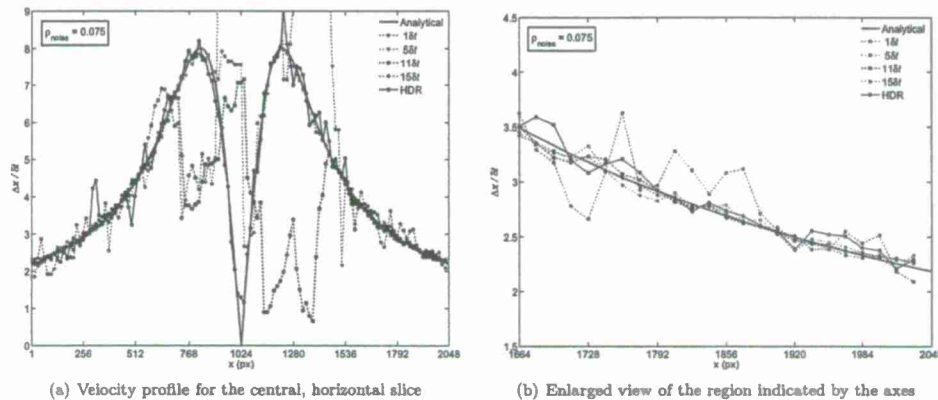


Figure 16. Results achieved for the central velocity profile by the image sequence with $\rho_{\text{noise}} = 0.075$. Plots are shown that contain the entire velocity profile (a) as well as an enlarged view of the region enclosed by the specified axes values (b). The HDR result performed better than the individual correlation results for almost all cases.

Gaussian white noise The second investigation was designed to simulate intensifier noise in the correlation analyses by increasing the level of Gaussian white noise in the image sequences. For clarity the term *Gaussian* refers to the distribution of noise values in each image (how frequently a particular value appears), and *white* describes the flat shape of the frequency spectrum. As such the noise applied to any two images (separated in time) for a given sequence is statistically independent or uncorrelated. Analogous to the noise density in the previous investigation, the mean (μ) and variance (σ^2) specified in the Gaussian distribution provided the means of controlling the noise level generated for each sequence. In all cases a zero-mean was specified, and variances of 0, 0.025, 0.05, 0.075, and 0.1 were considered. Sample particle images for $\sigma_{\mu=0}^2 = 0$ (baseline) and $\sigma_{\mu=0}^2 = 0.075$ are shown in figure 17, respectively.

Presenting all results in the same order as before, the plot shown in figure 18 contains the HDR results of the five image sequences considered, namely the baseline case as well as the four cases of increasing noise. Again this profile corresponds to the local velocity measurements achieved along the central, horizontal slice through the vortex. Analogous to the trend observed for increasing particle density, the number of deviations from the analytical solution appears to increase for increasing values of variance. Nevertheless all results resemble the analytical solution to some extent.

The plots shown in figure 19 correspond to the HDR result for $\sigma_{\mu=0}^2 = 0.075$. Figure 19(a) shows the entire velocity profile, whereas figure 19(b) contains an enlarged view of the region indicated by the axes. Although the HDR curve follows the general trend of the analytical solution rather closely, the deviations in this result are much more apparent than in the analogous HDR result shown for the previous investigation. In addition to the wild deviations experienced by the 15 δt and 11 δt correlation results near the core, small blips are evident in all of the individual results over much of the profile. Thus it appears that the Gaussian white noise, at least for the variances considered, had a much more profound effect on the individual correlation results and consequently the DEVOLS processing scheme. As is evident in the enlarged view, the HDR result for this case actually performed worse at several spatial locations compared to many of the individual correlations.

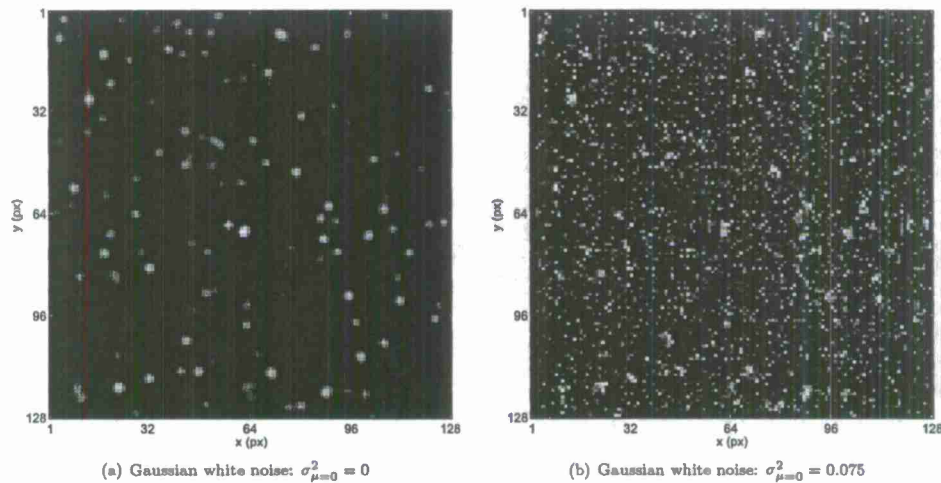


Figure 17. Image regions containing different levels of Gaussian white noise. Each region measures $128 \times 128 \text{ px}^2$ and contains an identical particle density and particle distribution.

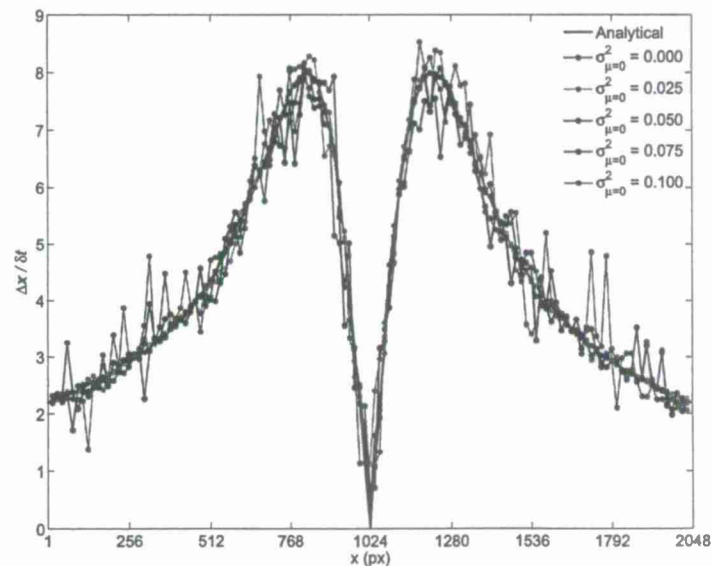


Figure 18. HDR results for the Hemel-Oseen vortex in which the level of Gaussian white noise was varied. Five temporally resolved image sequences were synthetically generated to contain zero-mean, Gaussian white noise with variances of 0, 0.025, 0.05, 0.075, and 0.1 (where the mean and variance were constant for all cases). The velocity profile shown corresponds to the central, horizontal slice through the vortex.

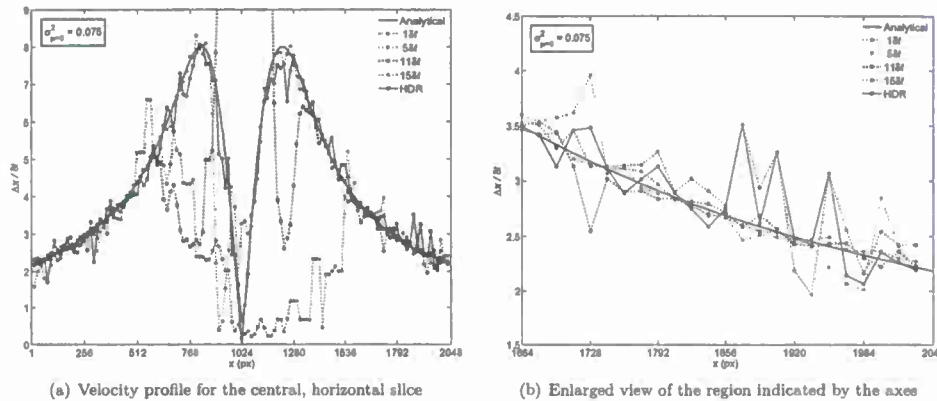


Figure 19. Results achieved for the central velocity profile by the image sequence with $\sigma^2_{\mu=0} = 0.075$. Plots are shown that contain the entire velocity profile (a) as well as an enlarged view of the region enclosed by the specified axes values (b). The HDR result performed worse at several spatial locations compared to the individual correlation results.

The reason the HDR result in certain situations does not converge on the analytical solution, particularly in the low-velocity regions, is because the default measurement is always considered (the measurement provided by the image pair spanning δt cannot be rejected in the current algorithm). This unfortunate scenario is the result of an inherent flaw that exists in the way the current processing scheme is designed. By not accounting for accelerations and thus assuming only linear displacements, it is possible in certain cases for the image pairs spanning the largest interframe times to provide a linear albeit incorrect slope for the particle-image displacement with time. Consequently if the OLS scheme is allowed to reject the default measurement in these cases, a regression line is fit to incorrect data. This situation is avoided in the majority of cases by forcing the algorithm to include the default measurement in all vector evaluations. Considering figure 19(b), however, this solution also results in the algorithm being significantly biased towards the default point. Work is currently being done to develop an additional criterion that will allow the default measurement to be rejected or ignored in the necessary cases. Two such methods are briefly discussed in the following concluding remarks.

V. Concluding remarks

The development and validation of a novel HDR processing scheme to supplement conventional PIV algorithms has been presented. As mentioned, this approach is currently being used to evaluate the TR PIV results from an experimental investigation regarding a high-temperature, shock-containing jet. The algorithm, termed dynamic evaluation via ordinary least squares (DEVOLS), offers substantial improvements over conventional PIV measurements for its ability to increase the dynamic velocity range. Unique to this approach is an iterative validation scheme that enables multiple displacement results to be utilized in the determination of an individual velocity vector. This feat is accomplished by fitting an ordinary least squares (OLS) regression line to those displacements satisfying a maximum displacement criterion at a given spatial location. The slope of this line is indicative of the local velocity. A user-specified tolerance, that is, a minimum allowable R^2 value, dictates how strictly this linear regression line must fit the data. To validate the DEVOLS algorithm, a temporally resolved sequence of synthetically generated particle images was considered in which the flow field surrounding a Hamel-Oseen vortex was simulated. Effects due to varying particle density as well as varying noise conditions in this flow environment were also characterized.

In addition to achieving results for the described experimental investigation, a couple of notable improvements to the DEVOLS algorithm are planned for the near future. The first involves transitioning the iterative validation scheme from an OLS regression model to a weighted least squares approach. This modification will allow increased emphasis to be placed on measurements corresponding to optimum particle displacements. Stated differently, instead of treating all valid displacement measurements equally, an additional criterion

will be used to determine the optimum temporal separation for a given spatial location. Increased weights will then be assigned to displacement measurements obtained by image pairs that span time intervals nearest this optimum value. In addition to this modification, the derivation of a least squares equation that accounts for acceleration is also in the works. This equation will enable regression lines to account for higher-order trends in the data and not be confined to linear fits. Such a scheme will also allow more data points to be considered at each location which will in turn improve the overall measurement accuracy.

References

- ¹Murray, N., Lyons, G., Tinney, C. E., Donald, B., Baars, W., Thurow, B., Haynes, H., and Panickar, P., "A laboratory framework for synchronous near/far-field acoustics and MHz PIV in high-temperature, shock-containing, jets," *Proceedings of the Internoise 2012/ASME NCAD meeting*, New York City, USA, August 19-22, 2012.
- ²Murray, N. E., Tinney, C. E., Thurow, B. S., and Sinha, N., "Toward active control of noise from hot supersonic jets," *Technical Proposal*, BAA 11-001 Special Notice 11-SN-0007.
- ³Ponton, M., Seiner, J., Ukelley, L., and Jansen, B., "A new anechoic chamber design for testing high-temperature jet flows," *AIAA Paper*, No. 2001-2190, 2001.
- ⁴Lempert, W. R., Wu, P., Zhang, B., Miles, R. B., Lowrance, J. L., Mastricola, V., and Kosonocky, W. F., "Pulseburst laser system for high speed flow diagnostics," *AIAA Paper*, No. 96-0179, 1996.
- ⁵Wernet, M. and Opalski, A., "Development and application of a MHz frame rate digital particle image velocimetry system," *AIAA Paper*, No. 2004-2184, 2004.
- ⁶Thurow, B., Satija, A., and Lynch, K., "Third-generation megahertz-rate pulse burst laser system," *Applied Optics*, Vol. 48, No. 11, 2009, pp. 2086-2093.
- ⁷Cavazzini, G. (editor), *The Particle Image Velocimetry - Characteristics, Limits and Possible Applications*, InTech, 2012.
- ⁸Liu, X. and Katz, J., "Instantaneous pressure and material derivative measurements using a four exposure PIV system," *Experiments in Fluids*, Vol. 41, No. 2, 2006, pp. 227-240.
- ⁹Violato, D., Moore, P., and Scarano, F., "Lagrangian and Eulerian pressure field evaluation of rod-airfoil flow from tomographic PIV," *Experiments in Fluids*, Vol. 50, No. 4, 2011, pp. 1057-1070.
- ¹⁰Adrian, R. J., "Dynamic ranges of velocity and spatial resolution of particle image velocimetry," *Measurement Science and Technology*, Vol. 8, No. 12, 1997, pp. 1393-1398.
- ¹¹Adrian, R. J., "Twenty years of particle image velocimetry," *Experiments in Fluids*, Vol. 39, No. 2, 2005, pp. 159-169.
- ¹²Fincham, A. and Delerce, G., "Advanced optimization of correlation imaging velocimetry algorithms," *Experiments in Fluids*, Vol. 29, No. Supplement 1, 2000, pp. S13-S22.
- ¹³Pereira, F., Ciarravano, A., Romano, G. P., and Felice, F. D., "Adaptive multi-frame PIV," *12th International Symposium on Applications of Laser Techniques to Fluid Mechanics*, Lisbon, Portugal, July 12-15, 2004.
- ¹⁴Hain, R. and Kähler, C. J., "Fundamentals of multiframe particle image velocimetry (PIV)," *Experiments in Fluids*, Vol. 42, No. 4, 2007, pp. 575-587.
- ¹⁵Persoons, T. and O'Donovan, T. S., "High dynamic velocity range particle image velocimetry using multiple pulse separation imaging," *Sensors*, Vol. 11, No. 1, 2011, pp. 1-18.
- ¹⁶Sciacchitano, A., Scarano, F., and Wieneke, B., "Adaptive multi-step ensemble correlation (AMEC) for time-resolved particle image velocimetry (TR-PIV)," *9th International Symposium on Particle Image Velocimetry*, Kobe, Japan, July 21-23, 2011.
- ¹⁷Meinhart, C. D., Wereley, S. T., and Santiago, J. G., "A PIV algorithm for estimating time-averaged velocity fields," *Journal of Fluids Engineering*, Vol. 122, No. 2, 2000, pp. 285-289.
- ¹⁸Keane, R. D. and Adrian, R. J., "Optimization of particle image velocimeters. Part I: Double pulsed systems," *Measurement Science and Technology*, Vol. 1, No. 11, 1990, pp. 1202-1215.
- ¹⁹Thielicke, W. and Stamhuis, E. J., "PIVlab - time-resolved digital particle image velocimetry tool for MATLAB," Published under the BSD license, programmed with MATLAB 7.1.0.246 (R14) Service Pack 3, MATLAB Central: *PIVlab.GUI.m*, 2005.

